Entangled states and coherent interaction in resonant media

Levon Chakhmakhchyan

To cite this version:

Levon Chakhmakhchyan. Entangled states and coherent interaction in resonant media. Physics [physics]. Université de Bourgogne, 2014. English. NNT : 2014DIJOS026 . tel-01128333

HAL Id: tel-01128333
https://theses.hal.science/tel-01128333

Submitted on 9 Mar 2015

UNIVERSITÉ DE BOURGOGNE
Laboratoire Interdisciplinaire Carnot de Bourgogne UMR CNRS 6303

NATIONAL ACADEMY OF SCIENCES OF ARMENIA
Institute for Physical Research

ENTANGLED STATES AND COHERENT INTERACTION IN RESONANT MEDIA

by

Levon CHAKHMAKHCHYAN

Thesis in Physics
Submitted for the Degree of Doctor of Philosophy

Date of defense July 21 2014

Jury

Gayane GRIGORYAN	Dr. of Physics Institute for Physical Research, Ashtarak	Co-Supervisor
Stéphane GUÉRIN	Professor ICB, Université de Bourgogne, Dijon	Co-Supervisor
Arthur ISHKHANYAN	Professor Institute for Physical Research, Ashtarak	Examiner
Claude LEROY	Professor ICB, Université de Bourgogne, Dijon	Co-Supervisor
Hrachya NERSISYAN	Professor Institute of Radiophysics and Electronics, Ashtarak	Examiner
Nicolas SANGOUARD	Professor GAP-Quantique, Université de Genève	Referee

Referees

Atom MURADYAN	Professor Yerevan State University, Armenia
Nicolas SANGOUARD	Professor GAP-Quantique, Université de Genève

LABORATOIRE INTERDISCIPLINAIRE CARNOT DE BOURGOGNE-UMR CNRS 6303
UNIVERSITE DE BOURGOGNE, 9 AVENUE A. SAVARY - 21078 DIJON - FRANCE

INSTITUTE FOR PHYSICAL RESEARCH, NATIONAL ACADEMY OF SCIENCES OF ARMENIA ASHTARAK-2, 0203 ARMENIA

UNIVERSITÉ DE BOURGOGNE
Laboratoire Interdisciplinaire Carnot de Bourgogne UMR CNRS 6303

NATIONAL ACADEMY OF SCIENCES OF ARMENIA
Institute for Physical Research

ENTANGLED STATES AND COHERENT INTERACTION IN RESONANT MEDIA

by

Levon CHAKHMAKHCHYAN

Thesis in Physics
Submitted for the Degree of Doctor of Philosophy

Date of defense July 21 2014

Jury

Gayane GRIGORYAN	Dr. of Physics Institute for Physical Research, Ashtarak	Co-Supervisor
Stéphane GUÉRIN	Professor ICB, Université de Bourgogne, Dijon	Co-Supervisor
Arthur ISHKHANYAN	Professor Institute for Physical Research, Ashtarak	Examiner
Claude LEROY	Professor ICB, Université de Bourgogne, Dijon	Co-Supervisor
Hrachya NERSISYAN	Professor Institute of Radiophysics and Electronics, Ashtarak	Examiner
Nicolas SANGOUARD	Professor GAP-Quantique, Université de Genève	Referee

Referees

Atom MURADYAN	Professor Yerevan State University, Armenia
Nicolas SANGOUARD	Professor GAP-Quantique, Université de Genève

LABORATOIRE INTERDISCIPLINAIRE CARNOT DE BOURGOGNE-UMR CNRS 6303
UNIVERSITE DE BOURGOGNE, 9 AVENUE A. SAVARY - 21078 DIJON - FRANCE

INSTITUTE FOR PHYSICAL RESEARCH, NATIONAL ACADEMY OF SCIENCES OF
ARMENIA ASHTARAK-2, 0203 ARMENIA

Remerciements

Je désire exprimer ma sincère considération à mes Directeurs de thèse, Dr. Gayane Grigoryan et Profs. Stéphane Guérin et Claude Leroy, pour leur soutien moral et scientifique et leur aide constante.

Je remercie le Conseil Régional de Bourgogne pour son aide financière. Ce financement m'a aussi permis de découvrir la culture française et de bénéficier de l'apport scientifique d'une collaboration réelle entre une équipe de recherche française et une équipe de recherche arménienne.

Je voudrais aussi remercier tous mes collègues et tout le personnel de l'Institute for Physical Research de l'Académie des sciences d'Arménie et du Laboratoire Interdisciplinaire Carnot de Bourgogne de l'université de Bourgogne pour leur aide et leur chaleureuse camaraderie.

Acknowledgments

I desire to express my sincere gratitude to my supervisors, Dr. Gayane Grigoryan and Profs. Stéphane Guérin and Claude Leroy, for their moral and scientific support and constant help.

I acknowledge the support of Conseil Régional de Bourgogne. This grant allowed me to discover the French culture and to benefit of both scientific contribution coming from a real collaboration between an Armenian research team and a French one.

I would also like to thank all the co-workers and staff of the Institute for Physical Research of National Academy of Sciences and Laboratoire Interdisciplinaire Carnot de Bourgogne of University of Bourgogne for the valuable assistance, kindly and warmhearted attitude.

Research conducted in the scope of the International Associated Laboratory IRMAS (CNRS-France & SCS-Armenia)
Part of the research leading to these results has received funding from the European Union FP7/2007-2013 under grant agreement n° 295025 - IPERA

Bourgogne Conseil régional

IPERA

IRMAS INTERNATIONAL ASSOCIATED LABORATORY

Etats intriqués et interaction cohérente dans les milieux résonants

L'intrication quantique, l'une des plus intrigantes caractéristiques de la théorie quantique, est devenue récemment un thème central de recherches en tant que ressource valorisable en communication quantique et traitement de l'information. Elle est au cœur des projets de téléportation quantique, de calculs quantiques et des protocoles de cryptographie quantique, et elle reconnu non pas comme un mais *le* trait caractéristique de la mécanique quantique.

Alors qu'on pensait que l'intrication ne pouvait pas se manifester au niveau macroscopique, il a été démontré que les états intriqués pouvait exister dans les solides à température donnée. Ce type d'intrication est appelée intrication thermique dans la littérature. A partir de mesures de susceptibilité magnétique, des preuves expérimentales ont été publiées pour des systèmes de spins de basse dimension, confirmant la présence d'intrication dans les matériaux à l'état solide. De plus, une observation expérimentale récente a montré la possibilité d'échantillons de diamants de taille millimétrique intriqués à température ambiante. D'autre part, des systèmes atomiques interagissant avec des champs quantifiés constituent des plates-formes alternatives pour le traitement de l'information quantique. En particulier, le transfert de population, total ou partiel, entre états de base est aussi au cœur de plusieurs processus quantiques allant de la chimie contrôlée par laser jusqu'à l'optique quantique moderne et l'information quantique, y compris la mise en œuvre de portes quantiques. Finalement, la condition clé dans quasiment toutes les applications pratiques de la science de l'information quantique est de protéger la cohérence des états quantiques contre les effets incohérents induits par l'influence incontrôlée de l'environnement. Une méthode puissante, qui permet de distribuer l'intrication entre des quantités distantes, implique la notion d'extraction d'un petit ensemble d'états plus fortement intriqués à partir d'un plus large ensemble d'états faiblement intriqués. Des schémas possibles de ce type peuvent être mis en œuvre, en particulier, dans les mémoires quantique, qui implique les principes d'interaction lumière-matière.

Dans le **chapitre 1**, nous considérons le modèle récemment proposé d'Ising-Heisenberg afin d'examiner les caractéristiques d'intrication de quelques composés particuliers, tel que le minerai naturel d'azurite ($Cu_3(CO_3)_2(OH)_2$) et une série de composés de coordination polymérique isostructurale de dimension deux $Cu_9X_2(cpa)_6 \cdot nH_2O$ (X=F, Cl, Br et cpa = carboxypentonic acid = acide carboxyle pentanoïque). Le réseau magnétique du premier matériau est représenté par une chaîne de diamants de spin 1/2, alors que le second matériau est décrit par un réseau triangulaire de Kagome. Bien qu'il soit une approximation du modèle d'Heisenberg d'interaction d'échange, le modèle d'Ising-Heisenberg fournit une explication satisfaisante des principales caractéristiques de ces matériaux. En raison du caractère séparable d'une interaction de type Ising, nous avons calculé l'intrication (quantifié par la concurrence) pour chacun des clusters quantiques des matériaux. Un traitement du type champ moyen basé sur l'inégalité de Gibbs-Bogoliubov, qui implicitement prend en compte l'interaction entre les clusters quantiques triangulaires, a été de plus appliqué au réseau triangulaire de Kagome. Nous montrons ici une forte relation entre la thermodynamique et les propriétés d'intrication du modèle. En particulier nous mettons en évidence que les pics de susceptibilité magnétique correspondent aux valeurs de paramètres pour lesquels l'intrication disparait. De plus la température critique d'intrication coïncide avec la transition de phase du second ordre du système. Nous avons étudié la structure des états fondamentaux de systèmes pour un large intervalle de forces d'interaction, révélant des régimes distincts avec des caractéristiques quantiques qualitativement différentes.

Dans le **chapitre 2**, nous considérons la limite classique de l'interaction de type Heisenberg qui se traduit par les modèles de spins classiques. La motivation principale pour étudier ces modèles est leur exacte résolution dans des cas particuliers. Ceci conduit à la possibilité de dériver des expressions analytiques pour des quantités thermodynamiques importantes. En particulier nous examinons la structure de phase du modèle Q-états de Potts et du modèle d'Ising d'interaction de trois sites sur des réseaux récursifs qui sont particulièrement performants dans l'analyse de nombreux systèmes magnétiques. On notera que l'approche de Bethe-Peierls, qui approxime des réseaux réels par des réseaux hiérarchiques (récursifs), est plus fiable dans certains cas que le traitement en champ moyen décrit ci-avant. Les modèles étudiés ont été exactement résolus par la technique de relation récursive, réduisant les propriétés thermodynamiques du modèle à des caractéristiques de morphismes rationnels. La structure de phase des ces modèles a été étudiée en détectant les points de bifurcation des morphismes correspondants. Une attention particulière a concerné l'apparition de fenêtres 3-périodiques dans la région chaotique des modèles de Potts et d'Ising (avec un couplage antiferromagnétique entre les nœuds de réseau). Nous avons mis en évidence quelques propriétés intrinsèques, telles que l'intermittence, apparaissant à chaque bord de la fenêtre et un nombre fini de cycles périodiques (modulés en phase) ainsi que le chaos confiné à l'intérieur de la fenêtre.

Nous abordons les systèmes de champs et d'atomes en interaction dans le **chapitre 3**, qui sont le cœur du problème du traitement de l'information quantique. En particulier nous considérons le modèle de Dicke pour modéliser l'interaction entre trois atomes piégés dans une cavité, interagissant via un couplage effectif, induit par le champ radiatif (limite dispersive). Nous avons mis en évidence la corrélation forte entre le modèle et les problèmes de frustration magnétique, et appliqué des outils similaires pour l'étude de l'intrication et les propriétés thermodynamiques du système. Néanmoins, une différence essentielle du système étudié est son accordabilité à la force de couplage, ce qui représente une difficulté supplémentaire dans le cas des solides. Une autre remarque importante concerne l'effet du vide induit par le décalage Stark, qui apparaît naturellement dans ce problème : il s'avère que ce terme change fondamentalement la représentation physique du problème.

Dans le **chapitre 4**, nous présentons une étude détaillée du processus de transfert de population via b-STIRAP dans un milieu atomique schématisé par un système Λ à 3 niveaux avec des forces d'oscillateurs différentes des transitions atomiques correspondantes. Nous avons déterminé les équations de propagation décrivant la dynamique du processus et des solutions analytiques approximatives ont été obtenues. Nous avons montré que l'efficacité de transfert de population est sensible au rapport des forces d'oscillateurs $q=q_p/q_s$, et peut être améliorée par un choix approprié de ce paramètre. En particulier, nous déterminons que l'efficacité de ce transfert est fortement affecté dans le cas $q > 1$ et décroit rapidement avec la distance de propagation, alors que les pulses se propageant conservent leur capacité à produire un transfert complet de population sur de grande distances de propagation quand $q \leq 1$. En outre nous montrons que le transfert peut s'opérer de façon superluminique. Les conditions restreignant la distance de propagation pour laquelle un transfert complet de population via b-STIRAP apparait dans un milieu ont été déterminées. De plus, nous avons abordé un autre problème, étroitement lié aux questions de traitement de l'information quantique et en communication : le problème de la distillation quantique dans les mémoires quantiques. Nous avons modélisé les phénomènes dissipatifs qu'un état compressé bimodal (intrication ressource initiale) subit quand il est stocké dans une mémoire, et nous avons démontré que les pertes affectent surtout le protocole original. En particulier, l'étape préparatoire en vue d'une "dé-gaussification" de l'état bimodal compressé initial, peut ne pas résulter en un accroissement de l'intrication, bien qu'étant une méthode bien connue d'accroissement local de l'intrication dans une mémoire parfaite. Nous avons donc analyser les contraintes sur les paramètres du protocole, au sein duquel on continue d'obtenir un gain d'intrication et nous avons montré que les restrictions supplémentaires permettent encore la réalisation expérimentale du schéma évoqué.

La thèse se termine par une **conclusion** qui met en évidence les principaux résultats de ce travail, et une liste de références récentes.

Contents

Introduction and motivation

Quantum entanglement, as one of the most intriguing features of quantum theory, has recently become a central area of research, since it is a valuable resource in quantum communication and information processing [1–5]. It is at the heart of quantum teleportation schemes [6–11], quantum computation [12–14] and quantum cryptography protocols [15–17], and is recognized as not one but rather *the* characteristic trait of quantum mechanics [18]. On the other hand, entanglement provides a new perspective for understanding quantum phase transitions (QPT's) and collective phenomena in many-body and condensed matter physics, where the Heisenberg model can be used as an appropriate tool for a detailed theoretical analysis [19–23]. Additionally, a recent research points to a connection between the entanglement of a many-particle system and the existence of QPT's and scaling [24, 25].

Although it was believed that entanglement should not manifest itself in macroscopic objects, it was theoretically demonstrated that entangled states can exist in solids at finite temperatures. Such entanglement is referred in literature to as *thermal entanglement* [19]. Its existence led to an intense search of a relation between entanglement thermal and thermodynamic (e.g. magnetic) properties of a system [26–29]. Based on magnetic susceptibility measurements [29] a few experimental evidences have been reported for low-dimensional spin systems, confirming the presence of entanglement in solid state materials. Particularly, thermal entanglement was detected experimentally in a number of compounds, as $Na_2Cu_5Si_4O_{14}$ [30], $CaMn_2Sb_2$ [31], pyroborate $MgMnB_2O_5$ the warwickite $MgTiOBO_3$ [32], $KNaMSi_4O_{10}$ (M=Mn, Fe or Cu) [33] and metal carboxylates [34]. Moreover a recent experimental observation showed a possibility of entangling macroscopic millimeter-sized diamond samples at room temperature [35].

Meanwhile, another issue of quantum information processing is the problem of quantifying entanglement, which plays a key role in estimating the fidelity of a quantum state teleportation [36], or in defining the amount of noise in a dense coding protocol [37]. Additionally, the study of entanglement in solid state physics is also of a great interest, since many proposals of quantum chips are solid state-based. A number of entanglement measures has been proposed recently. As shown in Ref. [38], it is reasonable to define the entanglement of a pure state of any bipartite system as the von Neumann entropy of either of its two parts. An explicit way of computing entanglement of formation of a mixed state, by means of a quantity called *concurrence*, was proposed in Refs. [39, 40]. But, the formula provided there, is applicable for a mixed state of two qubits only. Another computable measure of entanglement, the *negativity* [41, 42], which is based on Peres' separability criterion [43], can be used for an arbitrary bipartite state. We emphasize again the obvious fact, that the amount of entanglement cannot be measured directly in experiment. Thus one needs a way of tracking its behavior within an experiment.

One of the goals of the present thesis is to analyze the entanglement features of low-dimensional frustrated spin systems. Note that during the last two decades low-dimensional magnetic materials with competing interactions or geometrical frustration have become an intriguing research object. Particularly, these materials exhibit a rich variety of unusual ground states and thermal properties, as a result of zero and finite temperature phase transitions [44–57]. Unfortunately, the rigorous theoretical treatment of geometrically frustrated quantum Heisenberg models is a complicated procedure. There are very few exact results for antiferromagnetic spin chains, provided, in particular, through a powerful technique, known as the Bethe ansatz [58–60]. However, in a general case the problem that arises due to a non-commutability of spin operators involved in the Heisenberg Hamiltonian, is difficult to overcome. Therefore, one adopts a number of approximations, which resolve the mathematical difficulties, still providing satisfactory qualitative and quantitative results. One approach is based on introduction of Ising spins at some nodal sites of a lattice, which results in an alternating sequence of Ising and Heisenberg variables [61–68]. Another method for a study of a system in the thermodynamic limit is the mean field approach. An efficient mean-field-like treatment is based on the Gibbs-Bogoliubov inequality, which transforms a system into a collection of clusters in an effective magnetic field [69, 70]. Even though within this approximation the clusters are considered as being non-interacting, the self-consistency of effective magnetic fields implicitly involves their mutual coupling.

In what follows we use both of the above approximations for investigation of entanglement properties of two types of compounds, namely the natural mineral azurite ($Cu_3(CO_3)_2(OH)_2$) [71] and a series of two-dimensional isostructural polymeric coordination compounds Cu_9X_2 $(cpa)_6 \cdot$ nH_2O ($X = F$, Cl, Br and cpa=carboxypentonic acid) [72–76]. The first one is represented by a diamond chain structure, while the second one is formed by a triangulated Kagomé lattice. Note that these materials fall into a class of geometrically frustrated systems and exhibit a rich ground state structure with peculiar quantum behavior. Here we make an additional remark: within the adopted Ising-Heisenberg model, neighboring Heisenberg clusters (a dimer in the case of the diamond chain, and a trimer in the case of the triangulated Kagomé lattice) are separable from each other due to the classical (diagonal) nature of Ising-type exchange interactions. Thus, we can calculate entanglement (quantified by concurrence) for each of these quantum subdivisions separately.

Another approach of dealing with spin lattice models is to work in the limit of classical exchange interactions, i.e., to substitute the Heisenberg exchange interaction by an Ising one. Note that this approximation works satisfactory good in a strong magnetic field: when the latter is directed along the z-axis, a reduction of transverse fluctuations is expected to occur. In other words, in this case the S^x and S^y-spin components become infinitely small and thus can be neglected [77, 78]. As a result, one can solve exactly the models in some particular cases, which leads to analytic expressions for thermodynamic quantities of interest. Particularly, classical spin models are solved exactly on recursive (hierarchical) lattices, which are good approximations for real existing ones (the so-called Bethe-Peierls approximation) [79–82]. An important remark here is that the Bethe-Peierls approximation is more reliable than the above discussed mean-field approach [83, 84].

Distinguishable systems among classical spin models are the Ising and the Potts models. Particularly, the multisite interaction Ising model is efficient in description of properties of solid ^{3}He [78, 85] and RNA-like molecules [86–88]. Meanwhile, the Potts model, apart of being strongly related to problems of magnetism [89–91], falls in the same universality class as the gelation processes in branched polymers [92, 93]. Note that the model is well-defined for non-integer values of Q (as pointed out in Ref. [94]). Besides, many physical phenomena like the resistor network, dilute spin glass, self organizing critical systems can be formulated in terms of the Potts model, when $Q < 2$ [95–97].

In the present thesis we are interested in two particular examples of classical spin models, namely, the three-site interaction antiferromagnetic Ising (TSAI) model on a Husimi lattice and the Q-state Potts model on a Bethe lattice. The exact solution of these models is given through the recurrence relation technique. Within this method statistical properties of a system are defined by one- or multidimensional rational mappings [78–80,83–87]. When the lattice nodes are coupled through an antiferromagnetic interaction, both models exhibit a rather complex behavior, featuring doubling bifurcations, intermittency and chaos. The phase structure of these systems can be studied by detecting their bifurcation points, which are equivalent to phase transition points between modulated phases of different periods or between chaotic and periodic regimes. Although the above models are purely classical, they can be a good testing ground of applied methods and in some cases can also provide satisfactory quantitative picture [98–101]. We emphasize here a strong relation between quantum phase transitions, chaos and entanglement: as pointed out in Refs. [102–105], the quantum features of a system can differ, depending on the initial state, namely if it is chaotic or not.

Quantum information processing can be also implemented in alternative platforms to solids, such as an atomic system interacting with quantized fields. Many effective models of such interactions, proposed within the scope of cavity quantum electrodynamics, were investigated both from theoretical and experimental points of view [106–114]. The Dicke model (DM), describing the interaction of a single-mode bosonic field with a collection of two-level atoms [115,116] is of particular interest. It has been predicted to exhibit both equilibrium and non-equilibrium intriguing quantum phase transitions. The equilibrium superradiant QPT, followed by a spontaneous symmetry breaking, has been recently implemented experimentally in a realization of the DM with a Bose-Einstein condensate in an optical cavity [117,118]. On the other hand, existence of a set of non-equilibrium QPT's was demonstrated in Ref. [119].

The DM is usually considered in the rotating-wave approximation, which simplifies the analysis of some important phenomena such as super-radiance, collapses, and revivals of Rabi oscillations, squeezing, and phase transition [120,121]. Another important special case of the

DM, corresponds to the so-called dispersive limit [122–124]. The latter regime is widely used for quantum information processing [125–128]. In this case the radiation field mediates an effective coupling between the atoms in a cavity, which has a nature of a dipole-dipole interaction, preserving the number of field photons and of excited atoms. We remark here, that an experimental realization of entangled states of two and four trapped ions within this regime has been reported in Ref. [129]. Thus, one could also address to the question of quantifying entanglement between the trapped atoms (ions), described by the Dicke model in the dispersive regime. Note that the interaction term of the effective DM in the dispersive limit can be also regarded as a Heisenberg-type exchange interaction. Hence we find a strong relation between this model, the above described frustrated magnetism and systems of interacting magnetic spins.

On the other hand, complete or partial population transfer between ground states is also at the heart of many quantum processes [130], ranging from laser-controlled chemistry [131] to modern quantum optics and quantum information, including quantum gate implementation [132]. Adiabatic passage, which allows the dynamics to follow a single eigenstate of the system, is often used to implement such transfers due to its robustness with respect to field fluctuations and to the imperfect knowledge of the studied system. In particular, the stimulated Raman adiabatic passage (STIRAP) [133, 134], and its various extensions [135–137], which induce a complete population transfer in a Λ-system, have become much popular recently. The main advantage relies on its dark-state dynamics which does not involve the upper state in the adiabatic limit, and makes this process in principle immune to decoherence. An efficient population transfer has been recently reported in crystals doped with rare-earth elements Pr^{3+}:$\mathrm{Y_2SiO_5}$ [138, 139]. However this process requires in practice a large pulse area to satisfy the adiabaticity and prevents in most cases its use for pulses shorter than nanoseconds.

An alternative efficient method is provided through the b-STIRAP technique, featuring an intuitive sequence of pulses with a large one-photon detuning. Unlike the STIRAP, for which the dynamics adiabatically projects along a dark state, the intuitive process follows a bright state [140, 141]. The technique is referred to in literature as bright- or b-STIRAP. The possibility of such a transfer for one atom was predicted and analyzed in Ref. [142].

Additionally, the effect of spontaneous decay from the intermediate state inside the system for b-STIRAP was studied in Refs. [143–145]. Note that due to the process of b-STIRAP, Λ-system is fully reversible in interactions with short laser pulses of durations much shorter than the relaxation times of the system and may hence serve for implementation of all-optical reversible processor [146]. Recently, the combination of STIRAP and b-STIRAP has been also used for the experimental implementation of optical logical gates in a solid memory [147].

Meanwhile, the propagation effects can modify the results of above processes drastically. A number of works were devoted to the investigation of the population transfer within a counterintuitive sequences of pulses via STIRAP method [148–152]. Particularly, it was pointed out that during pulse propagation in the STIRAP regime, the interaction adiabaticity, as well as the spatial evolution of propagating pulses, are strongly affected by the relationship between the oscillator strengths of the corresponding atomic transitions. Additionally, in a recent work [153] a detailed theoretical analysis of the b-STIRAP process in a media with equal oscillator strengths was performed. However, the physical effects occurring during population transfer through the b-STIRAP mechanism in a media with unequal oscillator strengths have not been reported yet. Thus, anticipating a sensibility of the efficiency of the population transfer to the medium properties (such as the relation between oscillator strengths), a detailed analysis of b-STIRAP propagation effects becomes motivated.

Finally, the key requirement in essentially all practical applications of quantum information science is to protect the coherence of quantum states against decoherence, induced by the uncontrolled influences of an environment. One of the possible strategies to protect entanglement from decoherence effects is based on reducing the interaction with the environment, which however, is not sufficient in a number of cases. A more powerful method, which allows one to distribute entanglement between distant parties, involves the notion of extracting a small ensemble of more strongly entangled states from a larger ensemble of weakly entangled states. The strategy achieving this is referred to as *entanglement distillation* [3, 38]. Challenging experimental realizations of these distillation protocols in qubit systems and other finite-dimensional settings [154, 155] have been performed.

An important step in the theory of entanglement distillation was the invention of continuous-variable entanglement distillation protocols [156, 157], which turn out to be easier to implement in experiment. A continuous-variable entanglement distillation protocol using quantum memories was recently proposed in Ref. [158]. The authors considered the case of perfect quantum memories. However, once locally prepared and stored in a memory, two-mode squeezed states (the initial entanglement resources of the protocol) or any quantum states are subject to decoherence and deteriorate, with a consequent loss of entanglement. Therefore, the dissipation can modify strongly the properties of the scheme and thus the question of how a realistic quantum memory affects the performance of the original compact continuous-variable entanglement distillation protocol is of particular interest. In what follows we will study these effects in detail and conclude that the compact distillation protocol with the practical constraints coming from realistic quantum memories allows a feasible experimental realization within existing technologies.

Objectives of the thesis:

1. The investigation of entanglement properties of quantum dimeric and trimeric units in low dimensional spin models, describing real existing materials. Studies of the effects of the temperature and the external magnetic field and comparison of thermodynamic and entanglement features.
2. The analysis of exactly solvable classical spin models on hierarchical lattices, which are considered as approximations for quantum models on real lattices. The investigation of the phase structure of the systems within the dynamical system approach.
3. The study of quantum information issues in systems of interacting atoms and fields: quantifying entanglement between effectively coupled atoms in a cavity and the detailed analysis of population transfer in media of unequal oscillator strengths.
4. The investigation of compact continuous-variable entanglement distillation protocol in realistic quantum memories in presence of dissipation effects.

Scientific novelty and the practical value of the work:

1. For the first time the entanglement features of low dimensional spin models, describing the natural mineral azurite ($Cu_3(CO_3)_2(OH)_2$) and copper based coordination compounds [Cu_9X_2 $(cpa)_6\cdot$ nH_2O ($X = F, Cl, Br$)] were investigated. Our studies confirm

that solid state materials can be considered as a natural entanglement resource. Additionally, the detailed analysis of the rich phase structure of the present materials reveals regimes with the most robust entanglement behavior. On the other hand, the strong relation between thermodynamic and entanglement features, shown in the thesis, allows one to track the behavior of quantum entanglement through an experiment.

2. Using the dynamical system approach, the phase structure of some classical models on hierarchical (recursive) lattices has been studied. The distinguishable feature of the approach is the possibility of obtaining analytic formulas for the thermodynamic quantities of interest, which allows a comprehensive analysis of the phase structure. For the first time the transition between chaotic and periodic regimes by means of tangent bifurcation detection of rational mappings, describing the above models has been analyzed.

3. A detailed description of entanglement features of three atoms trapped in a cavity within the dispersive regime is presented. We showed a relatively simple tunability of the interaction strength of the above system and its close relation to the problems of frustrated magnetism and interacting magnetic spins.

4. A detailed investigation of propagation of two intense laser pulses in a medium of Λ-type atoms with unequal oscillator strengths is performed. Obtained results are crucial in some problems of quantum information theory, as, e.g., in the analysis of population transfer mechanism in media possessing the above properties.

5. The dissipation effects in a recently proposed compact continuous-variable entanglement distillation protocol have been analyzed. We showed that the losses, present in any realistic quantum memory, modify strongly the properties of the original protocol, putting additional constraints on the parameters of the experiment. Nevertheless, our analysis confirms that entanglement distillation in quantum memories is still possible within the emerging technologies, which allows its further practical implementation.

The statements of the thesis:

1. The spin-1/2 Ising-Heisenberg models, describing the natural mineral azurite ($Cu_3(CO_3)_2(OH)_2$) and copper based coordination compounds [Cu_9X_2 $(cpa)_6\cdot$ nH_2O (X = F, Cl, Br)] possess a rich phase and ground state structures with qualitatively different thermodynamic and entanglement features. Entanglement and magnetic properties of the above models share strong common behavior.

2. The three-site interaction Ising and the Q-state Potts models on the Bethe and Husimi (recursive) lattices exhibit chaos, which is confined inside a three-periodic window. Phase transition points of the models coincide with bifurcation points of corresponding one-dimensional rational mappings.

3. The entanglement properties of three atoms trapped in a cavity and effectively coupled by means of a radiation mode are highly pronounced in a specific range of the temperature, atomic transition eigenfrequency and the effective coupling strength.

4. The efficiency of a superluminal population transfer in a medium of Λ-type atoms can be increased by an appropriate choice of the oscillator strengths of adjacent transitions.

5. The experimental realization of an effective compact continuous-variable entanglement distillation protocol is possible within existing technologies, notwithstanding the inevitable dissipation effects, present in a realistic quantum memory.

Our results on entanglement properties of spin lattice models are published in Refs. [159–162]. As for the studies of classical spin models, they are presented in Refs. [163–166]. The quantum information problems in systems of interacting atoms and fields are addressed to in Refs. [167–169]. Finally, the dissipation effects of compact continuous-variable entanglement distillation protocol in realistic quantum memories are studied in Ref. [170].

In the rest, the thesis is organized as follows. In Chapter 1 we consider the entanglement properties of the spin-1/2 Ising-Heisenberg model on a diamond chain and on a triangulated Kagomé lattice. We also perform some comparative analysis of their thermodynamic and entanglement features, pointing out certain similarities between them.

In Chapter 2 we address to thermodynamic properties of the Q-state Potts and the three-site interaction Ising models on recursive lattices. Additionally, we study here the phase structure of these models by detecting bifurcation points of corresponding rational mappings obtained through the recursion relation technique.

In Chapter 3 we turn to the discussion of systems of interacting atoms and fields. Particularly, we investigate the entanglement and thermodynamics properties of effectively coupled three atoms in a cavity, within the dispersive limit. Furthermore, we present a detailed analysis of the b-STIRAP process in a medium of unequal oscillator strengths.

Finally, Chapter 4 is devoted to the studies of dissipation effects in a compact continuous-variable entanglement distillation protocol. We consider the efficiency of the realistic scheme and discuss its possible practical implementation.

Chapter 1

ENTANGLEMENT PROPERTIES OF SPIN LATTICE MODELS [1]

1.1 Introduction

The study of geometrically frustrated magnetic systems is deeply associated with a number of aspects of modern physics, including quantum information theory, material science, high temperature superconductivity and others. As attractive models among these systems one should mention those having a diamond-chain structure. The latter consists of diamond-shaped topological units along the chain (Fig. 1.1). It has been observed that the compounds $A_3Cu_3(PO_4)_4$ with A=Ca, Sr [171, 172], $Bi_4Cu_3V_2O_{14}$ [173] and $Cu_3(TeO_3)_2Br_2$ [174] can be nicely modeled by the Heisenberg diamond chain. Addiotionally, recent experimental results on the natural mineral azurite ($Cu_3(CO_3)_2(OH)_2$) [71] showed that Cu^{2+} ions of this material form a spin-1/2 diamond chain. Furthermore, the discovery of a plateau at 1/3 of the saturation value in the low-temperature magnetization curve [71, 175] has triggered an intensive interest in the magnetic properties of azurite [176–179]. However, the question of the strength and the type of exchange interactions for this natural mineral, despite the long-standing interest, is still open. The first diamond spin chain was explored under a symmetrical condition $J_1 = J_3$ [180] that predicted magnetization plateaus both at 1/3 and 1/6 of saturation [181, 182]. Next, the properties of frustrated diamond chain with

---

[1] The results considered in this chapter are published in Refs. [159–162].

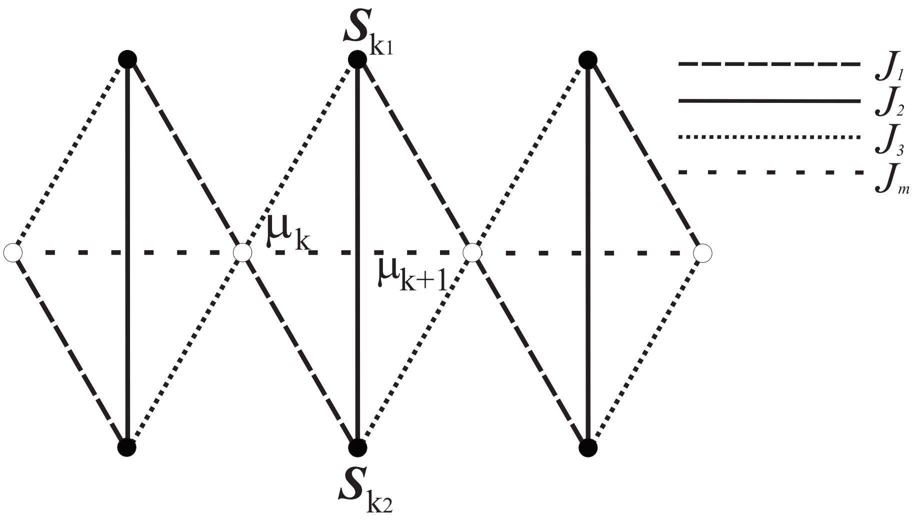

Figure 1.1: A cross-section of a generalized symmetrical diamond chain (k labels the number of the cluster). The empty (monomeric units) and full circles (dimeric units) denote lattice positions of the Heisenberg and Ising spins (within the proposed Ising-Heisenberg model), respectively. Solid lines schematically reproduce the Heisenberg J_2 interactions between dimeric units, while the broken ones label the Ising-type (nearest-neighbor J_1, J_3 and next-nearest neighbor J_m) interactions.

ferromagnetic interactions $J_1, J_3 < 0$ and antiferromagnetic interaction $J_2 > 0$ was studied theoretically in Ref. [183]. Other exchange interactions, like an additional cyclic four-spin [184] and J_m interaction between monomeric units (the so-called generalized diamond chain) [185] were also taken into account. Additionally, the importance of an anisotropic exchange and Dzyaloshinskii-Moriya interaction or interchain coupling was discussed in Refs. [186,187]. Summing up, the theory predictions for certain values of exchange coupling constants within a relatively broad range can fit the experimental results. The controversy on these values seems to be cleared up only recently (the latest comparison of experimental and theoretical results can be found in Ref. [188]).

Motivated by the controversies discussed above and the fact that different compounds can be described by means of a diamond chain, we shall explore systematically the generalized symmetrical spin-1/2 diamond chain with various competing interactions in a magnetic field. Owing to the fact, that it is difficult to fulfil fully quantum geometrically frustrated models, we use the recently proposed geometrically frustrated Ising-Heisenberg diamond chain model [61–67]. The latter suggests to overcome the mathematical difficulties by introducing Ising spins at the nodal sites and Heisenberg dimers on the interstitial decorating sites of the diamond chain (Fig. 1.1). Additionally, for understanding of the properties of underlying purely quantum models an analytic expression for all thermodynamic functions of the model is required. Note that some exactly solvable models with Ising and Heisenberg bonds can also provide satisfactory quantitative picture [189].

Another interesting system among geometrically frustrated topologies are the magnetic materials in form of two-dimensional isostructural polymeric coordination compounds Cu_9X_2 $(cpa)_6\cdot$ nH_2O (X = F, Cl, Br and cpa=carboxypentonic acid) [72–76]. The magnetic lattice of these series of compounds consists of copper ions placed at two non-equivalent positions, which are shown schematically as open and full circles in Fig. 1.2. Cu^{2+} ions with a square pyramidal coordination (a-sites) form equilateral triangles (trimers) which are connected one to another by Cu^{2+} ions (monomers) with an elongated octahedron environment (b-sites) forming the sites of Kagomé lattice. This magnetic architecture, which can be regarded as triangulated (triangles in triangles) Kagomé lattice, is currently under active theoretical investigation [68, 190].

The spin-1/2 Ising model on the triangulated Kagomé lattice has been exactly solved in Ref. [191]. However, in its initial form theory fails to describe the properties of the aforementioned compound series, since it entirely neglects quantum fluctuations firmly associated with a quantum nature of the paramagnetic Cu^{2+} ions having the lowest possible quantum spin number 1/2. Further extension to the Ising-Heisenberg model by accounting for quantum interactions between Cu^{2+} ions in a-sites (with quantum spin number 1/2) in the limit when monomeric b-spins have an exchange of Ising character, provides much more richer physics and displays essential features of the copper based coordination compounds [192, 193]. The strong antiferromagnetic coupling has been assumed for J_{aa} between trimeric a-sites, with a weaker ferromagnetic exchange J_{ab} between the trimer a- and monomer b-sites at the ratio $|J_{ab}/J_{aa}| \approx 0,025$ [194].

In what follows we shall mainly deal with the quantum entanglement properties of the spin-1/2 Ising-Heisenberg model on a generalized symmetrical diamond chain and on a triangulated Kagomé lattice.

Additionally, taking into account that each Heisenberg dimer of the diamond chain interacts with its neighboring dimer through the Ising-type, i.e. classical exchange interaction, we find that the states of two adjacent dimers become separable (disentangled) [1–3]. Thus, we can calculate the concurrence (a measure of pairwise entanglement [39,40]), which characterizes quantum features of the system, for each dimer separately. One of the main objectives of the next section is to reveal different regimes of the symmetrical diamond chain and to analyze new quantum effects (such as a double peak behavior in the concurrence versus temperature curves and existence of magnetic entanglement [19] of two different values). Note that one finds a similar situation with the triangulated Kagomé lattice: each a-type trimer interacts with its neighboring trimer through the Ising exchange interaction, therefore the states of two neighboring a-sublattices are separable.

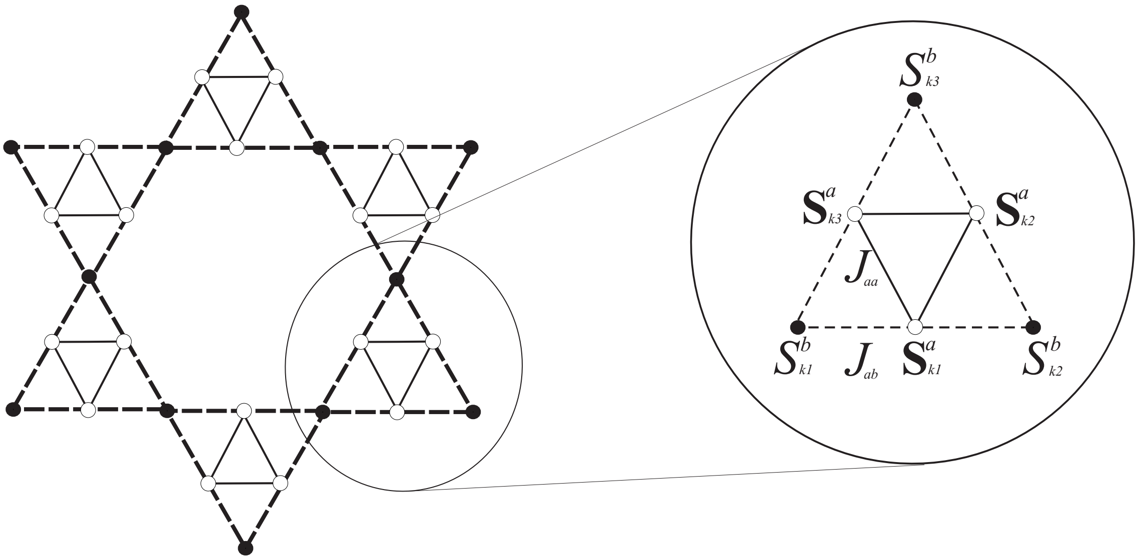

Figure 1.2: A cross-section of TKL structure. Solid lines represent the intra-trimer Heisenberg interactions J_{aa}, while the broken ones label monomer-trimer Ising interactions J_{ab}. The circle marks k-th cluster (Heisenberg trimer). $\mathbf{S}^a_{k_i}$ presents the Heisenberg and $S^b_{k_i}$ the Ising spins.

In what follows we shall mainly deal with the quantum entanglement properties of the spin-1/2 Ising-Heisenberg model on a generalized symmetrical diamond chain and on a triangulated Kagomé lattice.

Additionally, taking into account that each Heisenberg dimer of the diamond chain interacts with its neighboring dimer through the Ising-type, i.e. classical exchange interaction, we find that the states of two adjacent dimers become separable (disentangled) [1–3]. Thus, we can calculate the concurrence (a measure of pairwise entanglement [39,40]), which characterizes quantum features of the system, for each dimer separately. One of the main objectives of the next section is to reveal different regimes of the symmetrical diamond chain and to analyze new quantum effects (such as a double peak behavior in the concurrence versus temperature curves and existence of magnetic entanglement [19] of two different values). Note that one finds a similar situation with the triangulated Kagomé lattice: each a-type trimer interacts with its neighboring trimer through the Ising exchange interaction, therefore the states of two neighboring a-sublattices are separable.

The basic features of entanglement in spin-1/2 finite systems are fairly well understood by now (see e.g. [195, 196]), while the role of local cluster topology and spin correlations in thermodynamic limit still remain unanswered. There are some approximate methods, such as mean-field-like theories based on the Gibbs-Bogoliubov inequality, that one can invoke to deal with the cases like this, aimed at better understanding of different physical aspects [197–199]. This method can also be applied for studying thermal entanglement of many-body systems [200–202]. In spite of the method not being exact, it is still possible to observe regions of criticality [203].

In the case of the triangulated Kagomé lattice we can calculate concurrence, which characterizes quantum features, for each trimer separately in a self-consistent field. The key result of Sec. 1.3 is concentrated on the comparison of specific (peak and plateau) features in magnetization, susceptibility, specific heat and thermal entanglement properties in the above mentioned model using variational mean-field-like approximation based on Gibbs-Bogoliubov inequality. We will demonstrate how the order-disorder phase transition temperature is relevant to the the threshold temperature for vanishing of entanglement.

1.2 The spin-1/2 symmetrical diamond chain

1.2.1 Concurrence and thermal entanglement of the spin-1/2 Ising-Heisenberg model on a generalized symmetrical diamond

We consider the spin-1/2 Ising-Heisenberg model on a generalized symmetrical diamond chain ($J_1 = J_3 = J$), which consists of two non-equivalent types of sites, namely, the monomeric and dimeric ones (empty and full circles in Fig. 1.1, respectively). Within the proposed

Ising-Heisenberg model, the monomeric sites are occupied by Ising spins, while the dimeric nodes by Heisenberg ones. The Hamiltonian can be written as follows:

$$\begin{aligned}\mathcal{H}=\sum_{k=1}^{N}\mathcal{H}_k= \quad & \sum_{k=1}^{N}\left[J_2\mathbf{S}_{k_1}\mathbf{S}_{k_2}+J(\mu_k^z+\mu_{k+1}^z)(S_{k_1}^z+S_{k_2}^z)+\right.\\ & \left.+J_m\mu_k^z\mu_{k+1}^z-H\left(S_{k_1}^z+S_{k_2}^z+\frac{\mu_k^z+\mu_{k+1}^z}{2}\right)\right], \qquad (1.1)\end{aligned}$$

where the summation runs over clusters, depicted in Fig. 1.1. $\mathcal{H}_k$ represents the Hamiltonian of the $k-th$ cluster, $\mathbf{S}_k=(S_k^x,S_k^y,S_k^z)$ denotes the Heisenberg spin-1/2 operator and μ_k is the Ising variable. Knowing, that each Ising spin belongs simultaneously to two clusters, we take a 1/2 factor for the Ising spins in the last term of (1.1), which incorporates the effects of the external magnetic field. Positive values of J, J_2 and J_m correspond to antiferromagnetic couplings. Note that the system is strongly frustrated due to the chain's geometry and existence of competing interactions J, J_2 and J_m. When $J_1=J_3$ and $J_m=0$, we deal with the so-called ideal diamond chain [61–63]. Meanwhile, in a general case, when $J_1\neq J_3$, the symmetry of the system is broken and one obtains the distorted diamond chain (a detailed analysis of its thermodynamics can be found in Refs. [64, 187]). Before introducing the calculations and discussion we emphasize the fact which was already discussed in Sec. 1.1: the states of two neighboring Heisenberg dimers (with interaction J_2) are separable, because of a classical character of the coupling between them (by means of the Ising spin). Thus we can calculate the entanglement for each of the dimers individually. Note that a different approach of a mean-field-like treatment, based on the Gibbs-Bogoliubov inequality was used in Ref. [28], where all the couplings between the diamond chain sites were chosen to be of a quantum (Heisenberg-type) character.

For the construction of eigenvectors of each cluster we take into account that $\mathcal{H}_k$ possesses a symmetry corresponding to the permutations $\mu_k\leftrightarrow\mu_{k+1}$ and $\{\mu_k\leftrightarrow\mu_{k+1};\mathbf{S}_{k_1}\leftrightarrow\mathbf{S}_{k_2}\}$, which result in the following eigenvectors (hereafter, the letter k labels the number of the cluster; first bracket corresponds to the Heisenberg dimer):

$$
\begin{aligned}
\psi_1 &= \frac{1}{\sqrt{2}}(\uparrow_{k_1}\otimes\downarrow_{k_2}+\downarrow_{k_1}\otimes\uparrow_{k_2})\otimes\uparrow_k\uparrow_{k+1};\\
\psi_2 &= \frac{1}{\sqrt{2}}(\uparrow_{k_1}\otimes\downarrow_{k_2}+\downarrow_{k_1}\otimes\uparrow_{k_2})\otimes(\uparrow_k\downarrow_{k+1}+\downarrow_k\uparrow_{k+1});\\
\psi_3 &= \frac{1}{\sqrt{2}}(\uparrow_{k_1}\otimes\downarrow_{k_2}+\downarrow_{k_1}\otimes\uparrow_{k_2})\otimes(\uparrow_k\downarrow_{k+1}-\downarrow_k\uparrow_{k+1});\\
\psi_4 &= \frac{1}{\sqrt{2}}(\uparrow_{k_1}\otimes\downarrow_{k_2}+\downarrow_{k_1}\otimes\uparrow_{k_2})\otimes\downarrow_k\downarrow_{k+1};\\
\psi_5 &= \frac{1}{\sqrt{2}}(\uparrow_{k_1}\otimes\downarrow_{k_2}-\downarrow_{k_1}\otimes\uparrow_{k_2})\otimes\uparrow_k\uparrow_{k+1};\\
\psi_6 &= \frac{1}{\sqrt{2}}(\uparrow_{k_1}\otimes\downarrow_{k_2}-\downarrow_{k_1}\otimes\uparrow_{k_2})\otimes(\uparrow_k\downarrow_{k+1}+\downarrow_k\uparrow_{k+1});\\
\psi_7 &= \frac{1}{\sqrt{2}}(\uparrow_{k_1}\otimes\downarrow_{k_2}-\downarrow_{k_1}\otimes\uparrow_{k_2})\otimes(\uparrow_k\downarrow_{k+1}-\downarrow_k\uparrow_{k+1});\\
\psi_8 &= \frac{1}{\sqrt{2}}(\uparrow_{k_1}\otimes\downarrow_{k_2}-\downarrow_{k_1}\otimes\uparrow_{k_2})\otimes\downarrow_k\downarrow_{k+1}\\
\psi_9 &=\uparrow_{k_1}\otimes\uparrow_{k_2}\otimes\uparrow_k\uparrow_{k+1};\\
\psi_{10} &= \frac{1}{\sqrt{2}}\uparrow_{k_1}\otimes\uparrow_{k_2}\otimes(\uparrow_k\downarrow_{k+1}+\downarrow_k\uparrow_{k+1});\\
\psi_{11} &= \frac{1}{\sqrt{2}}\uparrow_{k_1}\otimes\uparrow_{k_2}\otimes(\uparrow_k\downarrow_{k+1}-\downarrow_k\uparrow_{k+1});\\
\psi_{12} &=\uparrow_{k_1}\otimes\uparrow_{k_2}\otimes\downarrow_k\downarrow_{k+1};\\
\psi_{k_{13}} &=\downarrow_{k_1}\otimes\downarrow_{k_2}\otimes\uparrow_k\uparrow_{k+1};\\
\psi_{14} &= \frac{1}{\sqrt{2}}\downarrow_{k_1}\otimes\downarrow_{k_2}\otimes(\uparrow_k\downarrow_{k+1}+\downarrow_k\uparrow_{k+1});\\
\psi_{15} &= \frac{1}{\sqrt{2}}\downarrow_{k_1}\otimes\downarrow_{k_2}\otimes(\uparrow_k\downarrow_{k+1}-\downarrow_k\uparrow_{k+1});\\
\psi_{16} &=\downarrow_{k_1}\otimes\downarrow_{k_2}\otimes\downarrow_k\downarrow_{k+1};
\end{aligned}
\tag{1.2}
$$

and the corresponding eigenvalues:

$$\begin{aligned}
&E_1=\frac{1}{4}\left(-2H+J_m+J_2\right); \quad E_2=E_3=-\frac{J_m-J_2}{4};\\
&E_4=\frac{1}{4}(J_m+J_2+2H); \quad E_5=\frac{1}{4}(-2H+J_m-3J_2);\\
&E_6=E_7=-\frac{J_m+3J_2}{4}; \quad E_8=\frac{1}{4}(2H+J_m-3J_2);\\
&E_9=-\frac{3H}{2}+\frac{J_m+J_2}{4}+J; \quad E_{10}=E_{11}=-H-\frac{J_m-J_2}{4};\\
&E_{12}=-\frac{H}{2}+\frac{1}{4}\left(J_m+J_2-4J\right); \quad E_{13}=\frac{H}{2}+\frac{1}{4}\left(J_m+J_2-4J\right);\\
&E_{14}=E_{15}=\frac{1}{4}(-J_m+J_2+4H); \quad E_{16}=\frac{3H}{2}+\frac{J_m+J_2}{4}+J.
\end{aligned} \tag{1.3}$$

Here we study a measure of pairwise entanglement, called *concurrence* $C(\rho)$ [39,40], which is defined as

$$C(\rho)=max\{\lambda_1-\lambda_2-\lambda_3-\lambda_4,0\}, \tag{1.4}$$

where λ_i's are the square roots of the eigenvalues of the corresponding operator for the density matrix

$$\tilde{\rho}=\rho_{12}(\sigma_1^y\otimes\sigma_2^y)\rho_{12}^*(\sigma_1^y\otimes\sigma_2^y) \tag{1.5}$$

in descending order. Since we consider bipartite entanglement, we should use the reduced density matrix ρ_{12}, by tracing out two (of four) spins of the cluster. The reduced density matrix ρ_{12} is defined as [204]

$$\rho_{12}=\sum_{\alpha}\langle\alpha|\rho|\alpha\rangle. \tag{1.6}$$

In this equation $|\alpha\rangle$ denotes basis vectors of the Hilbert space associated with the system, with respect to which the density matrix is reduced. The summation runs over all these basis vectors. Since in our case we make reduction with respect to two spins, $|\alpha\rangle=\{|\downarrow\downarrow\ \rangle,|\downarrow\uparrow\ \rangle,|\uparrow\downarrow\ \rangle,|\uparrow\uparrow\ \rangle\}$.

It is obvious that the only entangled pair is formed by the Heisenberg spins. Other pairs are disentangled (separable) because of the classical (diagonal) character of the Ising-type interaction between them. Hence we will be interested in the reduced density matrix, constructed by tracing out two Ising-type spins μ_k and μ_{k+1}. In other words, $\rho_{k_{12}}=\mathrm{Tr}_{\{\mu_k,\mu_{k+1}\}}\rho_k$ and the full density matrix ρ_k of the $k-th$ cluster is defined as (here and further Boltzmann constant is set to be $k_B = 1$)

$$\rho_k = \frac{1}{Z_k} \sum_{i=1}^{16} \exp(-E_i/T) |\psi_i\rangle\langle\psi_i|, \tag{1.7}$$

where Z_k is the partition function:

$$\begin{aligned} Z_k = \mathrm{Tr}\rho_k = \quad & e^{-\frac{6H+J_m+4J+J_2}{4T}} \left(2e^{\frac{H+J_m+2J}{2T}} + 2e^{\frac{3H+J_m+2J}{2T}} + \right. \\ & 2e^{\frac{5H+J_m+2J}{2T}} + 2e^{\frac{3H+J_m+2J+2J_2}{2T}} + e^{\frac{H+J}{T}} + e^{\frac{2(H+J)}{T}} + \\ & \left. e^{\frac{2H+J}{T}} + e^{\frac{H+2J}{T}} + e^{\frac{H+J+J_2}{T}} + e^{\frac{2H+J+J_2}{T}} + e^{\frac{3H}{T}} + 1 \right). \end{aligned} \tag{1.8}$$

Using the definition (1.6) and the basis vectors $|\alpha\rangle = \{| \downarrow\downarrow\rangle, | \downarrow\uparrow\rangle, | \uparrow\downarrow\rangle, | \uparrow\uparrow\rangle\}$, we obtain the reduced density matrix $\rho_{k_{12}}$ of the $k-th$ cluster:

$$\rho_{k_{12}} = \begin{pmatrix} u & 0 & 0 & 0 \\ 0 & w & y & 0 \\ 0 & y^* & w & 0 \\ 0 & 0 & 0 & v \end{pmatrix}, \tag{1.9}$$

where

$$\begin{aligned} u = \quad & 2e^{\frac{4H+J_m-J_2}{4T}} + e^{-\frac{-2H+J_m-4J+J_2}{4T}} + e^{-\frac{-6H+J_m+4J+J_2}{4T}}, \\ v = \quad & e^{-\frac{6H+J_m+4J+J_2}{4T}} \left(2e^{\frac{H+J_m+2J}{2T}} + e^{\frac{H+2J}{T}} + 1\right), \\ w = \quad & \tfrac{1}{2}\left(e^{\frac{J_2}{T}} + 1\right) e^{-\frac{2H+J_m+J_2}{4T}} \left(2e^{\frac{H+J_m}{2T}} + e^{H/T} + 1\right), \\ y = \quad & -\tfrac{1}{2}\left(e^{\frac{J_2}{T}} - 1\right) e^{-\frac{2H+J_m+J_2}{4T}} \left(2e^{\frac{H+J_m}{2T}} + e^{H/T} + 1\right). \end{aligned} \tag{1.10}$$

The density matrix $\rho_{k_{12}}$ in Eq. (1.9) has a form of a so-called X-state [205, 206], since the Hamiltonian $\mathcal{H}_k$ is translationary invariant with a symmetry $[S_z, \mathcal{H}_k] = 0$ ($S_z = 1/2(\mu_k^z + \mu_{k+1}^z) + S_{k_1}^z + S_{k_2}^z$) [207, 208]. The concurrence $C(\rho)$ of such an X-state density matrix has the following form [209]:

$$C(\rho) = \frac{2}{Z} max(|y| - \sqrt{uv}, 0). \tag{1.11}$$

It is worth to note here that the density matrix $\rho_{k_{12}}$ of any pair of spins, different from the Heisenberg dimer has no non-diagonal elements, responsible for the quantum correlations [see Eq. (1.11)]. Thus we conclude, that there is no entanglement between a pair of spins which contains at least one Ising spin.

In (1.2), one finds a set of states with maximum value of entanglement, for which the Heisenberg dimer is in a singlet or in a triplet state (ψ_i's with $i = 1, ..., 8$). As for the rest of the states (ψ_i's with $i = 9, ..., 16$) the Heisenberg dimer is in a separable state and therefore these ψ_i's are non-entangled ones.

1.2.2 The ideal diamond chain

In this subsection we proceed to the investigation of entanglement features of a dimeric unit of an ideal diamond chain ($J_m = 0$). Firstly, we study the behavior of $C(\rho)$ at $H = 0$. We discuss here three regimes, depending on the value of $J - J_2$: $J - J_2 > 0$, $J - J_2 < 0$ and $J - J_2 = 0$. In the first case, as one finds from (1.3), the ground state contains two-fold degenerate states ψ_{12} and ψ_{13}. Since these states are factorable, the corresponding dependency curve of $C(\rho)$ from temperature T starts from $C(\rho) = 0$ (Fig. 1.3). Furthermore, the entanglement can be invoked by increasing the temperature (for values of $J - J_2$ close to 0). This happens since the contribution of entangled states in the mixture ρ_k increases with the growth of temperature T. The local maximum, appearing here arises due to the optimal thermal mixing of all eigenstates in the system. This maximum becomes narrower and smaller and gradually vanishes by increasing $J - J_2$. Note that the value of $J - J_2$, corresponding to disappearing of $C(\rho)$ also depends on J_2 (e.g. for $J_2 = 1$, $J - J_2 \approx 0.2$). The latter becomes obvious, if one takes into account that J_2, being the coupling constant of the Heisenberg type interaction between dimeric units, is responsible for the strength of quantum correlations between Heisenberg spins. We emphasize here that in the case $J - J_2 > 0$ the system exhibits weak ($0 < J_2 < J$) or no frustration ($J_2 < 0$).

In the second case, when $J - J_2 < 0$, the model obviously manifests more of its quantum nature. Firstly, the dependency curve of $C(\rho)$ from temperature starts from $C(\rho) = 1$ at $T = 0$ (Fig. 1.3). This happens due to the fact that at a zero temperature the maximum entangled states ψ_5, ψ_6, ψ_7 and ψ_8 form four-fold degenerate ground state with the value

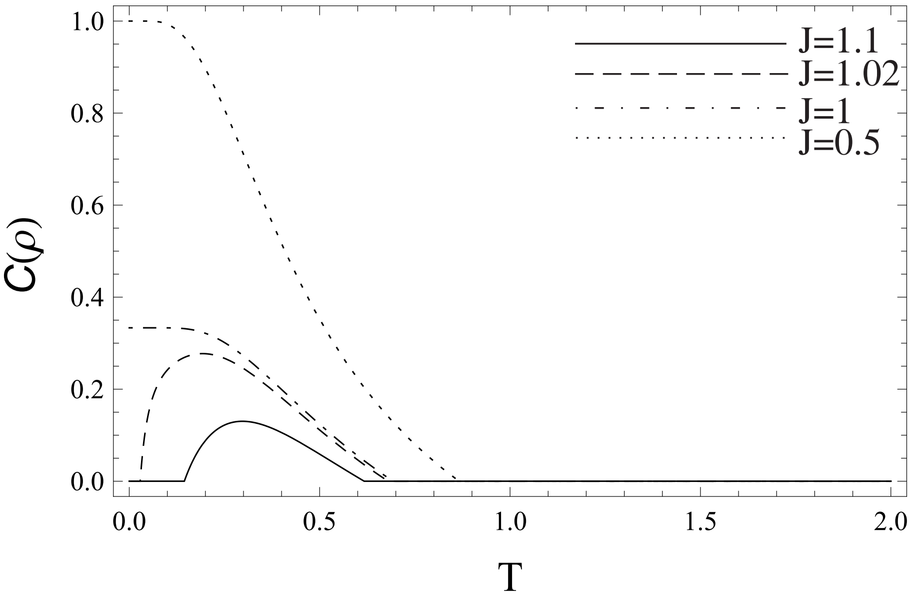

Figure 1.3: Concurrence $C(\rho)$ versus temperature T for $J_2 = 1$, $J_m = 0$, $H = 0$, and different values of J.

of $C(\rho) = 1$ for the corresponding reduced density matrix $\rho_{k_{12}}$. When the temperature is increased, the concurrence gradually disappears, because of the thermal mixing with other states of the system (including the factorable ones). The sudden-death temperature T_d, corresponding to the dying out of quantum correlations in the system can be found through the equation $C(\rho) = 0$. It has the following form:

$$x^{-J}\left(x^J + 1\right)^2 = 2\left|x^{J_2} - 1\right|, \tag{1.12}$$

where $x = e^{1/T}$. The solution can be presented as $T_d = J/\log a$ (when $J - J_2 < 0$), where a depends on the ratio parameter J_2/J. Increasing this ratio, a decreases, but the linear dependence on J remains (e.g. when $J_2/J = 2$, $a = \frac{1}{4}(3 + \sqrt{17})$).

Finally, the case $J - J_2 = 0$ can be regarded as a boundary case in the following sense. Here the ground state is six-fold degenerate, containing additionally ψ_{12} and ψ_{13}, besides ψ_5, ψ_6, ψ_7 and ψ_8 (in other words all the states from the previous two cases). Since ψ_{12} and ψ_{13} are factorable, this leads to lower entanglement of the ground state's reduced matrix, that is $C(\rho) = 1/3$ (Fig. 1.3). Moreover, the above discussed sudden-death temperature T_d is lower, than that for $J - J_2 < 0$ (although again $T_d = J/\log a$ with $a = 2 + \sqrt{5}$).

On the other hand, as it can be seen from Fig. 1.3, there are two sudden-death tempera-

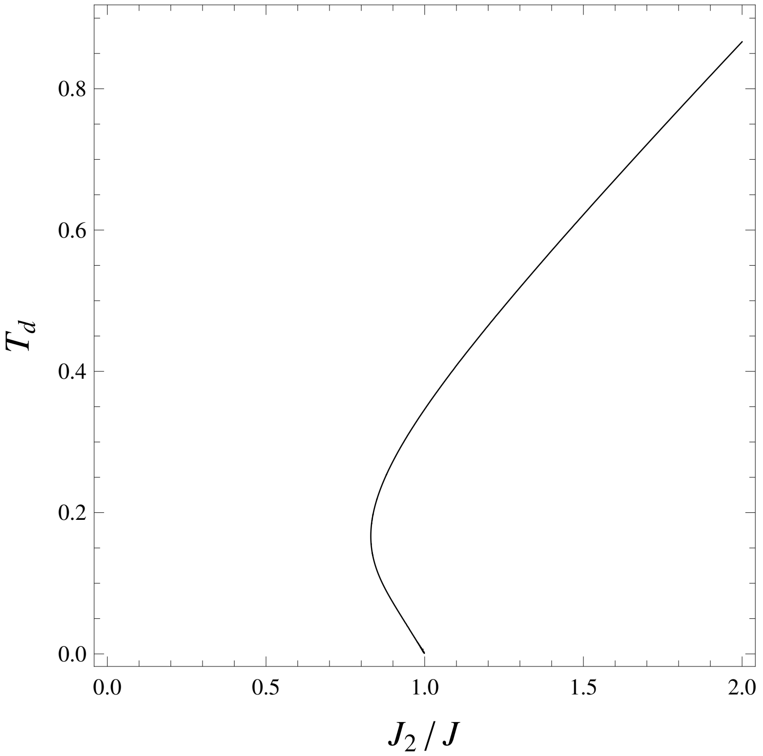

Figure 1.4: Sudden-death temperature T_d corresponding to the vanishing or arising of entanglement at a zero magnetic H versus the ratio parameter J_2/J ($J = 0.5$).

tures in the case $J - J_2 > 0$ (corresponding to arising and vanishing of entanglement) [196]. The dependence of T_d on the ratio parameter J_2/J is shown in Fig. 1.4. In the area $0 < J_2/J < 1$, there are two sudden-death temperatures, while for the values $J_2/J \geq 1$, the dependence is a linear one.

Our further investigation concerns the effects of the magnetic field H.

Firstly we discuss how the magnetic field affects the above introduced sudden-death temperature T_d. While increasing H, T_d also increases, but it always remains lower than $J_2/\log 3$ (more precisely $\lim_{H\to\infty} T_d = J_2/\log 3$). Another interesting fact is that the magnetic field gives rise to more than two sudden-death temperatures in the case $J - J_2 > 0$ [Fig. 1.5(a)] and on the dependence of $C(\rho)$ from temperature T one finds two peaks separated by an area of a zero entanglement [Fig. 1.5(b)]. With increasing H the smaller of aforementioned peaks tears apart from $C(\rho) = 0$, starts merging with the bigger one and eventually disappears. An effect of this kind has not been reported yet, to the best of our knowledge. Although a similar double peak behavior of concurrence was found in the dissipative Lipkin-Meshkov-Glick model versus *magnetic field* [210]. However, when $T \to 0$, $C(\rho)$ remains finite and becomes zero only

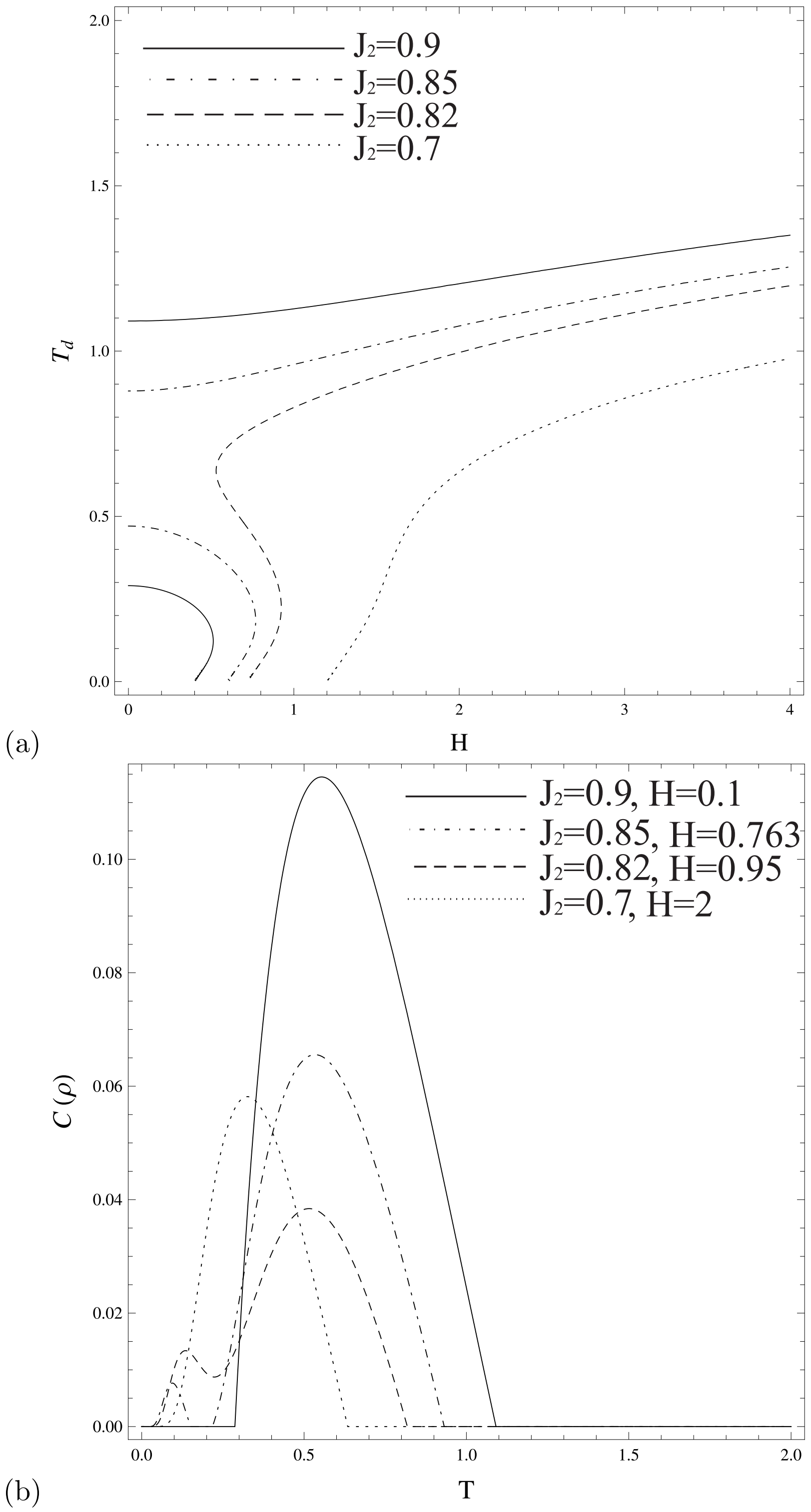

Figure 1.5: (a) Sudden-death temperature T_d corresponding to the vanishing or arising of entanglement versus magnetic field H for $J = 2$ and different values of J_2; (b) Concurrence $C(\rho)$ versus temperature T for $J = 2$ and different values of J_2 and magnetic field H.

at the absolute zero temperature $T = 0$ [i.e. there can be not more than three sudden-death temperatures corresponding to disappearing or arising of thermal entanglement, as it can be also seen form Fig. 1.5(a)]. In other words in the area of low temperatures the behavior of

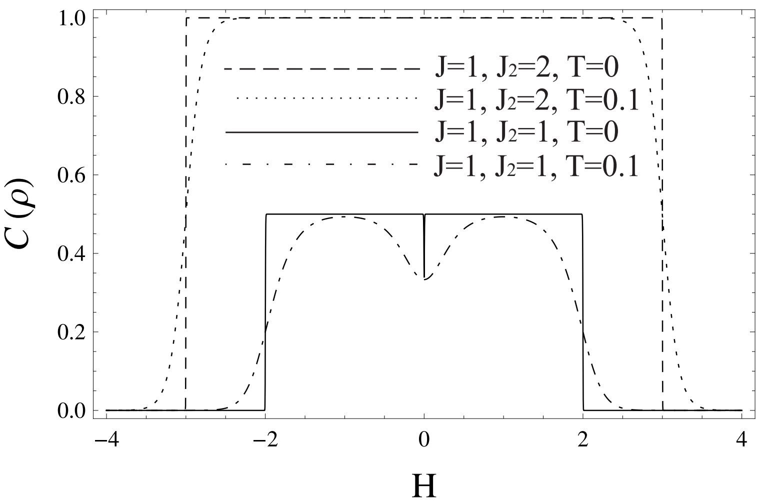

Figure 1.6: Concurrence $C(\rho)$ versus the magnetic field H for different values of the temperature, J_2 and J.

concurrence is smooth, in contrast with the case when magnetic field is absent.

Now, we concentrate on the dependence of $C(\rho)$ on the magnetic field. Because of the above introduced ground state structure, the dependency curve of $C(\rho)$ from magnetic field at zero temperature has a dip at $H = 0$ with $C(\rho) = 1/3$ for $J - J_2 = 0$. There is no dip if $J - J_2 < 0$ (Fig. 1.6). When Ising-type interaction is stronger than the Heisenberg one ($J - J_2 > 0$), one does not find a magnetic entanglement. Furthermore, magnetic entanglement is of a higher value than that at zero magnetic field in the case $J - J_2 = 0$. This happens due to the fact that ground state here is two-fold degenerated and contains ψ_5 and ψ_{12} with the value $C(\rho) = 1/2$ for the corresponding reduced density matrix. $C(\rho)$ becomes zero for the case $J - J_2 \leq 0$ at the values of H, corresponding to saturation field, that is when the non-entangled state $\uparrow\uparrow\uparrow\uparrow$ (in the area $H > 0$) or $\downarrow\downarrow\downarrow\downarrow$ (in the area $H < 0$) becomes the ground state. One can find the described values of H from the conditions $E_9 = E_5$ and $E_{16} = E_8$, giving $H_s^+ = J + J_2$ and $H_s^- = -J - J_2$, respectively. Thermal effects smoothes the step-like behavior of concurrence in the case when $J - J_2 \geq 0$ and induces thermal entanglement when $J - J_2 > 0$ (see Fig. 1.3). The further increase of temperature causes the quantum correlations eventually dying out for the both cases.

Summarizing, in Fig. 1.7 we also plot three-dimensional dependencies of the concurrence $C(\rho)$ versus temperature T and magnetic field H.

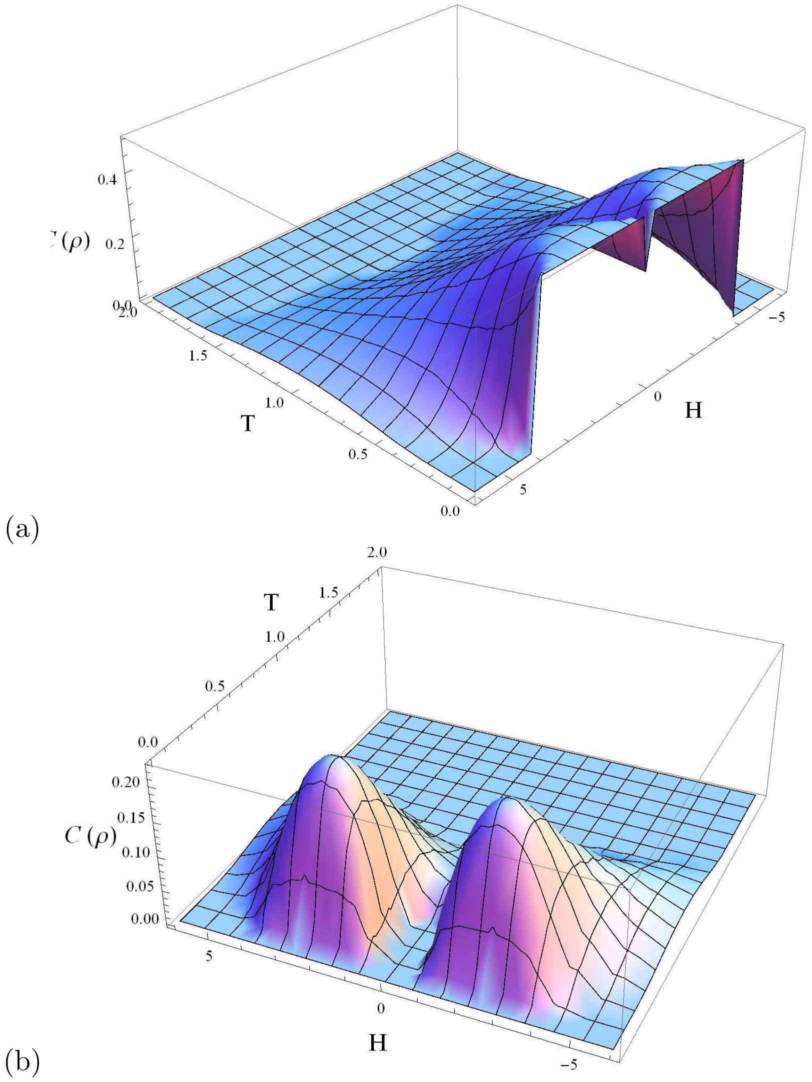

Figure 1.7: Concurrence $C(\rho)$ versus the magnetic field H and temperature T for (a) $J_2 = 2$ and $J = 2$; (b) $J_2 = 1.7$ and $J_1 = J_3 \equiv J = 2$.

1.2.3 Incorporation of J_m interaction

In this subsection we study the effects of the next-nearest neighbor interaction J_m between the Ising spins of the cluster, using the full expression for (1.10) and (1.11). We start with the discussion of the ground state structure for the case of $H = 0$ and $J - J_2 > 0$. It turns out that here one can distinguish two regimes. Firstly, when $0 < J_m < 2(J - J_2)$, the frustrated ground state contains two-fold degenerate ψ_{12} and ψ_{13} and thus the dependency curve of $C(\rho)$ from temperature starts up at $C(\rho) = 0$. However, the thermal effects can cause thermal entanglement for the values of J_m, close to $2(J - J_2)$ (but remaining $J_m < 2(J - J_2)$). One finds that $C(\rho)$ exhibits two sudden-death temperature behavior, that is also confirmed in

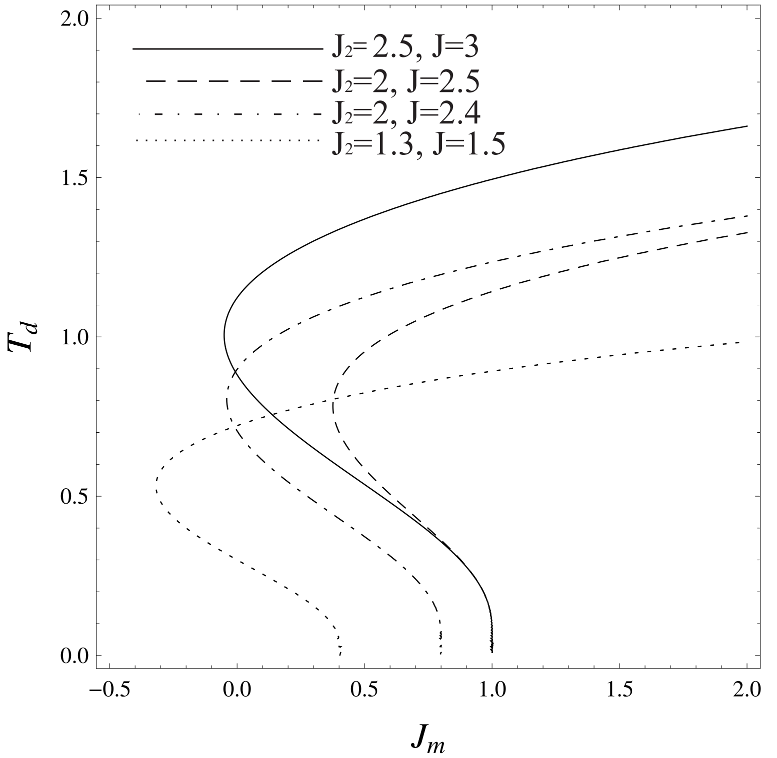

Figure 1.8: Sudden-death temperature T_d corresponding to the vanishing or arising of entanglement versus J_m for $H = 0$ and different values of J_2 and $J = 2$.

Fig. 1.8. This effect can be understood from the following discussion. The ground state consists of four-fold degenerate states ψ_6, ψ_7, ψ_{12} and ψ_{13}, for the case $J_m = 2(J - J_2)$. Although this mixture contains maximum entangled states ψ_6 and ψ_7, the corresponding density matrix for this ground state gives $C(\rho) = 0$. By increasing temperature, one obtains the thermal mixing of states which leads to a higher contribution of entangled states. This contribution, however, becomes less, when the values of J_m are considerably higher than $2(J - J_2)$. Thus, when increasing the difference of J_m and $2(J - J_2)$, the local maximum becomes narrower and eventually disappears.

In the opposite case, when $J_m > 2(J - J_2)$, the frustrated ground state is two-fold degenerate, but with ψ_6 and ψ_7, hence the above mentioned curve of $C(\rho)$ starts from $C(\rho) = 1$. We find only one sudden-death temperature here, which increases with the growth of J_m (Fig. 1.8). In other words, the qualitative picture remains the same as for the case $J_m = 0$.

Note that $C(\rho)$ is of a maximum value ($C(\rho) = 1$) at a zero magnetic field and a zero temperature, regardless of J_m for a dominant Heisenberg interaction ($J - J_2 < 0$).

Concluding the discussion of zero magnetic field properties in the case $J_m \neq 0$, we note

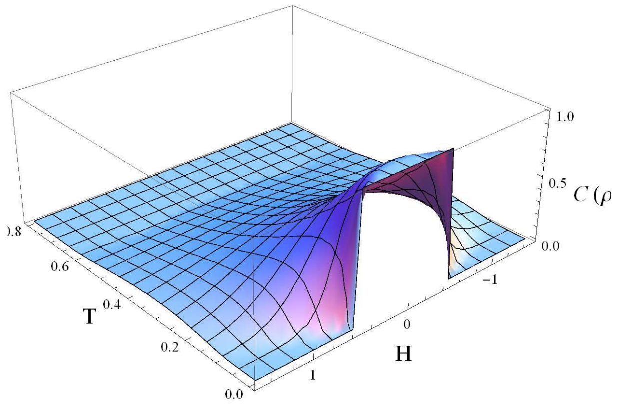

Figure 1.9: Concurrence $C(\rho)$ versus the magnetic field H and temperature T for $J_2 = 1$ and $J = 1.5$ and $J_m = 1.5$.

that when $J_m < 0$ (ferromagnetic coupling), the absolute value of J_m does not interfere with the ground state properties of the system (it is two-fold degenerate with ψ_{12} and ψ_{13}, if $J > J_2$, or ψ_5 and ψ_8, if $J < J_2$).

Here then, we discuss the regime $J - J_2 > 0$ introducing effects of the magnetic field H. We differentiate two subcases. First one, when $J_m \leq 2(J - J_2)$, one does not find magnetic entanglement in the system, since increasing the absolute value of magnetic field H, we obtain a sequence of separable states (e.g. $\psi_{12} \to (\psi_{10} + \psi_{11}) \to \psi_9$ or $\psi_{12} \to \psi_9$ for $H > 0$). Here and further by $(\psi_i + \psi_j)$ we mean two-fold degenerate states.

Meanwhile, when $J_m > 2(J - J_2)$, the aforementioned sequence of states starts from $(\psi_6 + \psi_7)$ with maximum value of $C(\rho) = 1$, therefore we obtain magnetic entanglement (Fig. 1.9). One can introduce here critical values of magnetic field H_c^+ and H_c^-, corresponding to vanishing of magnetic entanglement. In contrary with the case $J_m = 0$, $H_c^\pm$ does not coincide with the saturation fields $H_s^\pm$ (see Sec. 1.2.2).

On the one hand, we have the ground state transitions $(\psi_6+\psi_7) \to \psi_{12} \to (\psi_{10}+\psi_{11}) \to \psi_9$ (for $H > 0$) if the value of magnetic field, corresponding to the intersection of energies E_6 and E_{12}, is lower than that of E_{10} and E_{12} [Fig. 1.10(a)]. This condition gives: $J_m < 2J - J_2$. Thus the corresponding critical values of magnetic field can be found from $E_6 = E_{12}$ with $H_c^+ = 2J_2 - 2J + J_m$ (obviously, $H_c^- = -H_c^+$, from equation $E_6 = E_{13}$). On the other hand, when $J_m > 2J - J_2$, we have the ground state transitions $(\psi_6 + \psi_7) \to (\psi_{10} + \psi_{11}) \to \psi_9$ [Fig. 1.10(b)]. Corresponding $H_c^+ = J_2$, found from $E_6 = E_{10}$ ($H_c^- = -J_2$, from $E_6 = E_{14}$). The ground state transition $(\psi_6 + \psi_7) \to \psi_9$ can not occur, since the corresponding condition is inconsistent with $J_m > 2J - J_2$.

Following the same technique as in the previous paragraph (we do not stop on a detailed phase structure), we obtain the following regimes for $J - J_2 < 0$: $H_c^+ = H_s^+ = J + J_2$ ($H_c^- = -H_c^+$) in the case $J_m < J_2 - J$ and $H_c^+ = 2J_2 - J_m$ if $J_2 > J_m > J_2 - J$, and finally, when $J_m > J_2$ one finds $H_c^+ = J_2$.

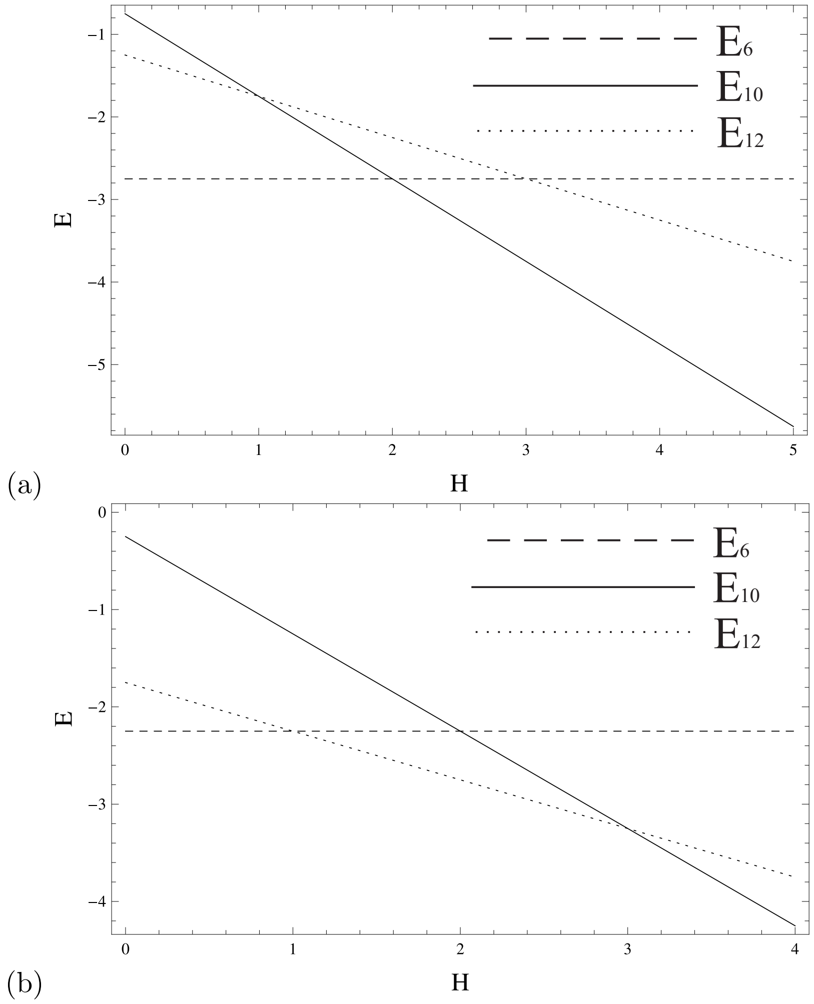

Figure 1.10: Eigenvalues E_6, E_{10} and E_{12} versus the magnetic field H for (a) $J_m > 2J - J_2$; (b) $J_m < 2J - J_2$.

The special (boundary) case $J - J_2 = 0$ and $J_m \neq 0$ is also of interest, since one can observe here magnetic entanglement of different values ($C(\rho) = 1$ and $C(\rho) = 1/2$) (Fig. 1.11), whereas in the case $J_m = 0$, these two regimes cannot coexist for a fixed values of J and J_2. This situation arises only for $0 < J_m < J$, when one finds the sequence of states $(\psi_6 + \psi_7) \longrightarrow (\psi_5 + \psi_{12}) \longrightarrow$(factorable state) (for $H > 0$). In other words, at the values of magnetic field $H = \pm J_m$ (found from conditions $E_6 = E_{12}$ for $H > 0$ and $E_6 = E_8$ for $H < 0$)

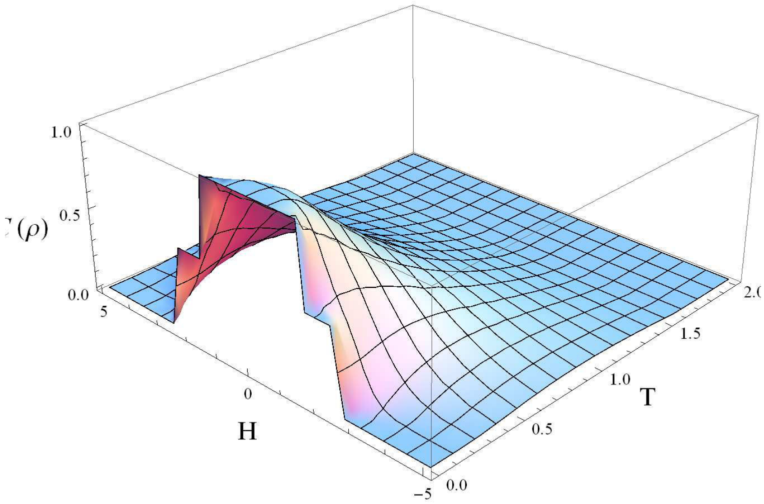

Figure 1.11: Concurrence $C(\rho)$ versus the magnetic field H and temperature T for $J_2 = 2$ and $J = 2$ and $J_m = 1.5$.

the states with different values of magnetic entanglement coexist.

As for the sudden-death temperature corresponding to the disappearing or arising of entanglement at non-zero magnetic field, one finds a similar behavior as in the case $J_m = 0$, i.e. here again we find up to three sudden-death temperatures (as in Fig. 1.5), with a double peak behavior on the dependency of $C(\rho)$ on temperature.

1.3 The triangulated Kagomé lattice

1.3.1 Isotropic Heisenberg model on triangulated Kagomé lattice

In this section we turn to the spin-1/2 Ising-Heisenberg model on a triangulated Kagomé lattice (TKL) (Fig. 1.2) consisting of two types of sites (a and b). Since the exchange coupling between Cu^{2+} ions are almost isotropic, the application of the isotropic, i.e., XXX Heisenberg model is more appropriate. There is a strong Heisenberg J_{aa} exchange coupling between trimeric sites of a type and weaker Ising-type one (J_{ab}) between trimeric a and monomeric b ones. Thus, the Kagomé lattice of the Ising spins (monomers) contains inside of each triangle unit a smaller triangle of the Heisenberg spins (trimer). The Hamiltonian can be written as follows:

$$\mathcal{H} = J_{aa}\sum_{(i,j)} \mathbf{S}^a_i \mathbf{S}^a_j - J_{ab}\sum_{(k,l)} (S^z)^a_k \cdot (S^z)^b_l - H\sum_{j=1}^{\frac{2N}{3}} 3[(S^z)^a_j + \frac{1}{2}(S^z)^b_j], \tag{1.13}$$

where $\mathbf{S}^a = \{S^a_x, S^a_y, S^a_z\}$ is the Heisenberg spin-1/2 operator, S^b is the Ising spin. $J_{aa} > 0$ corresponds to antiferromagnetic Heisenberg coupling and $J_{ab} > 0$ to ferromagnetic Ising-Heisenberg one. The first two summations run over $a - a$ and $a - b$ nearest neighbors respectively and the last sum incorporates the effect of uniform magnetic field (we have assumed that the total number of sites is $3N$).

1.3.2 Basic mean-field formalism

Here we apply the variational mean-field-like treatment based on Gibbs-Bogoliubov inequality [69, 70] to solve the Hamiltonian (1.13). This implies that the free energy (Helmholtz potential) of system is

$$F \leq F_0 + \langle \mathcal{H} - \mathcal{H}_0 \rangle_0, \tag{1.14}$$

where $\mathcal{H}$ is the real Hamiltonian which describes the system and $\mathcal{H}_0$ is the trial one. F and F_0 are free energies corresponding to $\mathcal{H}$ and $\mathcal{H}_0$ respectively and $\langle ... \rangle_0$ denotes the thermal average over the ensemble defined by $\mathcal{H}_0$. Following [68] we introduce the trial Hamiltonian in the following form:

$$\mathcal{H}_0 = \sum_{trimers} \mathcal{H}_{c_0}, \tag{1.15}$$

$$\mathcal{H}_{c_0} = \lambda_{aa}\left(\mathbf{S}^a_{k_1}\mathbf{S}^a_{k_2} + \mathbf{S}^a_{k_2}\mathbf{S}^a_{k_3} + \mathbf{S}^a_{k_1}\mathbf{S}^a_{k_3}\right) - \sum_{i=1}^{3}\left[\gamma_a (S^z)^a_{k_i} + \frac{\gamma_b}{2}(S^z)^b_{k_i}\right], \tag{1.16}$$

where the index k labels the number of a trimeric unit. In this Hamiltonian the stronger quantum Heisenberg antiferromagnetic interactions between a-sites are treated exactly, while the weaker Ising-type ones between a- and b-sites are replaced by self-consistent (effective) fields of two types: γ_a and γ_b. The variational parameters γ_a, γ_b and λ_{aa} can be found from the Bogoliubov inequality after minimizing the RHS of (1.14). Thus our focus is on the cluster depicted in Fig. 1.2. Each of the b-type spins belongs to two of such clusters simultaneously. Hence only the half of each b-spin belongs to one cluster and therefore there are $3 \cdot 1/2$ b-type spins in it. Consequently the total number of (a- and b-) spins in the cluster will be $3 + 3/2 = 9/2$ (there are 3 a-type spins in the triangle). Inequality (1.14) can be rewritten for the described cluster:

$$f \leq f_0 + \langle \mathcal{H}_c - \mathcal{H}_{c0} \rangle_0, \tag{1.17}$$

where $\mathcal{H}_c$ is the real and $\mathcal{H}_{c_0}$ the trial Hamiltonian of the cluster, f and f_0 free energies of the cluster defined by $\mathcal{H}_c$ and $\mathcal{H}_{c_0}$ respectively. Using the fact that in terms of (1.16) $\mathbf{S}^a$- and $\mathbf{S}^b$-type variables are statistically independent, one obtains $\langle \mathbf{S}^a \cdot \mathbf{S}^b \rangle_0 = \langle \mathbf{S}^a \rangle_0 \cdot \langle \mathbf{S}^b \rangle_0$. Besides, taking into account that $\langle (S^z)^a \rangle_0 = m_a$ (single a-site magnetization), $\langle (S^z)^b \rangle_0 = m_b$ (single b-site magnetization), we obtain the following expression:

$$\begin{aligned} f \leq\ & f_0 + (J_{aa} - \lambda_{aa}) \langle \mathbf{S}^a_{k_1} \mathbf{S}^a_{k_2} + \mathbf{S}^a_{k_2} \mathbf{S}^a_{k_3} + \mathbf{S}^a_{k_1} \mathbf{S}^a_{k_3} \rangle_0 \\ & -6 J_{ab} m_a m_b - 3 H m_a - F \tfrac{3 H m_b}{2} + 3 \gamma_a m_a + \tfrac{3 \gamma_b m_b}{2}. \end{aligned} \tag{1.18}$$

Now, by minimizing the right-hand side of inequality (1.18) with respect to γ_a, γ_b and λ_{aa} and using $\frac{\partial f_0}{\partial \gamma_a} = -3 m_a$, $\frac{\partial f_0}{\partial \gamma_b} = -3/2 m_b$, $\frac{\partial f_0}{\partial \lambda_{aa}} = \langle \mathbf{S}^a_{k_1} \mathbf{S}^a_{k_2} + \mathbf{S}^a_{k_2} \mathbf{S}^a_{k_3} + \mathbf{S}^a_{k_1} \mathbf{S}^a_{k_3} \rangle_0$, we determine the variational parameters in the form: $\lambda_{aa} = J_{aa}$, $\gamma_a = 2 J_{ab} m_b + H$, $\gamma_b = 4 J_{ab} m_a + H$. Parameters γ_a and γ_b, which have a meaning of a magnetic field, are interconnected, which is the consequence of their apparent self-consistency. The Hamiltonian $\mathcal{H}_0$ was chosen to be exactly solved. One finds that $\mathcal{H}_{c_0}$ can be divided into two parts corresponding to a- and b-type variables:

$$\begin{aligned} \mathcal{H}_{c_0} = & \left[\lambda_{aa} \{ \mathbf{S}^a_{k_1} \mathbf{S}^a_{k_2} + \mathbf{S}^a_{k_2} \mathbf{S}^a_{k_3} + \mathbf{S}^a_{k_1} \mathbf{S}^a_{k_3} \} - \sum_{i=1}^{3} \gamma_a (S^z)^a_{k_i} \right] - \sum_{i=1}^{3} \frac{\gamma_b}{2} (S^z)^b_{k_i} \\ & = \mathcal{H}^a_{c_0} + \sum_{i=1}^{3} (\mathcal{H}^b_{c_0})^i. \end{aligned} \tag{1.19}$$

Each of Hamiltonians $\mathcal{H}^a_{c_0}$ and $(\mathcal{H}^b_{c_0})^i$ can be solved separately (the variables have been separated). The eigenvalues of $\mathcal{H}^a_{c_0}$ are:

$$\begin{aligned}
&E_1 = \frac{3}{4}\left(\lambda_{aa} + 2\gamma_a\right); \quad E_2 = E_3 = \frac{1}{4}\left(-3\lambda_{aa} + 2\gamma_a\right); \\
&E_4 = \frac{1}{4}\left(3\lambda_{aa} + 2\gamma_a\right); \quad E_5 = E_6 = \frac{1}{4}\left(-3\lambda_{aa} - 2\gamma_a\right); \\
&E_7 = \frac{1}{4}\left(3\lambda_{aa} - 2\gamma_a\right); \quad E_8 = \frac{3}{4}\left(\lambda_{aa} - 2\gamma_a\right)
\end{aligned} \tag{1.20}$$

and the corresponding eigenvectors given by

$$\begin{aligned}
|\psi_1\rangle &= |000\rangle \\
|\psi_2\rangle &= \frac{1}{\sqrt{3}}\big(q|001\rangle + q^2|010\rangle + |100\rangle\big) \\
|\psi_3\rangle &= \frac{1}{\sqrt{3}}\big(q^2|001\rangle + q|010\rangle + |100\rangle\big) \\
|\psi_4\rangle &= \frac{1}{\sqrt{3}}\left(|001\rangle + |010\rangle + |100\rangle\right) \\
|\psi_5\rangle &= \frac{1}{\sqrt{3}}\big(q|110\rangle + q^2|101\rangle + |011\rangle\big) \\
|\psi_6\rangle &= \frac{1}{\sqrt{3}}\big(q^2|110\rangle + q|101\rangle + |011\rangle\big) \\
|\psi_7\rangle &= \frac{1}{\sqrt{3}}\left(|110\rangle + |101\rangle + |011\rangle\right) \\
|\psi_8\rangle &= |111\rangle,
\end{aligned} \tag{1.21}$$

where $q = e^{i2\pi/3}$ (these eigenvectors should be also the eigenstates of cyclic shift operator P with eigenvalues 1, q and q^2, satisfying $q^2 + q + 1 = 0$).

The partition function Z_{0_a} of the trimer in mean-field approximation is:

$$Z_{0_a} = \sum_{k=1}^{8} \exp(-E_k/T) = e^{-\frac{3\lambda_{aa}}{4T}} \left[\cosh\left(\frac{3\gamma_a}{2T}\right) + 2e^{\frac{3\lambda_{aa}}{2T}} \cosh\left(\frac{\gamma_a}{2T}\right) + \cosh\left(\frac{\gamma_a}{2T}\right)\right]. \tag{1.22}$$

Consequently the free energy of a-triangle will be:

$$f_{0_a} = -T\ln Z_{0_a} = \frac{3\lambda_{aa}}{4} - T\ln\left[\cosh\left(\frac{3\gamma_a}{2T}\right) + 2e^{\frac{3\lambda_{aa}}{2T}} \cosh\left(\frac{\gamma_a}{2T}\right) + \cosh\left(\frac{\gamma_a}{2T}\right)\right]. \tag{1.23}$$

Since the $(\mathcal{H}^b_{c_0})^i$ describes only half a particle (b-type spin), the Hamiltonian of one b-type spin will be $2 \cdot (\mathcal{H}^b_{c0})^i$. Hence, following the technique described above one finds the partition function Z_{0_b} and free energy f_{0_b} of a b-type spin in the adopted approximation:

$$Z_{0_b} = 2\cosh\left(\frac{\gamma_b}{2T}\right), \tag{1.24}$$

$$f_{0_b} = -T \ln\left[2\cosh\left(\frac{\gamma_b}{2T}\right)\right]. \tag{1.25}$$

As already mentioned, in terms of the trial Hamiltonian a- and b-type spins are statistically independent [see Eqs. (1.15), (1.16) and (1.19)]. Besides, b-type spins do not interact with each other. Therefore the partition function f_0 of the cluster in mean-field approximation reads:

$$f_0 = f_{0_a} + \frac{3}{2} \cdot f_{0_b}. \tag{1.26}$$

Consequently the free energy of the cluster f_{GB} in the mean-field approximation based on the Gibbs-Bogoliubov inequality will be:

$$\begin{aligned} f_{GB} = \quad & f_0 + \langle \mathcal{H}_c - \mathcal{H}_{c0} \rangle_0 = \frac{3\lambda_{aa}}{4} + 6J_{ab}m_a m_b - T\left[\ln\left\{4e^{\frac{3J_{ab}}{2T}}\cosh\left(\frac{\gamma_a}{2T}\right)\right.\right. \\ & \left.\left. +2\cosh\left(\frac{\gamma_a}{2T}\right) + 2\cosh\left(\frac{3\gamma_a}{2T}\right)\right\} + \frac{3}{2}\ln\left\{2\cosh\left(\frac{\gamma_b}{2T}\right)\right\}\right]. \end{aligned} \tag{1.27}$$

In Eq. (1.27) we have used the values of variational parameters γ_a, γ_b and λ_{aa}. Besides, due to the fact that there are $9/2$ spins in the cluster and therefore totally $2N/3$ clusters ($F_{GB} = 2N/3 \cdot f_{GB}$), we obtain:

$$\begin{aligned} \frac{F_{GB}}{N} = \quad & \frac{\lambda_{aa}}{2} + 4J_{ab}m_a m_b - 2T\left[\frac{1}{3}\ln\left\{4e^{\frac{3J_{ab}}{2T}}\cosh\left(\frac{\gamma_a}{2T}\right)\right.\right. \\ & \left.\left. +2\cosh\left(\frac{\gamma_a}{2T}\right) + 2\cosh\left(\frac{3\gamma_a}{2T}\right)\right\} + \frac{1}{2}\ln\left\{2\cosh\left(\frac{\gamma_b}{2T}\right)\right\}\right]. \end{aligned} \tag{1.28}$$

As for defined above a- and b-single site magnetizations we obtain:

$$m_a = -\tfrac{1}{3}\tfrac{\partial f_{0_a}}{\partial \gamma_a} = \tfrac{1}{6}\frac{3\sinh\left(\frac{3\gamma_a}{2T}\right)+2e^{\frac{3\lambda_{aa}}{2T}}\sinh\left(\frac{\gamma_a}{2T}\right)+\sinh\left(\frac{\gamma_a}{2T}\right)}{\cosh\left(\frac{3\gamma_a}{2T}\right)+2e^{\frac{3\lambda_{aa}}{2T}}\cosh\left(\frac{\gamma_a}{2T}\right)+\cosh\left(\frac{\gamma_a}{2T}\right)}, \tag{1.29}$$

$$m_b = -\tfrac{\partial f_{0_b}}{\partial \gamma_b} = \tfrac{1}{2}\tanh\left(\tfrac{\gamma_b}{2T}\right). \tag{1.30}$$

Notwithstanding of simplicity and the fact that the effective (self-consistent) field in zero magnetic field ($H = 0$) overestimates ferromagnetic correlations, it is still particularly useful for detection of spontaneous breaking SU(2) symmetry and possible temperature driven transitions in the frustrated spin systems (see Sec. 1.3.3). However, we also find that the strong quantum fluctuations, existing in the isotropic Heisenberg model in the absence of ferromagnetic type Ising term at $H = 0$ can restore the broken symmetry by providing stability to disordered spin-1/2 liquid state in frustrated geometries. Moreover, in general the presence of magnetic field ($H \neq 0$) suppresses the spin fluctuations and makes the self-consistent results more reliable and accurate [211]. Therefore, Eqs. (1.20), (1.21) and (1.27)-(1.30) with magnetic field are quite sufficient for understanding some intrinsic relationships between magnetic and entanglement properties [196] that naturally emerge in the Ising-Heisenberg model when one is complying with the variational mean-field-like procedure.

1.3.3 Magnetization

The results of the previous subsection can be used for investigation of the magnetic properties of the model. Here we are interested in the sublattice a properties, which, however, depend on parameters describing b-type spins. It is convenient to introduce a new (ratio) parameter $\alpha = J_{ab}/J_{aa}$. The magnetization curves can be found by solving numerically the transcendental equations (1.29) and (1.30). The magnetic field dependence of the magnetization per atom is plotted in Fig. 1.12 at $\alpha = 0.025$. We find that in the absence of magnetic field, the ordered ferromagnetic phase with spontaneous magnetization per site m_a is a stable ground state for all $|J_{ab}/J_{aa}|$ in spite of the high geometric frustration caused by the non-bipartite structure and antiferromagnetic intra-trimer interaction.

At relatively high temperatures the magnetization curve in Fig. 1.12(a) shows a monotonic behavior versus magnetic field with a full saturation at strong magnetic field. Upon decreasing the temperature a new partially saturated phase emerges in form of the (spin) plateaus shown in Fig. 1.12(b), which can be associated with staggered magnetization or short range antiferromagnetism (AF) in frustrated Kagomé geometry. Indeed, the appearance of plateau in magnetization curve at $m_a = 1/6$ can be explained as stability of trimeric a-sites in $\uparrow\uparrow\downarrow$ configuration. Thus, at rather low temperatures, the magnetization shows the finite leap across a plateau at $m_a = 1/6$ at infinitesimal magnetic field and below the critical field for

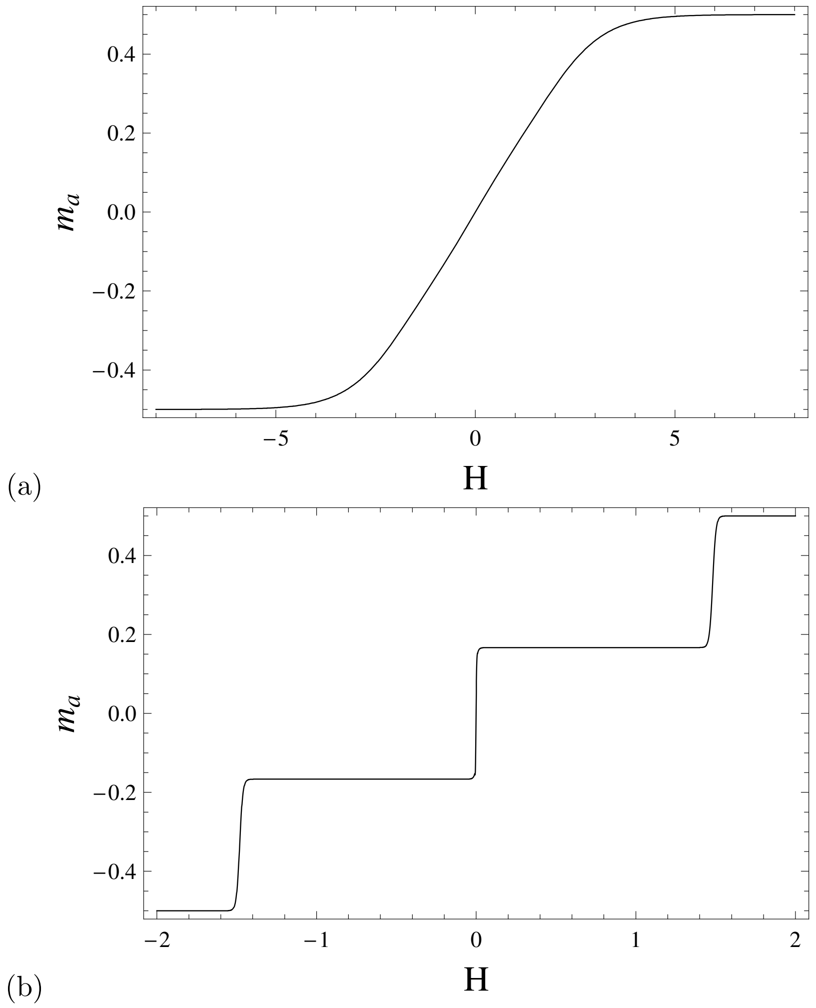

Figure 1.12: Single a-site magnetization m_a versus external magnetic field H for (a) $T = 0.7$ and (b) $T = 0.01$ for $\alpha = 0.025$, $J_{aa} = 1$. The magnetic field and temperature are in relative units of $k_B = 1$.

full saturation by flipping a down spin.

In Fig. 1.13 we also show the temperature dependence of the magnetization in equilibrium. As one can see from Fig. 1.13(a), in the absence of the external magnetic field the magnetization tends gradually to zero near the second-order transition temperature T_c between ordered ($m_a \neq 0$) and disordered ($m_a = 0$) phases. Hence, the magnetization m_a can be expanded into series near the critical temperature of second-order phase transition point:

$$m_a = am_a + bm_a^3 + cm_a^5 + ... \tag{1.31}$$

The critical temperature T_c corresponding to the second-order phase transition can be found from the condition $a = 1$, $b < 0$. In particular, for the case $J_{aa} = 1$ and $\alpha = 0.025$,

$T_c = 0.0102062$ (in relative units). At zero temperature in the absence of field we find unsaturated spontaneous ferromagnetism with $m_a = 1/6$ as a stable ground state.

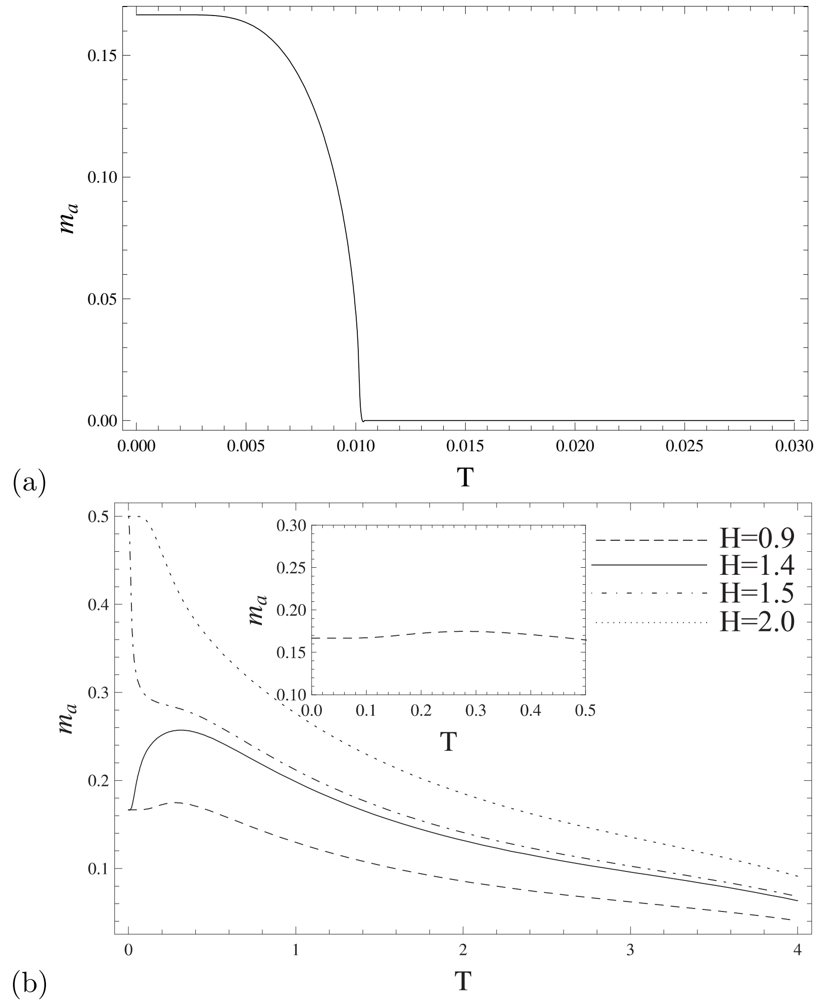

Figure 1.13: Single a-site magnetization m_a per atom versus temperature T for $J_{aa} = 1$, $\alpha = 0.025$ and (a) $H = 0$ and (b) different non-zero values of H (the inset shows details for the case $H = 0.9$ at low temperatures).

The magnetization in equilibrium as a function of temperature T at non-zero magnetic field [212] is plotted in Fig. 1.13(b). There are two distinct magnetic field regimes corresponding to $m_a = 1/6$ and saturated zero-temperature magnetization, $m_a = 1/2$. While fixed magnetic field H is less than the saturation magnetic field value, we deal with $m_a = 1/6$ regime. If we continue increasing the value of H, at the saturation magnetic field the magnetization jumps into $m_a = 1/2$ regime [$H = 1.5$, 2.0 in Fig. 1.13(b)]. There can be also seen a short plateau at $m_a = 1/6$ in the temperature dependence [$H = 0.9$ in Fig. 1.13(b)]. The peaks in the case of low magnetic fields arise due to the frustration effects.

1.3.4 Susceptibility

We define the magnetic susceptibility χ_a as

$$\chi_a = \frac{\partial m_a}{\partial H}. \tag{1.32}$$

First we examine the zero-field susceptibility, which is introduced as follows:

$$\chi_{a_0} = \left.\frac{\partial m_a}{\partial H}\right|_{H=0}. \tag{1.33}$$

The temperature dependence of χ_{a_0} in equilibrium is plotted in Fig. 1.14. The zero-field susceptibility χ_{a_0} diverges at the critical temperature T_c which is a signature of the second order phase transition discussed earlier (see Sec. 1.3.3). The temperature dependence of susceptibility χ_a at $H \neq 0$ [213] is presented in Fig. 1.15(a).

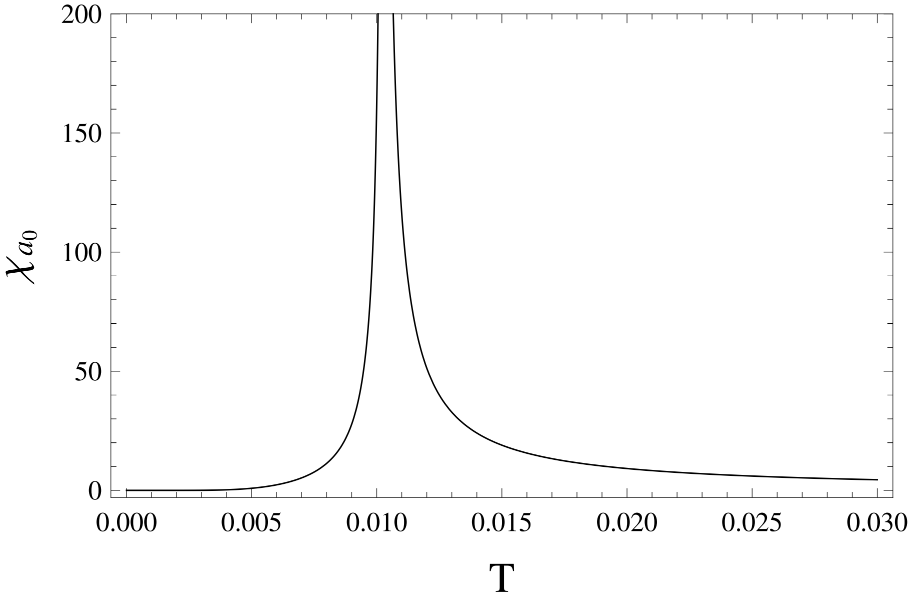

Figure 1.14: Zero-field susceptibility χ_{a_0} versus temperature T for $J_{aa} = 1$ and $\alpha = 0.025$.

The temperature dependence of magnetic susceptibility observed in [214] for $[\mathrm{Ni(H_2L^2)}]_4$ $[\mathrm{Cr(CN)_6}]_5\mathrm{OH} \cdot 15\mathrm{H_2O}$ compounds resembles the result shown in Fig. 1.14.

Notice, that at high temperatures the external field dependence of the magnetic susceptibility [Fig. 1.15(b)] exhibits one peak. With decreasing temperature, two peaks, symmetric with respect to $H = 0$, begin to arise, which correspond to the formation of the incipient (magnetization) plateau at $m_a = 1/6$. With decreasing further temperature the peaks

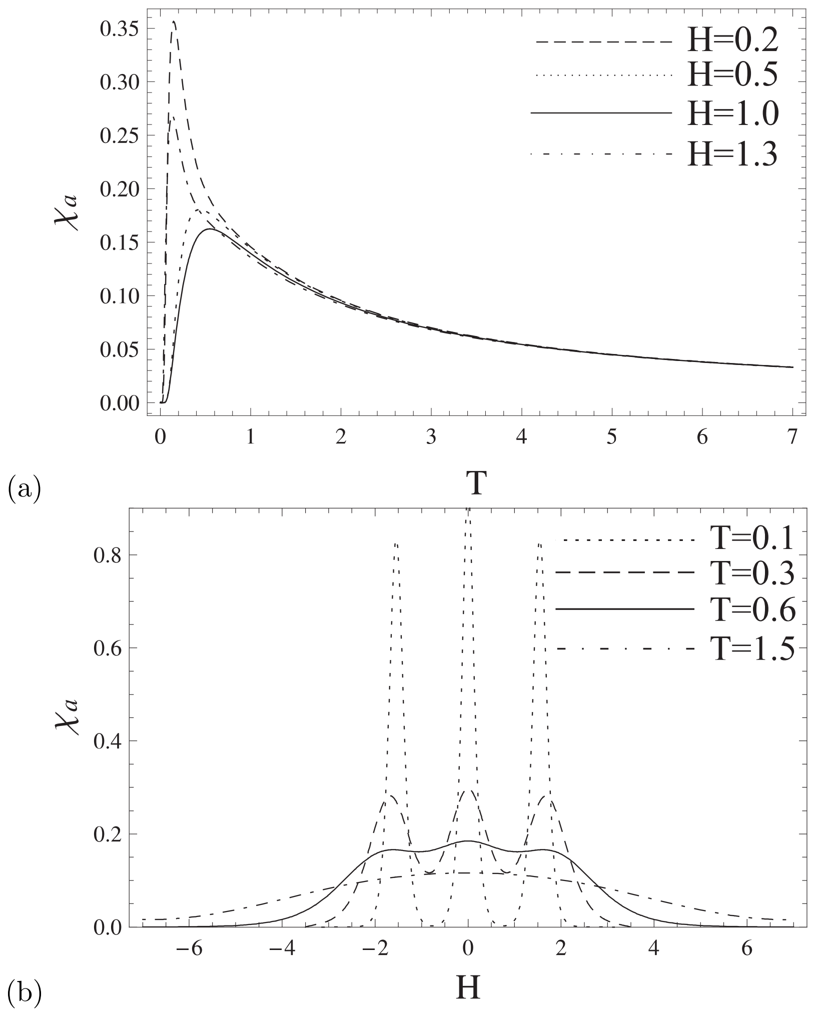

Figure 1.15: Susceptibility χ_a versus (a) temperature T at different H and (b) magnetic field H at different T for $J_{aa} = 1$, $\alpha = 0.025$.

become sharper and bigger in their magnitude.

1.3.5 Specific heat

The internal energy u and the specific heat $c(T)$ per cluster site are, respectively, determined as

$$u = -T^2 \frac{\partial}{\partial T} \left(F_{GB} / 3NT \right) \tag{1.34}$$

$$c(T) = \frac{\partial u}{\partial T} = -\frac{T}{3N} \frac{\partial^2 F_{GB}}{\partial T^2}, \tag{1.35}$$

F_{GB} taken from (1.28).

The behavior of the specific heat in equilibrium at the absence of the external magnetic

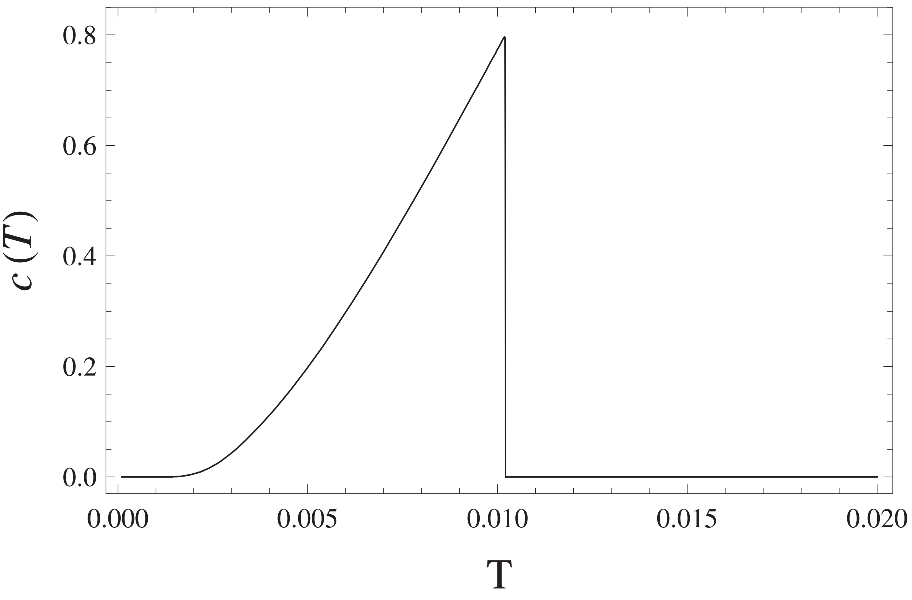

Figure 1.16: The zero-field specific $c(T)$ heat versus temperature T for $J_{aa} = 1$, $\alpha = 0.025$.

field ($H = 0$) is shown in Fig. 1.16. In this plot one can find the presence of second order phase transition: at the same temperature T_c, described in last two subsections, the specific heat has discontinuity.

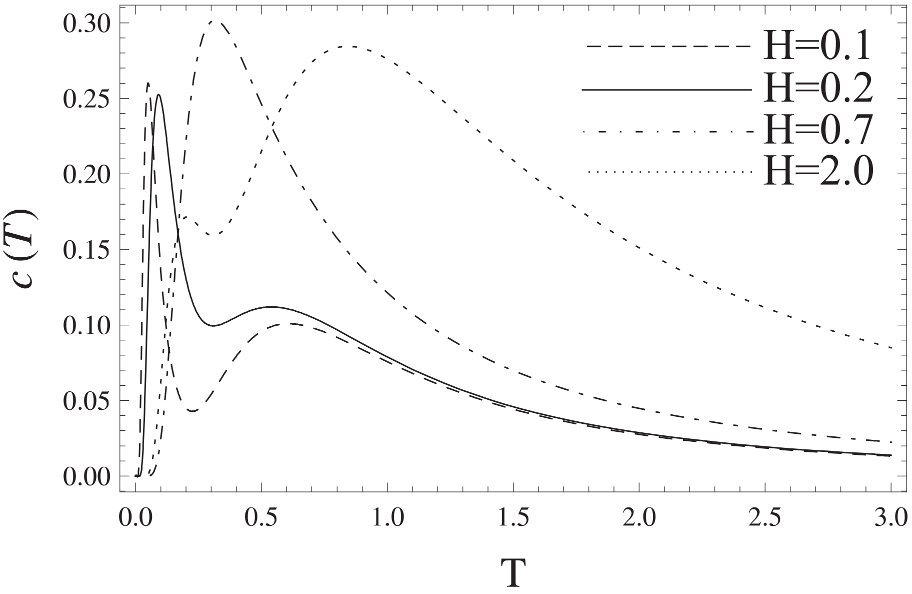

Figure 1.17: Specific heat $c(T)$ versus temperature T for $J_{aa} = 1$, $\alpha = 0.025$ and different H values.

The temperature dependence of the specific heat at non-zero magnetic field is shown in Fig. 1.17. Notwithstanding the observation of one peak in the $c(T)$ at $H = 0$ the temperature dependence of specific heat at $H \neq 0$ exhibits two-peak behavior peculiar to one and quasi one dimensional systems as one can find in [65, 215–217]. A double-peak structure in the specific heat manifests the existence of two energy scales in the system as a result of two competing orders [218]. Upon increasing the external magnetic field, the peak moves to higher-temperature region and, at the same time, decreases in amplitude. At higher values of H close to the transition from $m_a = 1/6$ to saturated $m_a = 1/2$ state the second broad peak gradually increases.

In Secs. 1.3.7 and 1.3.8 we further discuss magnetic properties by comparison with thermal entanglement.

1.3.6 Concurrence and thermal entanglement

The mean-field-like treatment of (1.13) transforms many-body system to reduced "single" cluster study in a self-consistent field where quantum interactions exist. This allows to study, in particular, (local) thermal entanglement properties of a-sublattice in terms of three-qubit XXX Heisenberg model in effective magnetic field γ_a, which carries the main properties of the system. Besides, because of the self-consistency and interconnection of the fields γ_a and γ_b the effective γ_b field has an impact on the concurrence, too. We study concurrence $C(\rho)$ as in Sec. 1.2.1, to quantify entanglement. Since we consider pairwise entanglement, we use the reduced density matrix $\rho_{12} = \mathrm{Tr}_3\rho$ ($\mathrm{Tr}_3\rho$ denotes the partial trace operation of the matrix ρ with respect to the third spin). Before introducing the calculations and discussion we emphasize the fact which was already discussed in Sec. 1.1: the states of two neighboring a-type trimers are separable (disentangled). Hence we can calculate the concurrence for each of them on cluster level individually in effective magnetic field. In our case the density matrix has the following form

$$\rho = \frac{1}{Z_{0a}} \sum_{k=1}^{8} \exp(-E_k/T)|\psi_k\rangle\langle\psi_k|, \tag{1.36}$$

E_k, $|\psi_k\rangle$ and Z_{0a} are taken from Eqs. (1.20), (1.21) and (1.22) respectively. The construction process of the reduced density matrix does not depend on whether γ_a is an effective or a real magnetic field, although the presence of effective field γ_a plays crucial role for the self-consistent solution. Here we skip the specific details and provide the result of final calculations of the matrix ρ_{12}, taking into account that the Hamiltonian $\mathcal{H}_{c_0}$ is translationary invariant with a symmetry $[S_z, \mathcal{H}_{c_0}] = 0$ ($S_z = \sum_{k=1}^{3} (S_z)^a_{k_i}$). Hence [207, 208]:

$$\rho_{12} = \begin{pmatrix} u & 0 & 0 & 0 \\ 0 & w & y & 0 \\ 0 & y^* & w & 0 \\ 0 & 0 & 0 & v \end{pmatrix}, \tag{1.37}$$

where

$$u = \frac{1}{3} e^{\frac{2\gamma_a - 3\lambda_{aa}}{4T}} \left(1 + 3e^{\frac{\gamma_a}{T}} + 2e^{\frac{3\lambda_{aa}}{2T}}\right) \tag{1.38}$$

$$v = \frac{1}{3} e^{-\frac{3(2\gamma_a + \lambda_{aa})}{4T}} \left(3 + e^{\frac{\gamma_a}{T}} + 2e^{\frac{2\gamma_a + 3\lambda_{aa}}{2T}}\right) \tag{1.39}$$

$$w = \frac{1}{3} e^{-\frac{2\gamma_a + 3\lambda_{aa}}{4T}} \left(1 + e^{\frac{\gamma_a}{T}}\right) \left(1 + 2e^{\frac{3\lambda_{aa}}{2T}}\right) \tag{1.40}$$

$$y = -\frac{1}{3} e^{-\frac{2\gamma_a + 3\lambda_{aa}}{4T}} \left(1 + e^{\frac{\gamma_a}{T}}\right) \left(-1 + e^{\frac{3\lambda_{aa}}{2T}}\right). \tag{1.41}$$

The concurrence $C(\rho)$ of the density matrix ρ_{12} is given in Eq. (1.11):

$$C(\rho) = \frac{2}{Z} max(|y| - \sqrt{uv}, 0). \tag{1.42}$$

Finally, we consider transcendental equations (1.29) and (1.30) by taking into account the values of variational parameters: $\lambda_{aa} = J_{aa}$, $\gamma_a = 2J_{ab}m_b + H$, $\gamma_b = 4J_{ab}m_a + H$, and, therefore, one can use these parameters to calculate $C(\rho)$. First, we study the behavior of $C(\rho)$ at $H = 0$. The temperature dependence of $C(\rho)$ is shown in Fig. 1.18.

Notice, the "triangle-in-triangle" system can display (bipartite) entanglement described by concurrence even in the absence of external magnetic field. It is important to mention that this result does not contradict to the well-known fact that there is no (bipartite) entanglement, measured by concurrence in isotropic three-qubit XXX Heisenberg model in zero magnetic field ($H = 0$) [196]. Indeed this effect is due to the existence of Ising-type interaction replaced by effective field $\gamma_a = 2J_{ab}m_b + H$ acting upon a-spins. The latter, in addition to H contains another quantity having meaning of magnetic ($2J_{ab}m_b$), which is non-zero at $H = 0$.

Another important observation is that threshold temperature (or the sudden-death temperature T_d) at which entanglement $C(\rho)$ disappear is identical to the critical temperature

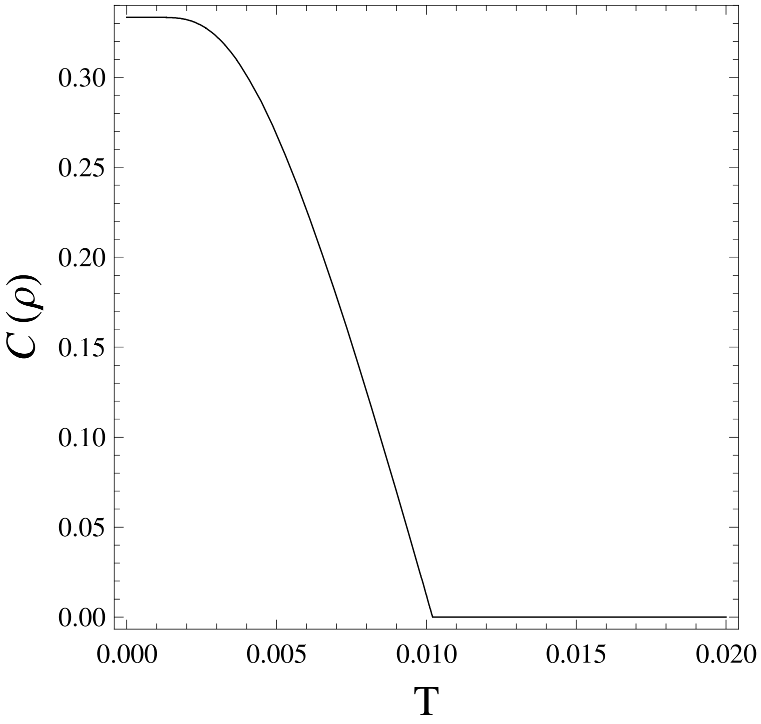

Figure 1.18: Concurrence $C(\rho)$ versus temperature T for $J_{aa} = 1$, $\alpha = 0.025$ and $H = 0$

T_c of second order phase transition between ordered and disordered phases described earlier in Sec. 1.3.5. This implies that the concurrence vanishes precisely at T_c, the same temperature of specific heat discontinuity. This is the consequence of the fact that at T_c the system undergoes order-disorder phase transition and the second term in γ_a vanishes, too ($m_b = 0$, when $H = 0$ and $T \geq T_c$). This factor implies the strong relationship between magnetic and entanglement properties of the system. In Fig. 1.19 we present the three dimensional plot of the concurrence as a function of the temperature and external magnetic field. We will discuss some of these features in behavior of concurrence $C(\rho)$ for studying magnetic and entanglement thermal properties in Secs. 1.3.7 and 1.3.8.

1.3.7 Common features of magnetic properties and entanglement: finite temperatures

In this subsection we discuss some similarities of magnetic statistical properties and quantum entanglement.

First, we consider for general J_{aa} and H the susceptibility (1.32) as a statistical characteristic. Figure 1.20(a) shows the density distribution of susceptibility reduced per one

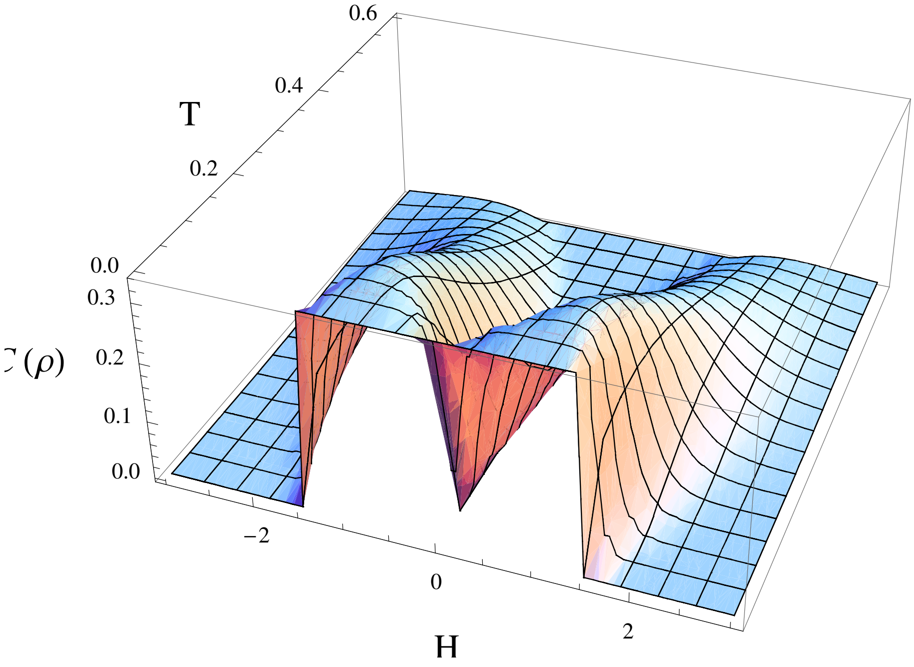

Figure 1.19: Concurrence $C(\rho)$ versus temperature T and external magnetic field H for $J_{aa} = 1$, $\alpha = 0.025$.

a-site as a function of the coupling constant J_{aa} and the external field H, at a relatively high temperature $T = 0.1$, which is higher than T_c. The white stripes on the figure correspond to peaks of the susceptibility. These stripes have a certain finite width due to nonzero temperature. For consistency in Fig. 1.20(b) a similar plot of concurrence density is shown for the same values of $(J_{aa}; H)$ parameters. The existence of entanglement in the infinite XXX Heisenberg chains of spins-1/2 and spins-1 was pointed in [29]. Here weak probe fields have been aligned along three orthogonal directions (x, y and z), supposing that magnetic susceptibility is equal in all these directions ($\chi_x = \chi_y = \chi_z$) and using the fact that $\chi_x + \chi_y + \chi_z$ is an entanglement witness. In our case there is a magnetic field aligned in the z-direction only, therefore $\chi_z \equiv \chi_a$. And we show that the behavior of susceptibility χ_z is similar to that of bipartite entanglement. Indeed, comparison of Figs. 1.20(a) and 1.20(b) shows that the general behavior of the statistical and entanglement properties, such as susceptibility (χ_a) and concurrence ($C(\rho)$), coincide. Our calculations show that the values of variables for the maximum (peak) in magnetic susceptibility correspond to the critical values on the $(J_{aa}; H)$ diagram at which the quantum coherence disappears and concurrence vanishes ($C(\rho) = 0$). However, this picture for the Ising-Heisenberg model on the TKL lattice can applied only for antiferromagnetic coupling $J_{aa} > 0$, while for ferromagnetic coupling $J_{aa} < 0$ the system always remains disentangled.

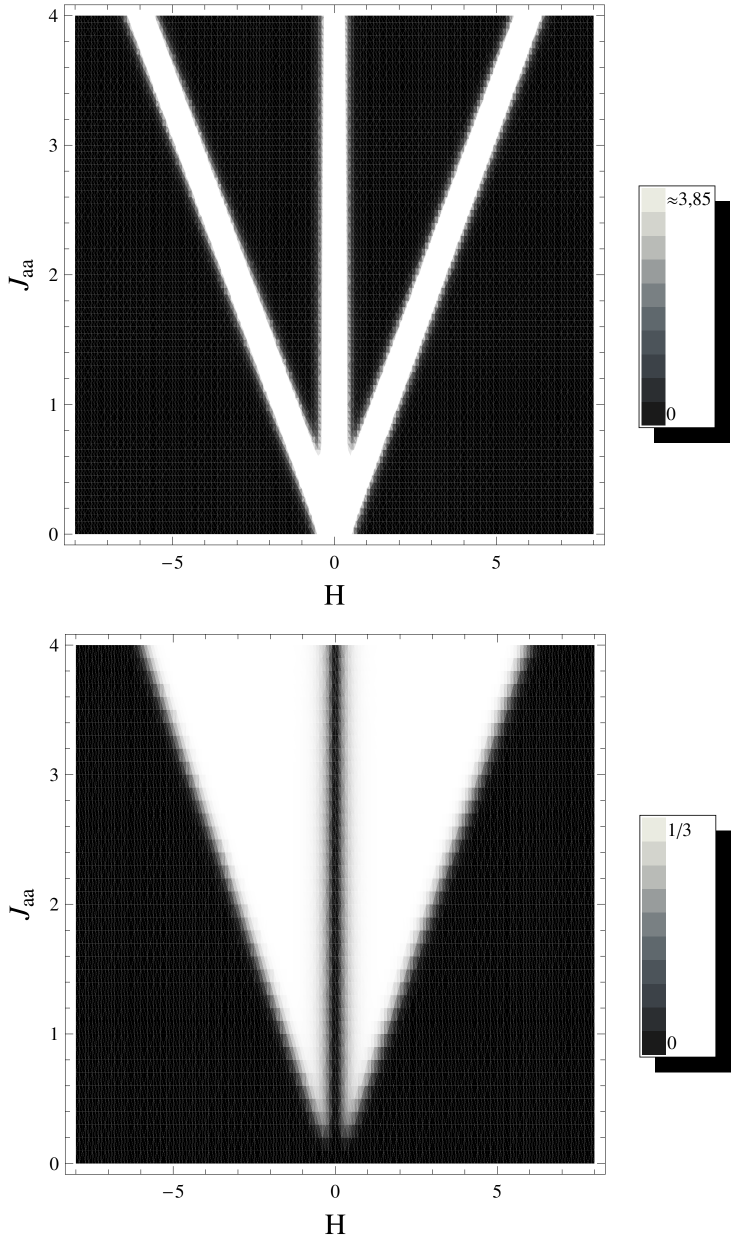

(a)

(b)

Figure 1.20: Density plot for (a) susceptibility χ_a and (b) concurrence $C(\rho)$ versus magnetic field H and coupling constant J_{aa} at $\alpha = 0.025$ and $T = 0.1$.

For further comparison we show for various temperatures in Figs. 1.21(a) and (b) the corresponding dependencies of the concurrence and heat capacity on magnetic field H.

In Fig. 1.21(a) at relatively low temperatures the specific heat exhibits a six peak structure located symmetrically with respect to the magnetic field ($H = 0$). As temperature increases, the middle peaks (on both sides of the $H = 0$) split and merge with the left and right peaks in the neighbor areas, near $H = 0$. At higher temperatures, the two other peaks on both

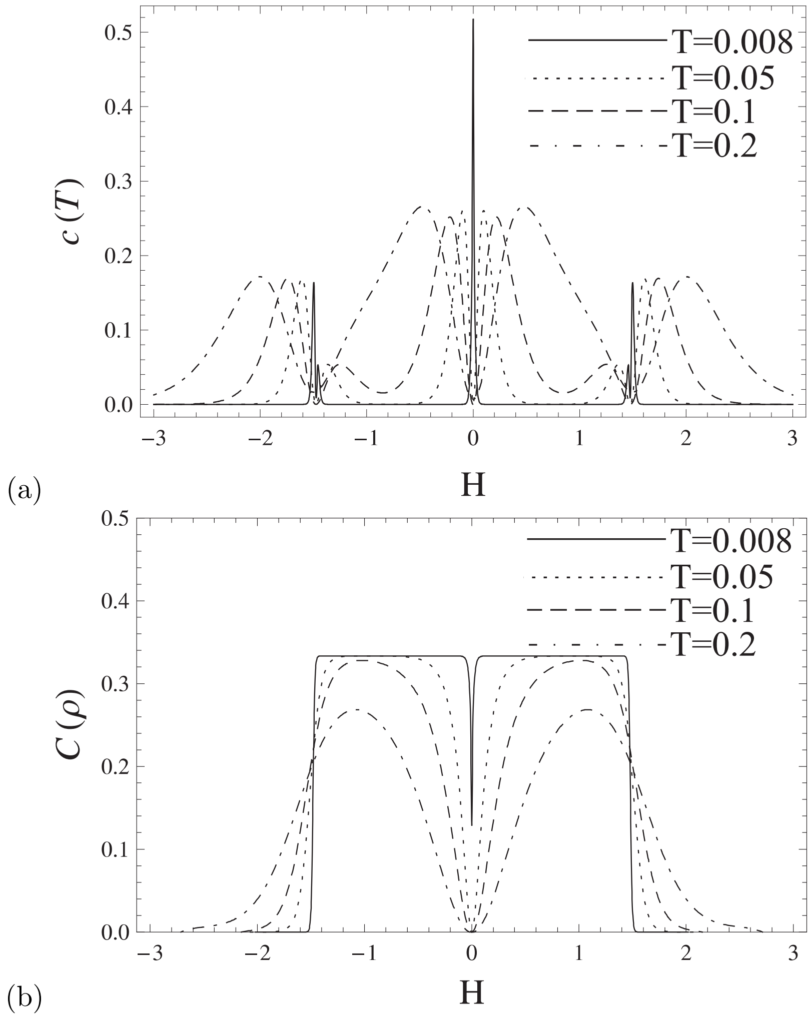

Figure 1.21: (a) Specific heat $c(T)$ and (b) concurrence $C(\rho)$ versus external magnetic field H for $J_{aa} = 1$, $\alpha = 0.025$.

sides of $H = 0$ also merge in one. As temperature increases there remain only two peaks, i.e., the sharp peak structure gradually disappears.

At low temperatures close to T_c ($T > T_c$), the two most distant peaks from the $H = 0$ (on each side of H) in Fig. 1.21(a) are approaching closer to each other, but do not merge in one. Meanwhile, the closest ones to the $H = 0$ peak (on either side of H) become narrower and approach closer to the origin, $H = 0$. For $T \lesssim T_c$, some features are resulting from the effective Ising field: the local minimum of the curve $c(T)$ at $H = 0$ becomes non zero, $c(T)|_{H=0} \neq 0$. With further decreasing temperature, the heat capacity in the vicinity of $H = 0$ displays one narrow peak (whereas in a normal three-qubit Heisenberg model there are two symmetrical peaks and $c(T)|_{H=0} = 0$). Nevertheless, the described extreme effects do not affect the behavior of the entanglement (concurrence), which is a purely quantum feature:

the curve is smooth enough for all $T > T_c$. However, $C(\rho)$ behaves as a step-like function by approaching closer to critical temperature T_c. At temperatures below the critical value, a local dip minimum is non zero, $C(T)|_{H=0} \neq 0$ (see also Fig. 1.18). This dip disappears at $T \approx 0.002$ by forming a single flat plateau at $T = 0$.

Our results on Gibbs-Bogoliubov treatment of coupled spins controlled by external magnetic field provide understanding of the magnetic ground state properties in "triangles-in-triangles" $Cu_9X_2(cpa)_6$ Kagomé series described in Refs. [75, 76]. This simple approach can also explain several interesting properties, such as double peaks of the specific heat, different competing (magnetic) orders, a 1/3 magnetization plateau and susceptibility peaks for the pulse field reported for classical and quantum Kagomé lattice magnets in [219]. In the end of the subsection, we emphasize that although introduced (effective) self-consistent γ_a and γ_b fields break the symmetry against $H = 0$, this does not act upon concurrence and specific heat.

1.3.8 Zero temperature entanglement and modulated phases

In this subsection the magnetization and entanglement properties of a-sublattice are considered at zero temperature using variational mean-field approximation. In Fig. 1.22(a) a phase diagram of constant magnetization is shown for a-sublattice. This diagram differentiates the following phases: Phase **I** corresponds to the single a-site magnetization $m_a = 1/6$, when spins in a-sublattice are in $\uparrow\uparrow\downarrow$ configuration; Phase **II** corresponds to $\downarrow\downarrow\uparrow$ configuration with the single a-site magnetization $m_a = -1/6$. These phases exist only for the antiferromagnetic coupling, $J_{aa} > 0$. For the ferromagnetic case ($J_{aa} < 0$) in **III** and **IV** regions we get spin saturation, with maximum $m_a = 1/2$ ($\downarrow\downarrow\downarrow$) and minimum $m_a = -1/2$ ($\uparrow\uparrow\uparrow$) magnetization per atom respectively.

Phase **I** contains the two-fold degenerate states $|\psi_5\rangle$ and $|\psi_6\rangle$, while Phase **II** – the two-fold degenerate states $|\psi_2\rangle$ and $|\psi_3\rangle$. By constructing the reduced density matrix in Phases **I** and **II**, one can find these phases in maximum entangled state, $C(\rho) = 1/3$. Phases **III** and **IV** correspond to $|\psi_1\rangle$ and $|\psi_8\rangle$ states respectively. These phases are disentangled, $C(\rho) = 0$. In Fig. 1.22(b) the concurrence density distribution is shown versus coupling constant (J_{aa}) and magnetic field (H) at zero temperature. The area of non-zero entanglement coincides with the phase $\mathbf{I}+\mathbf{II}$, where $|m_a| = 1/6$, while the one with zero entanglement ($C(\rho) = 0$) corresponds to the phase $\mathbf{III}+\mathbf{IV}$ with $|m_a| = 1/2$.

Notice, the plateau behavior in magnetization corresponds to constant entanglement values in corresponding density plots. The plateau in magnetization at $|m_a| = 1/6$ corresponds to maximum entanglement value, $C(\rho) = 1/3$, where the saturated phase at $|m_a| = 1/2$ is disentangled, $C(\rho) = 0$. This descriptive picture is also available at the non-zero temperature. At relatively low temperatures the plateau of magnetization at $|m_a| = 1/6$ and entanglement coincide, except the narrow region in the vicinity of $H = 0$ border. By decreasing the temperature, the middle stripe in Fig. 1.20(b) narrows and gradually disappears (see Fig. 1.22(b) and also Sec. 1.3.7). This trend becomes apparent by comparison of Figs. 1.20(b) and 1.23. The latter represents the density distribution of m_a magnetization at considerably low temperature $T = 0.1$. In Fig. 1.23 the grey areas describe the plateau at $|m_a| = 1/6$, while black and white regions correspond to saturated states, $|m_a| = 1/2$. White regions in Fig. 1.23 correspond to the plateau behavior in the concurrence. As the temperature increases the borders between distinct (different) phases are gradually smeared out. Summarizing, the structure of each of the Heisenberg trimers has the crucial impact on the phase diagram in Fig. 1.22(a): the geometrical structure of a-sublattice is responsible for the frustration effects arising in the antiferromagnetic Heisenberg model (geometrical frustration). This leads to above mentioned ground states with definite values of concurrence in Fig. 1.22(b). The ground state concurrence arises on magnetization plateaus at $|m_a| = 1/6$ (see Fig. 1.12(b) for non-zero temperatures), which is a consequence of strong geometrical frustration of a-sublattice. While the octahedron environment (b-sites) are responsible for the effective field only.

1.4 Summary

1. We studied the thermal entanglement of a spin-1/2 Ising-Heisenberg model on a symmetrical diamond chain and on a triangulated Kagomé lattice. The first one was proposed to understand frustrated magnetism of a series of compounds, like $A_3Cu_3(PO_4)_4$ with A=Ca, Sr, $Bi_4Cu_3V_2O_{14}$, $Cu_3(TeO_3)_2Br_2$ and $Cu_3(CO_3)_2(OH)_2$, while the sec-

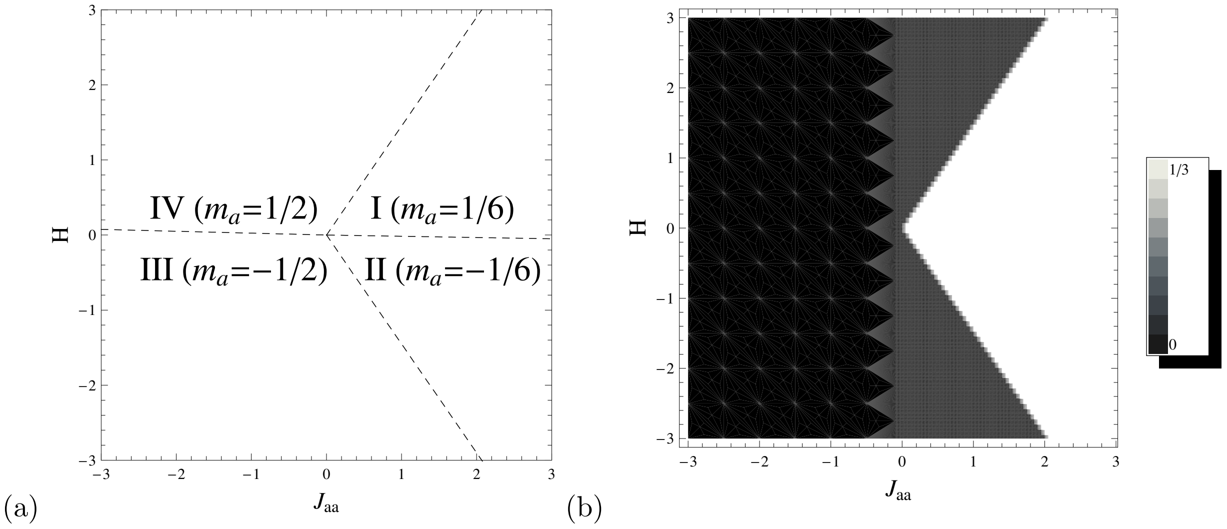

Figure 1.22: (a) Phase diagram of a-sublattice for $|\alpha| = 0.025$ and (b) density plot of concurrence $C(\rho)$ versus magnetic field H and coupling constant J_{aa} for $|\alpha| = 0.025$ at zero temperature.

ond one describes properties of $Cu_9X_2(cpa)_6 \cdot nH_2O$ polymeric coordination compounds (X = F, Cl, Br and cpa=carboxypentonic acid).

2. For the diamond chain it we showed that the magnetic field can lead to another, yet not described effect of double peak behavior of concurrence $C(\rho)$ versus *temperature* with three sudden-death temperatures (one of them corresponding to reappearance of concurrence and the other two to its disappearing). Another novel effect was indicated for the boundary case $J = J_2$ when $0 < J_m < J$. Specifically, two states with different values of magnetic entanglement coexist for the value of magnetic field $H = \pm J_m$.

3. We found strong correlations between magnetic properties and quantum entanglement in the spin-1/2 Ising-Heisenberg model on a triangulated Kagomé lattice. The ratio $\alpha = J_{ab}/J_{aa} = 0.025$ (J_{aa} labels intra-trimer Heisenberg, while J_{ab} monomer-trimer Ising interactions) is considered, which guaranties experimental realization for suitable theoretical treatment. We adopted variational mean-field-like treatment (based on Gibbs-Bogoliubov inequality) of separate clusters in effective interconnected fields of two types (consisting of Heisenberg a-trimers and Ising-type b-monomers). Moreover, we found an entanglement resource at a zero magnetic field, which is absent in system of a free Heisenberg trimer.

4. In addition, the entangled-disentangled phases in concurrence and ordered-disordered

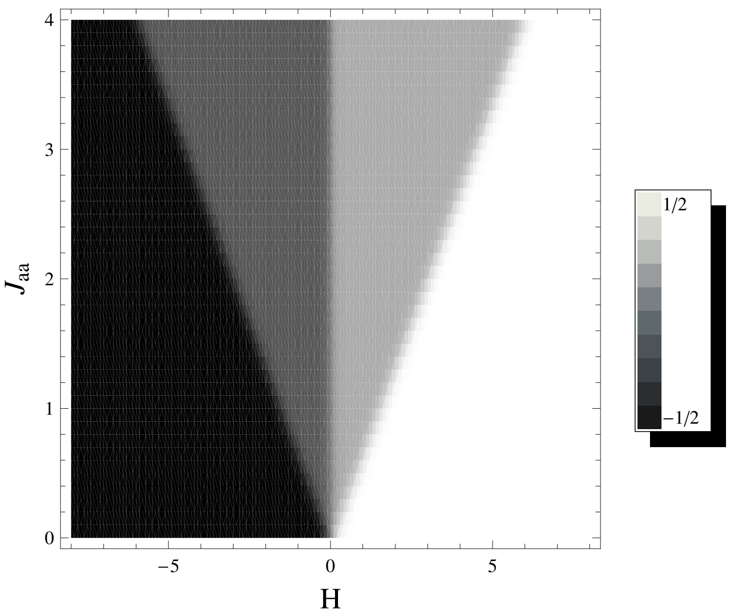

Figure 1.23: Density plot of magnetization m_a versus magnetic field H and coupling constant J_{aa} for $\alpha = 0.025$ and $T = 0.1$.

phases in quantum phase transitions share many common features. The threshold (sudden-death) temperature for concurrence is identical to the critical temperature of the (smooth) second order phase transition. Besides the entanglement and thermodynamic properties exhibit also common (plateau and peak) behavior in magnetization, susceptibility and concurrence.

Chapter 2

THE CLASSICAL LIMIT OF EXCHANGE INTERACTIONS AND CHAOTIC BEHAVIOR [1]

2.1 Introduction

As already mentioned in the Introduction of the present thesis, the problems of frustrated magnetism, interaction of atoms with fields and quantum information theory are strongly interconnected. However, a detailed analysis of complete models with pure quantum interactions is difficult to fulfill and in some cases is even unattainable. In the previous chapter we demonstrated one of the possible ways of overcoming the above mentioned difficulties, namely, introducing intermediate Ising spins in the sites of a magnetic lattice as a barrier for quantum fluctuations. Another method is to approximate the pure quantum Heisenberg model with the Ising one in the strong magnetic field regime. Specifically, if the magnetic field is directed along the z-axis, a reduction of transverse fluctuations occurs, and the S^x and S^y-spin components, becoming infinitely small, can be neglected [77, 78]. Consequently, models become exactly solvable in some particular cases, which leads to analytic expressions for thermodynamic quantities of interest.

Note that the dynamical approach plays a crucial role here: it is an essential tool in

---

[1] The results considered in this chapter are published in Refs. [163–166].

the theory of phase transitions and criticality [83, 84, 220–223]. It greatly enhanced our understanding of phase structure and critical properties of spin and gauge models. The method is widely used for exact solution of spin models on hierarchical lattices, which are good approximations for real existing ones (the so-called Bethe-Peierls approximation) [79–82, 163, 164]. This technique can be also applied to the generalized Bethe lattice (Husimi lattice) to describe properties of frustrated systems with multisite interactions, and RNA-like polymers [86–88]. The multisite interaction Ising and Q-state Potts models are of particular interest here. The first one is efficient in the analyzes of magnetic properties of solid ^{3}He [78, 85]. On the other hand, as already mentioned in the Introduction, the Potts model is associated with a number of physical phenomena. It plays a key role in the theory of magnetism. Additionally, being well defined for non-integer values of Q, it describes the helix-coil phase transitions for polypeptides and proteins [92, 93], the resistor network, dilute spin glass and self organizing critical systems, when $Q < 2$.

In the present chapter we consider the three site interaction Ising and the Q-state Potts models ($Q < 2$) on Husimi and Bethe lattices, respectively (Fig. 2.1). A distinguishable feature of these systems is their exact solvability through the recurrence relation technique. Within this method, statistical properties of a system are defined by one- or multidimensional rational mappings [78–80, 83–87, 163, 164]. In the case of antiferromagnetic coupling between lattice nodes, both models exhibit a complex behavior, featuring doubling bifurcations, chaotic regimes, intermittency, and superstable cycles.

In what follows we address to the phase structure of the Q-state Potts (QSP) and the three site interaction Ising (TSAI) models and to the analysis of one-dimensional rational mappings determining their properties. The bifurcation points of these maps correspond to points of phase transitions with a change of a symmetry [87, 163, 164, 223, 224]. Apart of looking at the phase transition mechanism in the conventional period doubling regime of the QSP model, we additionally study the chaotic−modulated phase transition in the three-periodic window through a tangent bifurcation [225, 226] for both QSP and TSAI models. Note that such windows were revealed and studied both theoretically and experimentally in a number of other systems of applied interest [227–229]. In the three-periodic window we point out some peculiar features of the above models, such as a chaotic regime confined inside

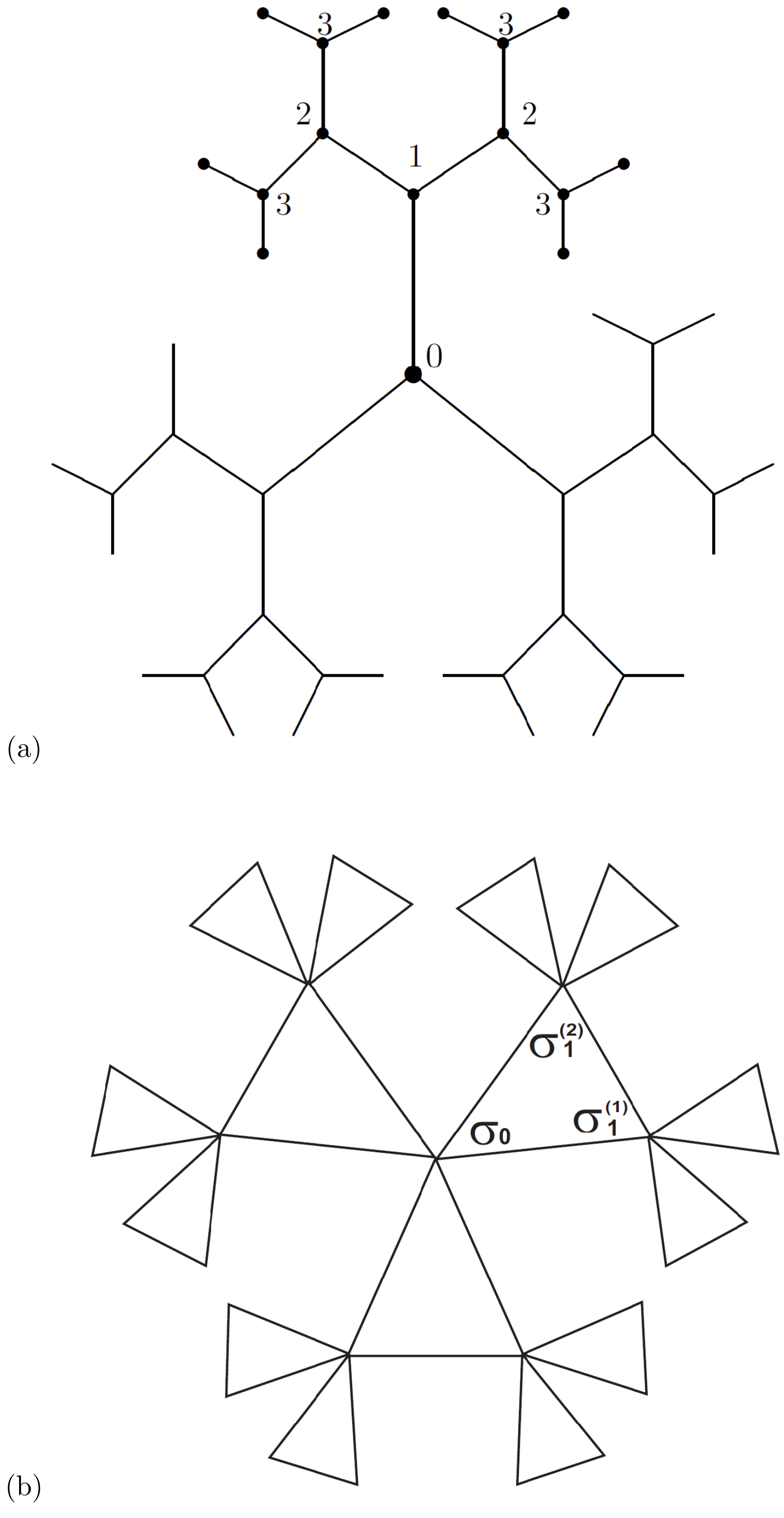

Figure 2.1: The Bethe (a) and the Husimi (b) lattices with coordination number $\gamma = 3$.

the window or a three-periodic window represented within a finite number of 3×2^n-periodic cycles. To the best of our knowledge this kind of behavior has not been described for rational mappings yet and was not observed in statistical models before.

Another tool in the investigation of bifurcation (phase transition) points and in distinguishing chaotic and periodic regimes, is the Lyapunov exponent. It serves not only as a good order parameter, but also gives a relevant information about the geometrical and dynamical properties of a model's attractor [230–232].

Additionally, we address to the concepts of Scaling and Universality which have played an essential role in the description of statistical systems [233]. Particularly, we study the behavior of Feigenbaum exponents [234, 235] for the rational mapping of the QSP model on a Bethe lattice and prove their convergence to the well-known values. Note that a similar analysis was made for the TSAI model on a Husimi lattice, confirming the above universality hypothesis [224]. It is interesting to note that the universality of Feigenbaum exponents can also be used as an approximate tool for construction of curves of phase transitions between different modulated phases [163]. Furthermore, the rate of convergence of these exponents affects the validity of the approximation much. Thus we find another motivation of analyzing the behavior of Feigenbaum hypothesis for the present statistical model.

2.2 The Q-state Potts model on a Bethe lattice

2.2.1 Rational mapping for the Potts model and its phase structure

The Q-state Potts model on a Bethe lattice [Fig. 2.1(a)], with two-site interactions and in presence of an external magnetic field is defined by the Hamiltonian [236]

$$\mathcal{H} = -J \sum_{(i,j)} \delta(\sigma_i, \sigma_j) - H \sum_i \delta(\sigma_i, Q). \tag{2.1}$$

The first sum in Eq. (2.1) goes over all nearest-neighbor pairs and the second one over all sites of the lattice ($J < 0$ corresponds to antiferromagnetic coupling). The partition function and the single site magnetization of the model are given by

$$\mathcal{Z} = \sum_{\{\sigma\}} e^{-\frac{\mathcal{H}}{k_B T}}, \tag{2.2}$$

$$M = \langle \delta(\sigma_0, Q) \rangle = \mathcal{Z}^{-1} \sum_{\{\sigma\}} \delta(\sigma_0, Q) e^{-\frac{\mathcal{H}}{k_B T}}, \tag{2.3}$$

where k_B is the Boltzmann constant (we will set $k_B = 1$). The Bethe lattice can be separated into γ identical branches by cutting it apart at the central point, resulting in the following expression for the partition function

$$\mathcal{Z}_n = \sum_{\{\sigma_0\}} exp\{\frac{H}{T} \cdot \delta(\sigma_0, Q)\}[g_n(\sigma_0)]^{\gamma}, \tag{2.4}$$

where σ_0 is the central spin and $g_n(\sigma_0)$ is the contribution of each lattice branch. Following the well-known procedure [78, 237–239], one finds the mapping

$$\begin{gathered} x_n = f(x_{n-1}), \\ f(x) = \frac{e^{\frac{H}{T}} + (e^{\frac{J}{T}} + Q - 2)x^{\gamma-1}}{e^{\frac{H+J}{T}} + (Q-1)x^{\gamma-1}}, \end{gathered} \tag{2.5}$$

which determines the thermodynamic properties of the model ($x_n = g_n(\sigma \neq Q)/g_n(\sigma = Q)$) and is known as the Potts-Bethe mapping. The magnetization of the central spin is thus defined as:

$$M_n = \langle \delta(\sigma_0, Q) \rangle = \frac{e^{\frac{H}{T}}}{e^{\frac{H}{T}} + (Q-1)x_n^{\gamma}}. \tag{2.6}$$

In real statistical systems the bifurcation points of mappings like (2.5) correspond to phase transition points with a change of a symmetry. For systems with $Q < 2$ with antiferromagnetic coupling ($J < 0$), the dependence of magnetization M on the field H is rather complicated: a full range of period doubling, chaos and p-cyclic windows is observed here. Figure 2.2 shows bifurcation diagrams for different values of parameters.

In terms of the mapping (2.5), the area where M is a single-valued function of H [AB and CD in Fig. 2.2(a), AB in Fig. 2.2(b)], the recursion sequence $\{x_n\}$ converges to one

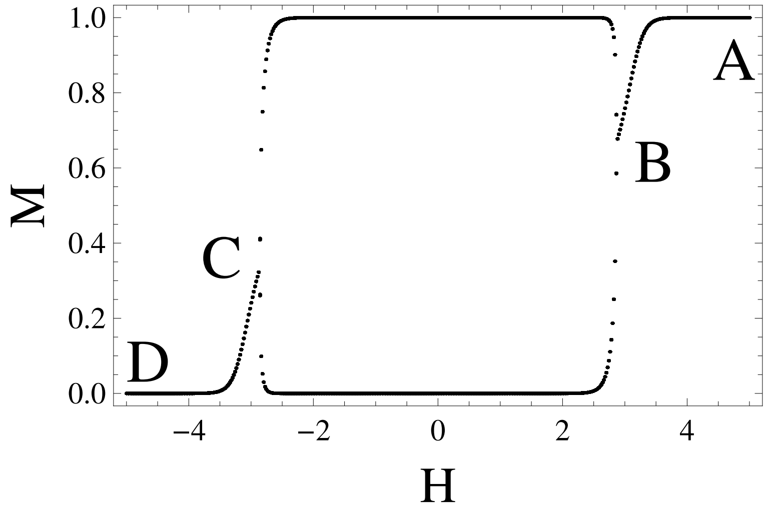

(a)

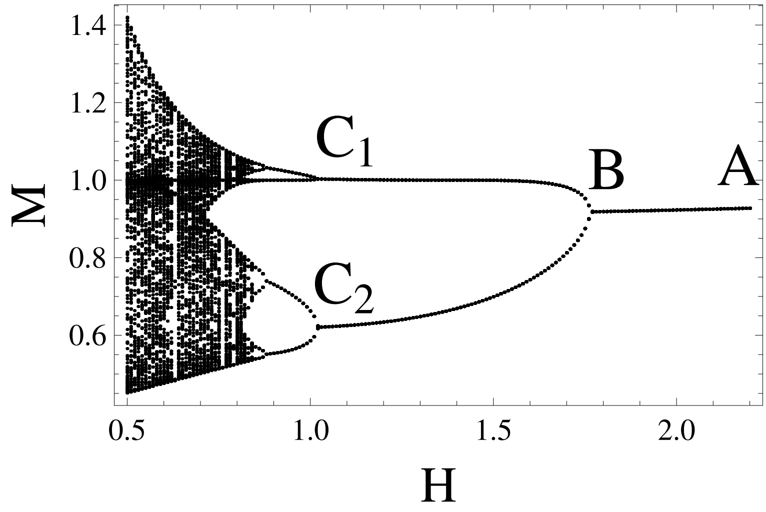

(b)

Figure 2.2: The magnetization M versus external magnetic field H for $\gamma = 3$, (a) $Q = 2$, $J = -1$, $T = 1$. The areas AB and CD correspond to the phase without sublattice structure (uniform phase), BC is the antiferromagnetic phase, B and C are the phase transition points; (b) $Q = 1.1$, $J = -1$, $T = 1$. Here AB correspond to the magnetization of the uniform phase, BC_1 and BC_2 are magnetizations of two sublattices of the antiferromagnetic phase.

stable fixed point x_0 (phase without sublattice structure). Meanwhile, in the region after the first bifurcation point [BC in Fig. 2.2(a), C_1BC_2 in Fig. 2.2(b)], the sequence $\{x_n\}$ has two stable points. Therefore here we have two values of magnetization, which can be explained, as an arising of two sublattices of an antiferromagnetic order. The areas between consequent bifurcation points are described by a sequence of n fixed points (n sublattices), corresponding to various modulated phases with finite period (commensurate modulated phases).

2.2.2 Universality of Feigenbaum exponents for the Potts model

In this subsection we address to the universality of Feigenbaum exponents for the Potts-Bethe mapping. Let r_n be the value of a parameter r of a mapping at a period doubling bifurcation point, and r_∞ the value of r from which the chaotic behavior ensues. It turns out that the values of r_n satisfy the following scaling:

$$r_n = r_\infty - const\delta^{-n}, \qquad n \gg 1. \tag{2.7}$$

If d_n is the distance between the point x^* for which $f_r(x)$ is extremal and the nearest point on a 2^n cycle (Fig. 2.3), than

$$\frac{d_n}{d_{n+1}} = -\alpha, \qquad n \gg 1. \tag{2.8}$$

The quantities α in Eq. (2.8) and δ in Eq. (2.7) are known as Feigenbaum exponents [234,235]:

$$\delta = 4,6692016091... \tag{2.9a}$$

$$\alpha = 2,50290787050... \tag{2.9b}$$

On the other hand, if R_n is the value of a parameter at which the line $x = x^*$ intersects 2^n periodic cycle (Fig. 2.3), one finds

$$R_n = R_\infty - const'\delta^{-n}. \tag{2.10}$$

An important observation is that the exponents δ and α are universal, i.e., Eqs. (2.7), (2.8) and (2.10) are true for a wide variety of mappings, with α and δ having the same values as in Eqs. (2.9a) and (2.9b) [234]. As for *const* and *const′* in Eqs. (2.7) and (2.10), they depend on the family of reflection functions.

For the numerical analysis of the above universality hypothesis for the Potts-Bethe mapping, we introduce a quantity δ_n, defined as

$$\delta_n = \frac{R_n - R_{n-1}}{R_{n+1} - R_n}. \tag{2.11}$$

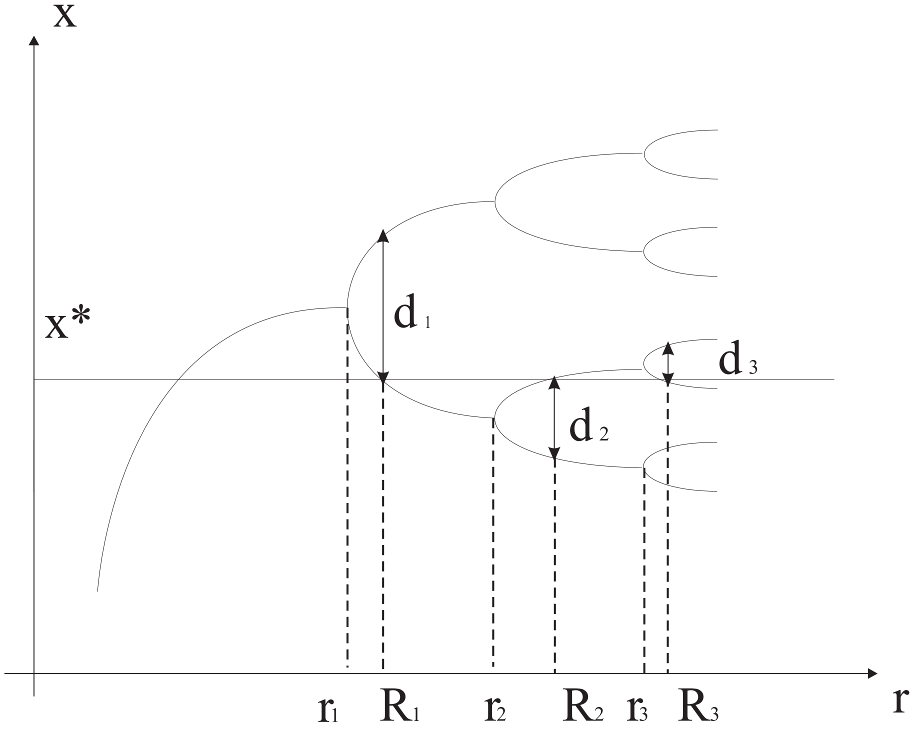

Figure 2.3: The period doubling process (schematically): r_n corresponds to a 2^n period-doubling bifurcation point, R_n is the value of a parameter at which the line $x = x^*$ intersects a 2^n periodic cycle.

Taking into account that [235]

$$\delta = \lim_{n\to\infty} \delta_n \tag{2.12}$$

and the condition

$$f_{R_n}^{(2^n)}(x^*) = x^* \tag{2.13}$$

($f^{(n)}(x)$ is the $n-th$ iteration of $f(x)$, i.e., $f^{(2)}(x) = f[f(x)]$, $f^{(2^2)}(x) = f^{(4)}(x) = f^{(2)}[f^{(2)}(x)]$, etc.), one calculates Feigenbaum exponents for a mapping $f(x)$. In our case

$$f(x) \ = \frac{e^{\frac{H}{T}}+(e^{\frac{J}{T}}+Q-2)x^{\gamma-1}}{e^{\frac{H}{T}}\cdot e^{\frac{J}{T}}+(Q-1)x^{\gamma-1}} = \frac{r+(e^{\frac{J}{T}}+Q-2)x^{\gamma-1}}{r\cdot e^{\frac{J}{T}}+(Q-1)x^{\gamma-1}}, \tag{2.14}$$

with

$$r = e^{\frac{H}{T}}. \tag{2.15}$$

The Potts-Bethe mapping $f(x)$ is extremal at $x^* = 0$.

Note that the values of R_n and r_n must satisfy the following condition (see Fig. 2.3):

$$r_1 < R_1 < r_2 < R_2 < r_3 < ... \tag{2.16}$$

Thus, we start solving Eq. (2.13) from $n = 0$, and put R_n's following the order (2.16). Additionally, one finds that

$$\lim_{n\to\infty} R_n = R_\infty = r_\infty. \tag{2.17}$$

Our numerical results for $J = -1$, $T = 1$, $\gamma = 3$, $Q = 1.1$ and $Q = 0.8$ are summarized in Table 2.1. We find that values of α and δ indeed converge to the Feigenbaum exponents for the Potts-Bethe mapping, which describes physical properties of a real statistical system. However, the convergence in the case $0 < Q < 1$ is faster than for $1 < Q < 2$. Below we find other confirmations of the fact that in the regimes $0 < Q < 1$ and $1 < Q < 2$ the model exhibits qualitatively different behavior.

As for $const'$, presented in Eq. (2.10), we obtained the following values for $Q = 0.8$ and $Q = 1.1$: $const' = -2.682...$ and $const' = -5.034...$ respectively. We emphasize again that the confirmed universality can be used in the approximate analysis of the phase structure of statistical models. Moreover, the speed of the convergence plays an essential role in determining the strength of the approximation [163].

2.2.3 Lyapunov exponents for one dimensional rational mapping

As generally known, under the action of a mapping $x_{n+1} = f(x_n)$ two nearby points can disperse. The Lyapunov exponent $\lambda(x)$ characterizes the degree of the exponential divergence of two adjacent points. Its exact formula is:

$$\lambda(x) = \lim_{n\to\infty} \lim_{\varepsilon\to 0} \frac{1}{n} \ln \left| \tfrac{f^{(n)}(x+\varepsilon)-f^{(n)}(x)}{\varepsilon} \right| = \lim\nolimits_{n\to\infty} \tfrac{1}{n} \ln \left| \tfrac{df^{(n)}(x)}{dx} \right|. \tag{2.18}$$

We consider the dependence of $\lambda(x)$ for the Potts-Bethe mapping on the external magnetic field H, fixing Q, temperature T and strength of interaction J [Fig. 2.4(a)].

One can also study the behavior of $\lambda(x)$ on the temperature T, fixing H, Q, and J [Fig. 2.4(b)]. This helps to examine the behavior of the magnetization at fixed external

Table 2.1: Feigenbaum exponents for Potts-Bethe mapping [Eq. (2.5)] for $T = 1$; $J = -1$; $\gamma = 3$.

Q	period doubling	R_n	α	δ_n
0.8	$2^1 = 2$	6.148585490...	-	-
	$2^2 = 4$	5.624678677...	3.068429829...	5.321086266...
	$2^3 = 8$	5.526220056...	2.580752880...	4.731522199...
	$2^4 = 16$	5.505410977...	2.519238533...	4.688360097...
	$2^5 = 32$	5.500972521...	2.506269470...	4.672585925...
	$2^6 = 64$	5.500022629...	2.503627065...	4.670011847...
	$2^7 = 128$	5.499819226...	2.503059457...	4.669364508...
	$2^8 = 256$	5.499775665...	2.502940259...	4.669237820...
	......	......	......	......
	$2^\infty = \infty$	5.499764337...	-	-
1.1	$2^1 = 2$	3.931868660...	-	-
	$2^2 = 4$	2.569022501...	3.358835598...	6.792470680...
	$2^3 = 8$	2.368381788...	2.654374001...	5.057633178...
	$2^4 = 16$	2.328710918...	2.534475897...	4.745030314...
	$2^5 = 32$	2.320350408...	2.509653084...	4.685552342...
	$2^6 = 64$	2.318566091...	2.504352497...	4.672658688...
	$2^7 = 128$	2.318184228...	2.503218367...	4.669946004...
	$2^8 = 256$	2.318102458...	2.502974448...	4.669360473...
	$2^9 = 512$	2.318084946...	2.502922160...	4.669235722...
	......	......	......	......
	$2^\infty = \infty$	2.318080392...	-	-

magnetic field, when temperature is varied (see also Sec. 2.2.4). Comparing Figs. 2.4(a) and (b) we find, that at a fixed H the chaotic region is richer than at a fixed T: a large variety of different p-cyclic windows can be observed in the first case.

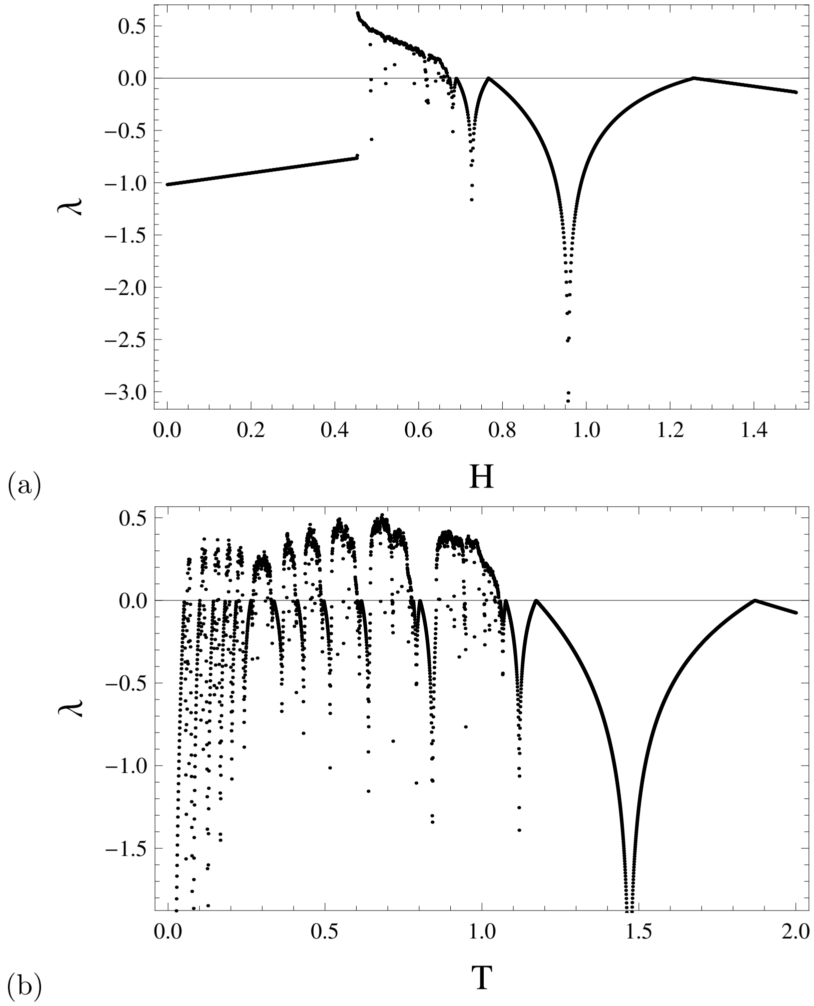

Figure 2.4: The Lyapunov exponent $\lambda(x)$ of the Potts-Bethe mapping (a) versus magnetic field H for $Q = 0.8$, $J = -1$, $\gamma = 3$, $T = 2$; (b) versus temperature T for $Q = 1.2$, $J = -1$, $\gamma = 3$, $H = 0.2$.

One of the major properties of the Lyapunov exponent is that it is equal to zero at a bifurcation point. This property can be easily deduced from the fact that a bifurcation point corresponds to a neutral point of a mapping. On the other hand the property is useful for detecting phase transition points between different modulated phases or between chaotic and periodic regimes.

2.2.4 Modulated phase structure

Here we turn to the study of the phase structure of the QSP model on a Bethe lattice by means of detecting bifurcation points of the mapping (2.5). Values of parameters (external magnetic field and temperature) at a phase transition (bifurcation) point can be found as a neutral point of a mapping:

$$f'(x) = e^{i\varphi}. \tag{2.19}$$

Different values of φ correspond to different types of bifurcation:

1. $\varphi = 2\pi n$. This case corresponds to a saddle-node or tangent bifurcation (type I intermittency) [225, 226]. It can be observed e.g. in the logistic map as transition to a p-cyclic window from a chaotic regime (see also Sec. 2.2.5).
2. $\varphi = \pi + 2\pi n$. Here we have a bifurcation corresponding to period doubling [240] (type III intermittency).
3. A pair of conjugate complex eigenvalues of the Jacobian in the case of a multidimensional mapping corresponds to the Hopf-bifurcation (type II intermittency) which introduces new basic frequencies in the system [241].

At the first bifurcation point in the period doubling regime we have:

$$\begin{cases} f(x) = x \\ f'(x) = -1. \end{cases} \tag{2.20}$$

Eliminating x from (2.20) and solving the obtained equation with respect to H, we obtain two branches:

$$\begin{aligned} H = T \cdot \ln \Bigg[\frac{1}{8(-1+Q)} e^{-\frac{3J}{T}} \Big(& -6e^{\frac{3J}{T}}(Q-2) - e^{J/T}(6Q+u-6)(Q-2) \\ & - 3e^{\frac{4J}{T}} + (Q-1)(Q+u-1) - e^{\frac{2J}{T}}(3(Q-2)Q+u+6\Big)\Bigg] \end{aligned} \tag{2.21}$$

and

$$\begin{aligned} H = T \cdot \ln \Bigg[\frac{1}{8(-1+Q)} e^{-\frac{3J}{T}} \Big(& -6e^{\frac{3J}{T}}(Q-2) - e^{J/T}(6Q-u-6)(Q-2) \\ & - 3e^{\frac{4J}{T}} + (Q-1)(Q-u-1) + e^{\frac{2J}{T}}(-3(Q-2)Q+u-6\Big)\Bigg], \end{aligned} \tag{2.22}$$

where

$$u = \sqrt{-1+e^{J/T}}\sqrt{Q+e^{J/T}-1}\sqrt{9e^{J/T}Q-Q-18e^{J/T}+9e^{2J/T}+1}. \tag{2.23}$$

Consider two regimes:

1. $Q > 1$. In this particular case two branches in (2.21) and (2.22) define the line separating the phase without sublattice structure (**U**, i.e. uniform) and the **2AF1** phase (this notation means AntiFerromagnetic phase of the period 2^1).

2. $Q < 1$. This case is more complicated because of the following reason (here and further $\gamma = 3$): when $Q < 1$, the Potts-Bethe mapping has singular points. Figure 2.5 indicates, that the behavior of the mapping becomes sensible to initial point of the iteration: a stable point can fall into the area I or II. But it turns out, that only the area I has a physical meaning: in the case $Q < 1$, magnetization can be negative, which has not physical interpretation [see Eq. (2.3)]. One can easily show that M is negative in the area II. Thus, hereafter we assume, that stable points of the mapping are in the area I. This corresponds to Eq. (2.22).

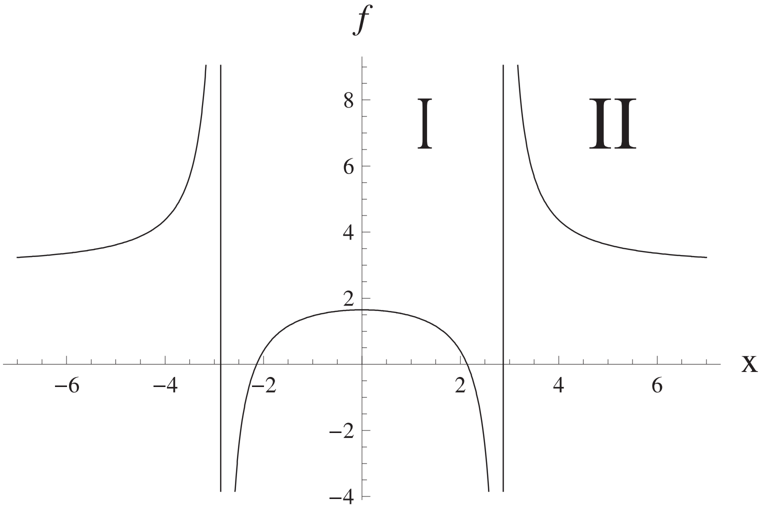

Figure 2.5: The Potts-Bethe mapping $f(x)$ for $Q = 0.8$, $J = -1$, $\gamma = 3$, $T = 2$, $H = 2$.

It is also of interest to find the line separating antiferromagnetic (**2AF1**) and four-periodic **2M2** phases (here and further the notation **mMn** means a magnetic phase of the period m^n) modulated phases. This means to find the values of T and H, where the second bifurcation occurs. The procedure is the same with the only difference being that here the second iteration of the mapping ($f^{(2)}(x) = f[f(x)]$) loses its stability:

$$\begin{cases} f^{(2)}(x) = x \\ (f^{(2)}(x))' = -1. \end{cases} \tag{2.24}$$

The area between two curves, obtained from Eqs. (2.20) and (2.24), is the one, where the two periodic modulated (antiferromagnetic) phase exists. Using the same technique we can also find the line, separating four-periodic (**2M2**) and eight-periodic (**2M3**, i.e., $2^3 = 8$-periodic) modulated phases. The condition reads:

$$\begin{cases} f^{(4)}(x) = x \\ (f^{(4)}(x))' = -1. \end{cases} \tag{2.25}$$

The area between curves defined by Eqs. (2.24) and (2.25) is the the area of the existence the four-periodic modulated phase. The results are given in Figs. 2.6 and 2.7.

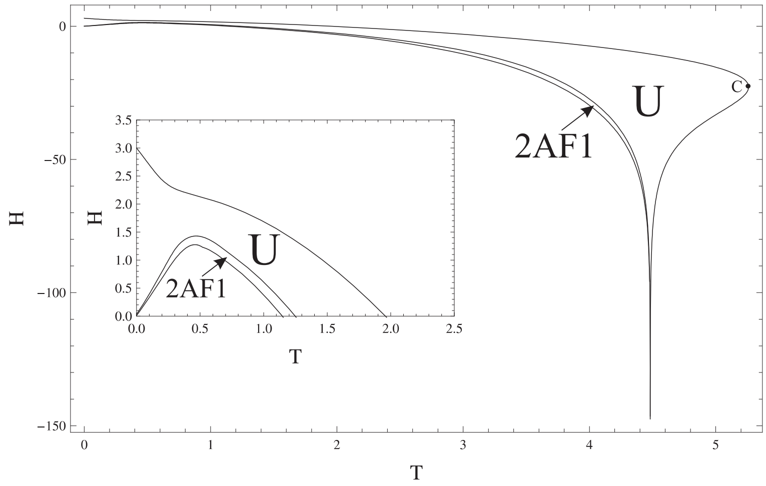

Figure 2.6: The phase diagram of the Q-state Potts model for $Q = 1.2$, $J = -1$, $\gamma = 3$: the uniform **U** phase without sublattice structure and the antiferromagnetic phase **2AF1** (the insert shows details in the area $H > 0$). Point C describes the upper bound of the temperature ($T_c = 5.260340$).

As mentioned in Sec. 2.2.1 the convergence rate of Feigenbaum exponents in areas $0 < Q < 1$ and $1 < Q < 2$ is different. As one can see from Figs. 2.6 and 2.7, the phase structure is different as well. In other words, the point $Q_c = 1$ can be considered as a critical one, corresponding to a transition between two regimes with qualitatively different thermodynamic behavior.

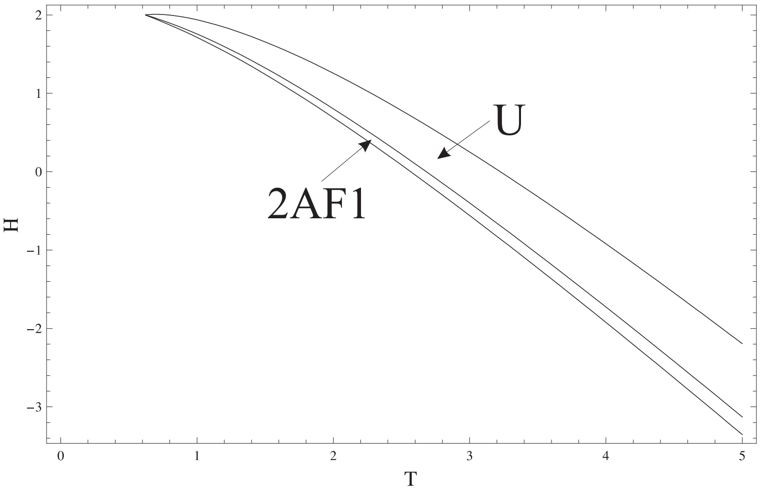

Figure 2.7: The same as in Fig. 2.6, but for $Q = 0.8$, $J = -1$, $\gamma = 3$.

The magnetization M can be also regarded as a function of T, fixing the value of external magnetic field. Figure 2.6 indicates, that upon lowering H, first two periodic cycles appear, corresponding to **U-2AF1** transition. When the line H intersects the curve of the uniform − antiferromagnetic phase transition line, one finds a bubble on each branch [Fig. 2.8(a)]. Here we have **U-2AF1-2M2-2AF1** transitions. After the line H intersects the lower curve, we have another two bubbles which points on the **U-2AF1-2M2-2M3-2M2-2AF1** transitions. Upon further decrease of the external magnetic field new bubbles are formed as parts of the old ones and for still lower H's we reach a chaotic region [Fig. 2.8(b)].

2.2.5 The three-periodic window

In this subsection we study the three-periodic window of the Potts-Bethe mapping. Some definite values of parameters T and H form a line in the parameter space, which separates the chaotic and the three-periodic regimes. Figure 2.9 presents the third iteration of the mapping $f(x)$ [Eq. (2.5)] for one point of that line (as one can see the mapping has three stable fixed points here). On this line the saddle-node bifurcation occurs, i.e. the aforementioned line is found from the following condition (see Sec. 2.2.4):

$$\begin{cases} f^{(3)}(x) = x \\ (f^{(3)}(x))' = 1. \end{cases} \tag{2.26}$$

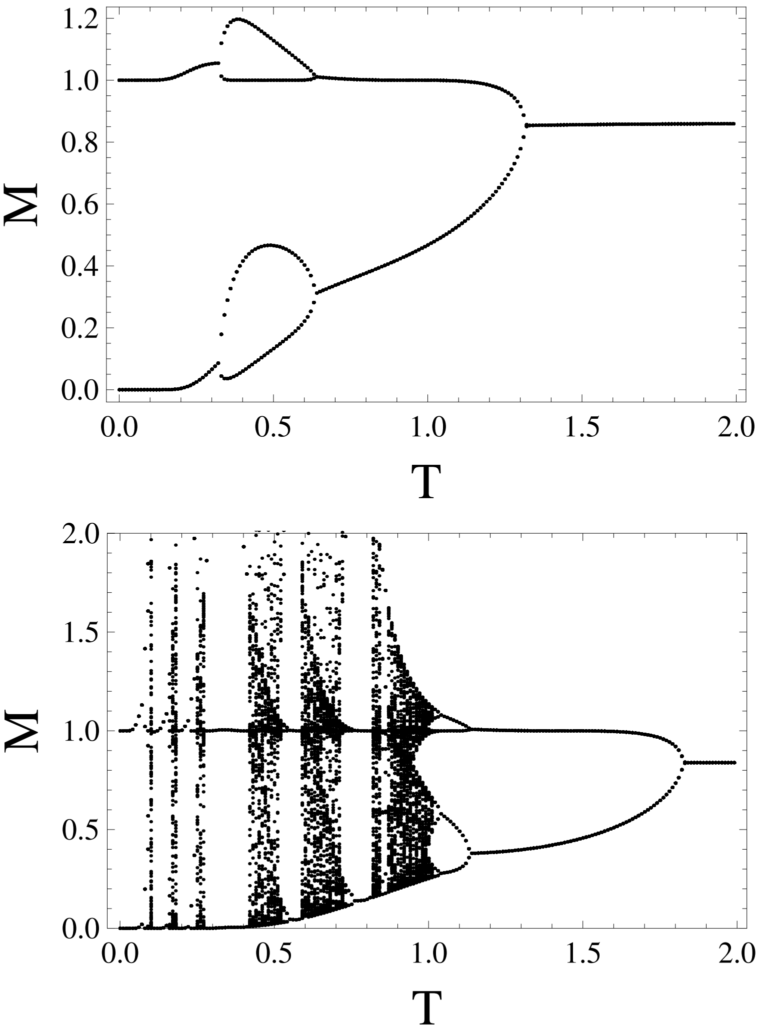

(a)

(b)

Figure 2.8: The magnetization M versus temperature T for $Q = 1.2$, $J = -1$, $\gamma = 3$ (a) $H = 1.25$; (b) $H = 0.3$.

Consequent bifurcations correspond to period doubling, which leads to appearance of stable 3×2^n periodic cycles. Following the technique described in Sec. 2.2.4, we find the line separating three- and six-periodic cycles (three- and six- periodic modulated phases) from the following system of equations:

$$\begin{cases} f^{(3)}(x) = x \\ (f^{(3)}(x))' = -1. \end{cases} \tag{2.27}$$

Curves found from (2.26) and (2.27) form the area of existence of the three-periodic modulated phase (**3M0**, i.e. $3 \times 2^0 = 3$ periodic) (Fig. 2.10).

One deduces from Fig. 2.10 that for $H > 0$ the mapping exhibits an interesting behavior.

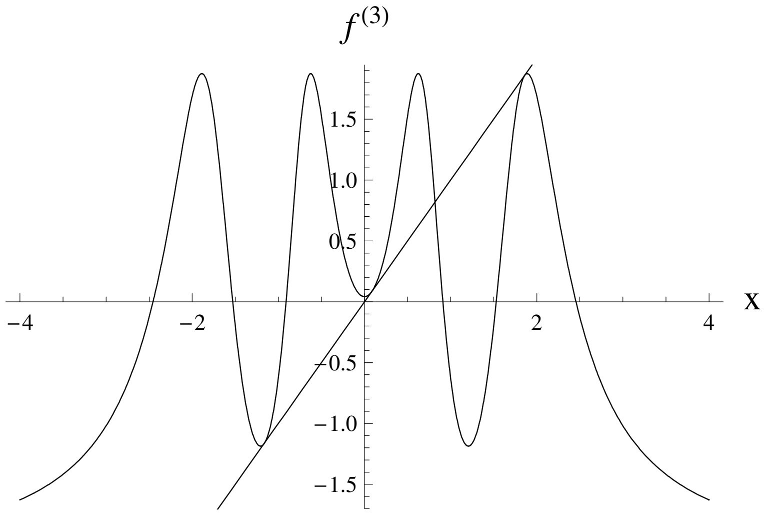

Figure 2.9: The third iteration of the Potts-Bethe mapping $f^{(3)}(x)$ for $Q = 1.1$, $J = -1$, $\gamma = 3$ at one point of the saddle-node bifurcation line defined by Eq. (2.26): $T = 1.5915$, $H = -1$.

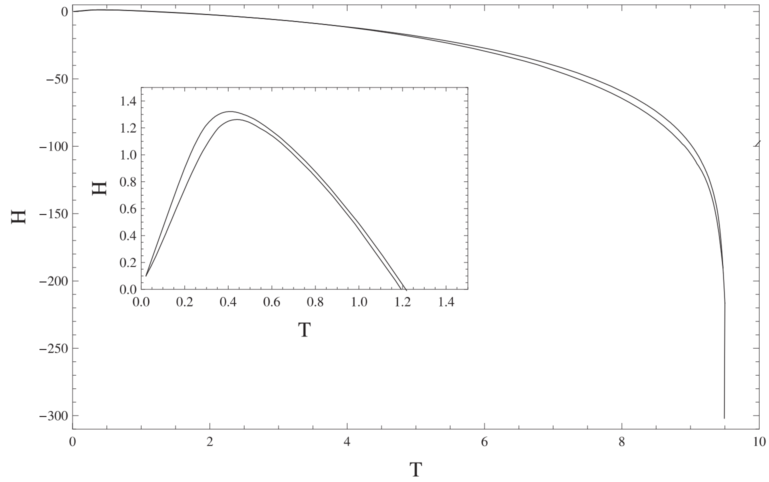

Figure 2.10: The three-periodic modulated phase **3M0** for the Potts model for $Q = 1.1$, $J = -1$, $\gamma = 3$ (the insert shows details in the area $H > 0$).

Firstly, when the line H intersects only the upper transition line, two edges of the window are plainly distinguishable: the saddle-node bifurcation takes place on both of them and the window is presented within the three-periodic cycle only [Fig. 2.11(a)]. Here transitions between chaotic state and the three-periodic modulated phase (**3M0**) occurs. Secondly when the line H intersects the lower transition line, a $3 \times 2^1 = 6$-periodic cycle appears in a form of a bubble, which corresponds to the six-periodic modulated phase (**3M1**, i.e. $3 \times 2^1 = 6$-periodic). This indicates the **3M0-3M1** transition. Obviously if we continue lowering the values of H, new bubbles appear and ultimately the chaotic region *inside* the window will be reached [Fig. 2.11(b)]. However, for $H < 0$ the saddle-node bifurcation occurs only at one edge of the window.

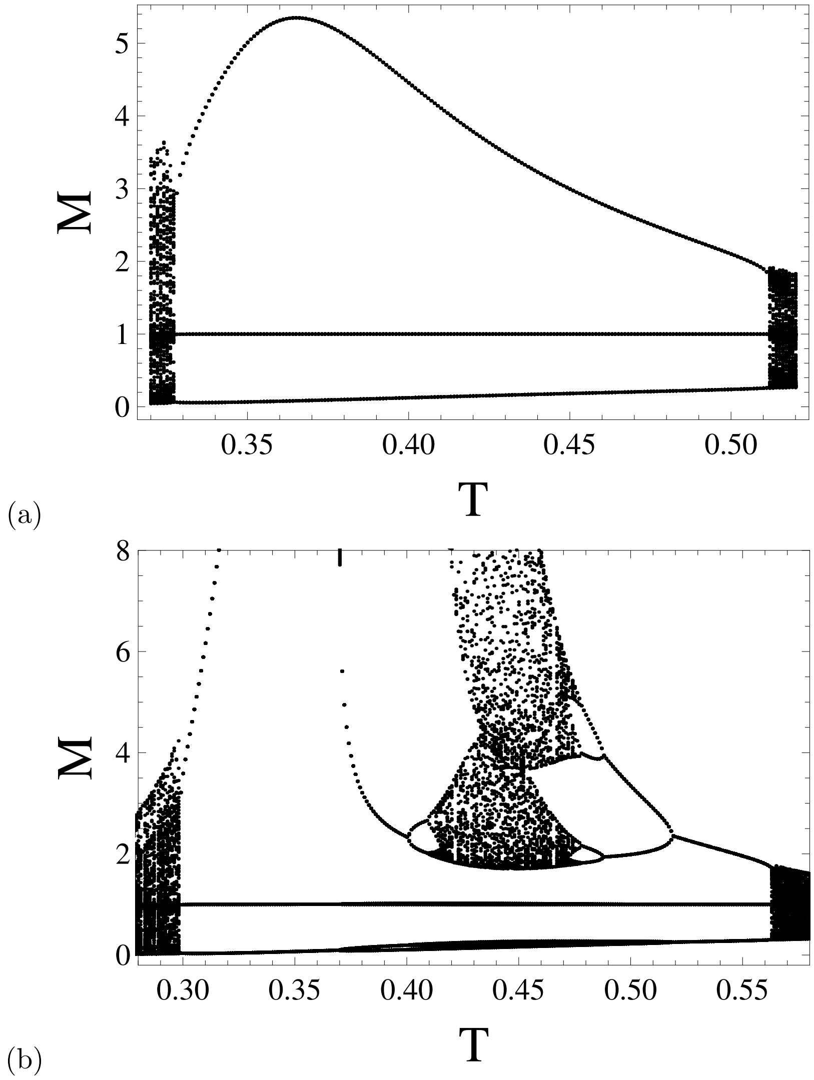

Figure 2.11: The magnetization M versus temperature T in the three-periodic window for $Q = 1.1$, $J = -1$, $\gamma = 3$ (a) $H = 1.27$; (b) $H = 1.22$.

We additionally turn to the behavior of the Feigenbaum α and δ exponents for the three-periodic window. In contrast to the conventional period doubling, the values of R_n here are found from the following condition:

$$f_{R_n}^{(3\cdot 2^n)}(x^*) = x^*. \tag{2.28}$$

The exponents α and δ converge to the values in Eqs. (2.9a) and (2.9b) for the three-periodic window as well. For instance, for $J = -1$, $T = 1$, $\gamma = 3$ and $Q = 0.8$ at $n = 10$, $\delta = 4.669160924$ and $\alpha = 2.502899839$. While for the *const′* in Eq. (2.10) for the same values of parameters we have: *const′* $= -0.0167...$ These results confirm once more the universality hypothesis for the rational mapping, which describes the Q-state Potts model on a Bethe lattice.

2.3 The three-site interaction antiferromagnetic Ising model on a Husimi lattice

2.3.1 The model and its exact solution

The three-site interaction antiferromagnetic Ising (TSAI) model on a Husimi lattice [Fig. 2.1(b)] is defined by the following Hamiltonian [238]:

$$\mathcal{H} = -J_3 \sum_{\triangle} \sigma_i \sigma_j \sigma_k - H \sum_i \sigma_i, \tag{2.29}$$

where $\sigma_i = \pm 1$ is the spin variable. The second term in the Hamiltonian incorporates the effects of the external magnetic field. The first sum in (2.29) runs over the triangles of the lattice, while the second one goes over all sites of the lattice ($J_3 < 0$ corresponds to the antiferromagnetic case).

The partition function and the single site magnetization of the model are given by

$$\mathcal{Z} = \sum_{\{\sigma\}} e^{-\frac{\mathcal{H}}{T}}; \tag{2.30}$$

$$M = \langle \sigma_0 \rangle = \mathcal{Z}^{-1} \sum_{\{\sigma\}} \sigma_0 e^{-\frac{\mathcal{H}}{T}}.$$

Following the recursion relation technique we separate the Husimi lattice into γ identical branches by cutting it apart at the central triangle. Afterwards, following the well-known procedure [78–80, 83–87, 163, 164], we obtain:

$$M = \langle \sigma_0 \rangle = \frac{e^{\frac{2H}{T}} y_n^{\gamma} - 1}{e^{\frac{2H}{T}} y_n^{\gamma} + 1}, \tag{2.31}$$

where

$$x_n = f_1(x_{n-1}), \qquad (2.32)$$
$$f(x) = \frac{x^{2(\gamma-1)} e^{\frac{4H+2J_3}{T}} + 2e^{\frac{2H}{T}} x^{\gamma-1} + e^{\frac{2J_3}{T}}}{2x^{\gamma-1} e^{\frac{2H+2J_3}{T}} + e^{\frac{4H}{T}} x^{2(\gamma-1)} + 1}.$$

Here $x_n = g_n(\sigma_0 = +1)/g_n(\sigma_0 = -1)$, with g_n being the contribution from each of γ identical branches after cutting it apart at the central triangle. We fix the coordination number to $\gamma = 3$ and consider this map in the region $x > 0$. The mappings $f(x)$ is maximal at $x = x^* = e^{-H/T}$. Note that in contrast to the Q-state Potts model with $Q < 1$ discussed in the previous section, the first iteration of the mapping (2.32) does not possess singularities (Fig. 2.12). Thus the properties of the model are not sensitive to the choice of the initial point x_0 of the recursive sequence $\{x_n\}$.

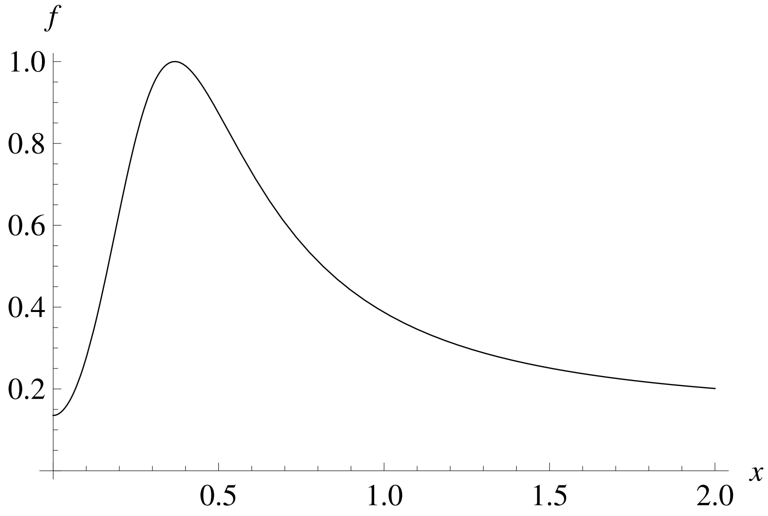

Figure 2.12: The mapping $f(x)$ from Eq. (2.32) for $H = 1$, $T = 1$, $J_3 = -1$ and $\gamma = 3$.

2.3.2 Phase structure and the three-periodic window

Since the phase structure of TSAI model in the conventional period doubling regime was analyzed in details in Refs. [224, 230–232, 238], in what follows we address to the properties of the model in the three-periodic regime. In other words, we plan to detect the transition from the chaotic (incommensurate modulated) phase to the three-periodic one. As already discussed in Sec. 2.2.5, this transition occurs through a tangent bifurcation (type I intermittency) [225, 226]. Thus we look for the solution of the following set of equations in the same way as in Sec. 2.2.5:

$$\begin{cases} f_i^{(3)}(x) = x \\ (f_i^{(3)}(x))' = 1, (i = 1, 2). \end{cases} \tag{2.33}$$

On the other hand, next bifurcation points correspond to a doubling of a period, leading to appearance of 3×2^n modulated phases and to transitions between them. In other words, next bifurcation point occurs within the following condition:

$$\begin{cases} f_i^{(3)}(x) = x \\ (f_i^{(3)}(x))' = -1, (i = 1, 2). \end{cases} \tag{2.34}$$

Solving the previous two sets of equations numerically, we obtain the chaotic − three-periodic modulated phase (Eq. 2.33) and the three-periodic − six-periodic modulated phase (Eq. 2.34) transition lines. Meanwhile, the region between the two above curves is the one where the three-periodic modulated phase (**3M0**, i.e. 3×2^0) exists.

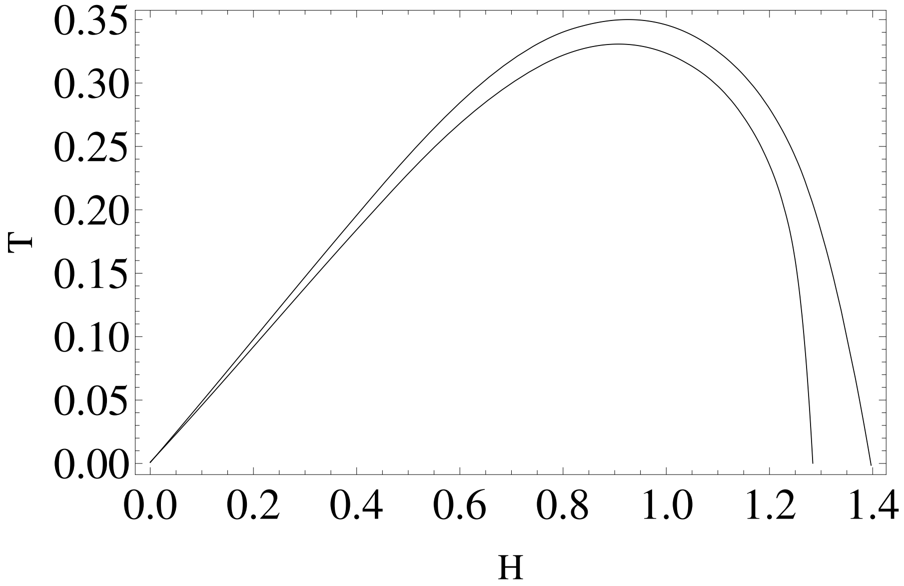

Figure 2.13: The three-periodic modulated phase of the three-site interaction antiferromagnetic Ising model for $J_3 = -1$ and $\gamma = 3$.

In Fig. 2.13 we show the **3M0** phase on the phase diagram (in the $(T; H)$ plane). Our first observation here is that the TSAI model possesses some common features compared to the Q-state Potts model. Firstly, we find that the mapping $f(x)$ (therefore, the magnetization M) undergoes a tangent bifurcation at both edges of the window, when the temperature is fixed ($T = const$) and the external field is varied. If the $T = const$ line intersects only the curve corresponding to Eq. (2.33), the window is represented by the **3M0** phase only [Fig. 2.14(a)]. Meanwhile, when the $T = const$ line intersects the curve corresponding to Eq. (2.34), the six-periodic phase **3M1** (i.e. $3 \times 2^1 = 6$) appears in a form of a new bubble, transition to which happens through a doubling bifurcation, i.e. through a phase transition with a change of a symmetry [Fig. 2.14(b)]. Upon further decrease in the temperature, chaos is reached, confined inside the window, as in the Potts model at $H = const$ [Fig. 2.14(c)]. Note that this picture of localization of 3×2^n phases inside a cyclic period-3 window for *one-dimensional rational mappings* given by Eqs. (2.5) and (2.32) describing statistical spin systems, was also observed in the three-dimensional polynomial Rossler system [242, 243].

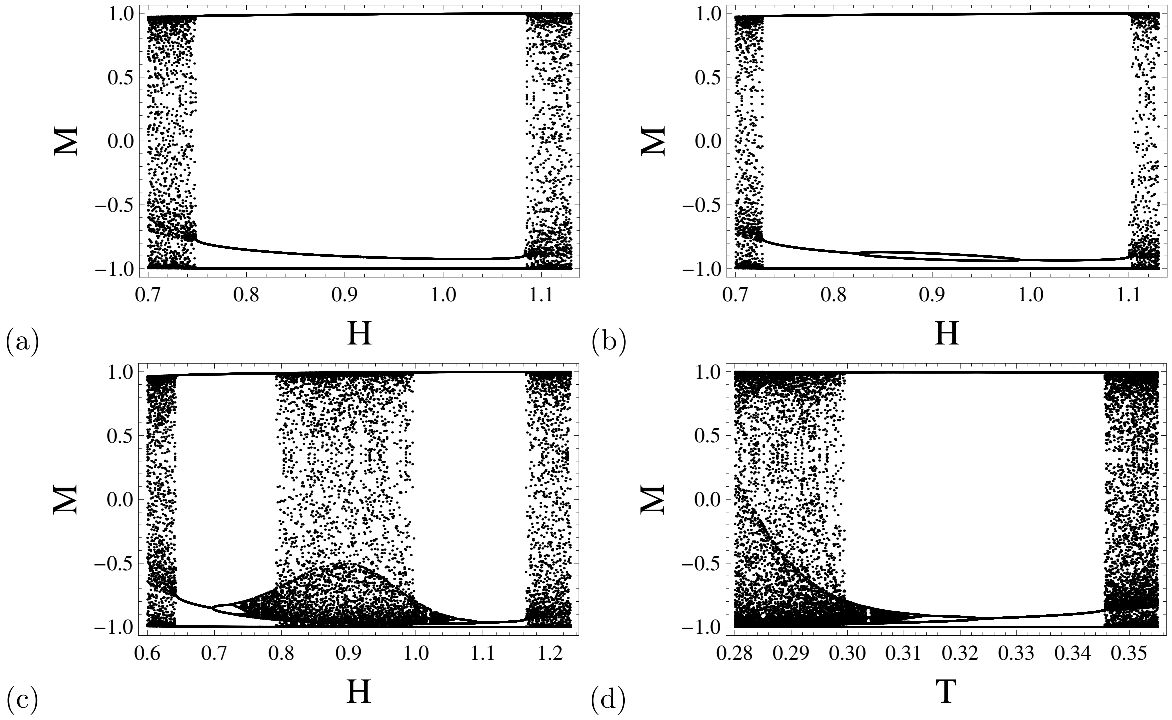

Figure 2.14: The magnetization M in the three-periodic window for $J_3 = -1$, $\gamma = 3$ (a) versus H for $T = 0.33$; (b) versus H for $T = 0.325$ (the bubbles corresponding to the six-periodic modulated phase are not seen on the upper and lower branches because of a small difference in sublattices' magnetizations); (c) versus H for $T = 0.3$; (d) versus T for $H = 1$.

Additionally, as is shown in Fig. 2.13, the transition between chaos and the **3M0** phase through a tangent bifurcation at a fixed field H occurs only at one edge of the window. Meanwhile, at the other edge, an abrupt change in the chaotic attractor occurs due to crisis [242, 244], i.e., the collision of the chaotic attractor with the independent unstable fixed point with a period of 3 (as in the Potts model at a fixed temperature T). Note there is a certain interval $H \in [1.276; 1.375]$, where the ground state of the TSAI model is the three-periodic modulated phase **3M0**.

Concluding the discussion of the phase structure of the three-periodic window, we consider the Lyapunov exponent $\lambda(x)$ [defined in Eq. (2.18)] as another order parameter. As already mentioned in Sec. 2.2.3, the Lyapunov exponent is negative in the periodic regime, positive in the chaotic one, and is zero at points of bifurcation. Figures 2.15(a) and (b) show the temperature dependencies of the Lyapunov exponents for the mapping $f(x)$ defined in Eq. (2.32) for the same parameters as in Figs. 2.14(b) and (c), respectively. According to Fig. 2.15, $\lambda(x) = -\infty$ at certain parameters T and H. These points correspond to the superstable cycles [245, 246], which are located in the region of a particular modulated phase. Therefore, the construction (both analytical and numerical) of the superstable cycle of the order n makes it possible to determine the regions of T and H where a modulated phase of a period n exists.

Considering the discussion of the previous two sections, we conclude, that the bifurcation properties in the cyclic three-periodic window of the antiferromagnetic Potts model on a Bethe lattice with respect to the temperature T at magnetic fields $H > 0$ are similar to the respective properties of the three-site interaction antiferromagnetic Ising model on a Husimi lattice with respect to the magnetic field H (compare Figs. 2.10 and inset in Fig. 2.13).

An intriguing note is that the intermittency phenomenon (leading to transitions from chaotic to periodic phases and vice versa), discussed in the present chapter, can also be used for the construction of so-called Ulam networks, which share certain common features with real social ones [247]. Moreover, methods of spin dynamics within the models described above, can be used, particularly, for the analysis of some opinion formation processes. We have addressed this question in Ref. [165].

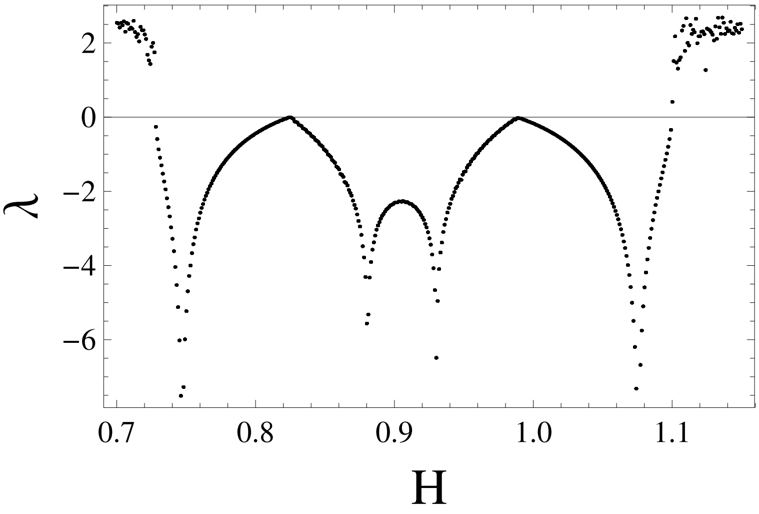

(a)

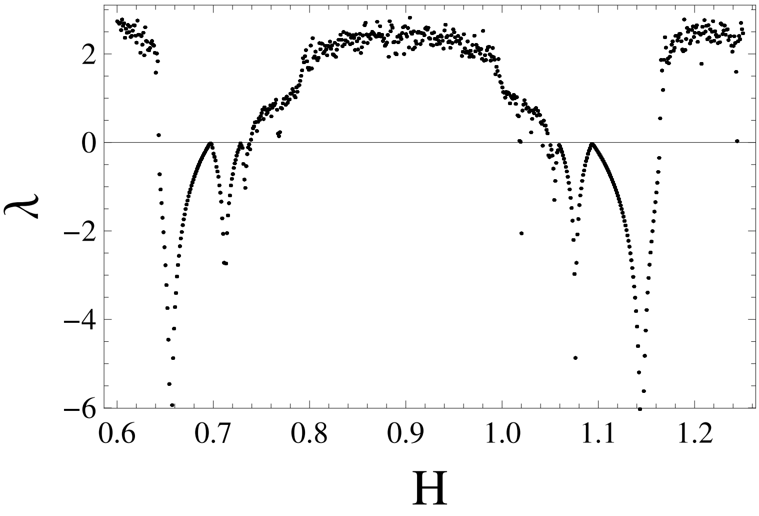

(b)

Figure 2.15: The magnetic field dependence of the Lyapunov exponent $\lambda(x)$ in the three-periodic window for $J_3 = -1$, $\gamma = 3$ and (a) $T = 0.325$ (b) $T = 0.3$.

2.4 Summary

1. The thermodynamic properties of the Q-state Potts model on a Bethe lattice and the three-site interaction antiferromagnetic Ising model on a Husimi lattice are analyzed by means of the recurrence relation technique.

2. For the rational mapping of the Q-state Potts model we proved the universality of Feigenbaum exponents and studied their convergence rate (which can be useful for approximate construction of phase transition lines between different modulated phases). Furthermore, we revealed two regimes $0 < Q < 1$ and $1 < Q < 2$ with qualitatively distinct thermodynamic behavior.

3. The phase structure of both models is analyzed through detecting the bifurcation points

of corresponding one dimensional rational mappings. Particularly, for the Potts model we analyzed the conventional period doubling sequence and revealed a number of modulated phases and phase transitions between them.

4. Additionally, we analyzed the three-periodic window for both models, appearing in the chaotic regime through a tangent bifurcation. The window exhibits some peculiar features, as plainly distinguishable edges, presence of a finite number of 3×2^n cycles and confinement of chaos inside the window.
5. Finally, we pointed out some common bifurcation (and thus thermodynamic) properties of the Potts model with respect to the temperature T (for $H > 0$) on the one hand and the Ising model with respect to the magnetic field H on the other.

Chapter 3

SYSTEMS OF INTERACTING ATOMS AND FIELDS [1]

3.1 Introduction

As already discussed in previous chapters, quantum information processing can be implemented in alternative platforms to solids, such as an atomic system interacting with quantized fields. Particularly, the Dicke model (DM) features the interaction of a single-mode bosonic field with a collection of two-level atoms [115,116]. The DM is usually considered in the rotating-wave approximation, when the atom-field coupling strength is relatively weak. In the present chapter we are mainly interested in an important special case of the DM, corresponding to the so-called dispersive limit [122–124], which is also widely used for quantum information processing [125–128]. In this case the radiation field mediates an effective coupling of a dipole-dipole nature between the atoms in a cavity.

In the next section we investigate the entanglement features of three atoms coupled by a dipole-dipole interaction (in a sense described above), and use the concurrence as a measure of pairwise entanglement. As already mentioned in the Introduction of the present thesis, the DM in the dispersive limit is strongly related to the problem of frustrated magnetism, discussed in the previous two chapters. As it will be shown in the following section, the effective coupling constant becomes dependent on the detuning between the atomic transition

---

[1] The results considered in this chapter are published in Refs. [167–169].

frequency and the cavity field. This provides a relatively simple way of manipulating the interaction strength magnitude, what is rather complicated in the case of solids. Besides, a change of the sign of the interaction strength (corresponding to a switch between regimes with distinct physical pictures) also becomes possible by appropriate modifications of the setup parameters. Furthermore, the effective Hamiltonian gives rise to so-called collective spin models: many-body systems possessing long- or even infinite-range interactions [248–251]. Since in our case the dipole-dipole coupling is mediated by a radiation field, the atoms can interact with each other on an arbitrary distance within the cavity volume. Thus, the idealized infinite interaction length becomes practicable. We also take into account the vacuum induced Stark shift term, which causes qualitative changes in the ground state of the system. It results in a physical picture, different from the one corresponding to a pure Heisenberg-type exchange interaction.

Numerous problems of atomic optics and quantum information require atoms and molecules prepared in specified quantum states. Furthermore with the growing interest in quantum information, there is also concern with creating and controlling specified coherent superpositions of quantum states. Therefore there has long been interest in finding techniques to control the transfer of population between quantum states. A particularly interesting technique for population transfer is the stimulated Raman adiabatic passage (STIRAP) [135,252] realized via so-called "dark" (or "trapped") states [253]. In this chapter we focus our attention on the alternative method involving rather "bright" [254, 255] than "dark" state. Unlike STIRAP, which is insensitive to the radiative losses from the excited state that is not populated, b-STIRAP stores some transient population in the excited state. Radiative losses are therefore possible resulting in a reduction in the transfer efficiency. Thus contrary to STIRAP, b-STIRAP should feature a sufficiently large one-photon detuning and sufficiently short interaction time in order to permit efficient population transfer. The growing interest for b-STIRAP necessitates a further investigation when the propagation effects are taken into account. The essential difference of the b-STIRAP method, as compared to STIRAP, is that the first one is a faster process that is realized with a superluminal velocity. Another difference is that the adiabaticity conditions are stronger in the case of b-STIRAP. For instance, when the oscillator strengths of both transitions are equal, the interaction adibaticity, provided at the medium entrance, is broken down for b-STIRAP, while for STIRAP it is preserved during propagation. In this context, the natural question arises whether the population transfer efficiency in a medium via b-STIRAP is also sensitive to the ratio of oscillator strengths.

To clarify the question addressed, we make a detailed theoretical study of nonlinear pulse propagation in a Λ-type three-level atomic system under the conditions of the "bright" state, for various ratios of the medium coupling constants. Our results show that the population transfer dynamics strongly depends, in particular, on this ratio. We find that, depending on the ratio, pulses propagating in a medium will maintain their capacity to produce efficient adiabatic population transfer for long distances in some cases and loose this property in others.

3.2 The Dicke model in the dispersive limit

3.2.1 The model

We consider N two-level trapped atoms interacting with a single-mode cavity field. The Hamiltonian of the system (the DM model) in the rotating wave approximation can be written as (in units such that $\hbar = 1$)

$$\mathcal{H} = \mathcal{H}_0 + \mathcal{V}, \tag{3.1}$$

$$\mathcal{H}_0 = \omega_0 a^\dagger a + \frac{1}{2}\sum_{i=1}^{N} \omega_i S_i^z, \tag{3.2}$$

$$\mathcal{V} = g \sum_{i=1}^{N} (S_i^+ a + S_i^- a^\dagger), \tag{3.3}$$

where $S_i^+ = |1_i\rangle\langle 0_i|$, $S_i^- = |0_i\rangle\langle 1_i|$, $S_i^z = |1_i\rangle\langle 1_i| - |0_i\rangle\langle 0_i|$ (with $|0_i\rangle$ and $|1_i\rangle$ the ground and excited states respectively, of the $i-th$ atom), $a^\dagger$ and a are the creation and annihilation operators for the cavity mode, ω_i is the $i-th$ atomic transition frequency, ω_0 is the cavity frequency, and g is the atom-cavity coupling strength [115, 116].

We focus on the dispersive limit [122–127], when

$$|\omega_i - \omega_0| \gg g\sqrt{\bar{n}+1}, \qquad i = 1, ..., N \tag{3.4}$$

with $\bar{n}$ the mean number of photons. In the interaction representation the system is governed by an effective Hamiltonian [125–127]

$$\mathcal{V}_{\text{eff}} = \lambda\Big(\sum_{i=1}^{N} |1_i\rangle\langle 1_i| aa^\dagger - |0_i\rangle\langle 0_i| a^\dagger a + \sum_{i\neq j} S_i^+ S_j^-\Big), \tag{3.5}$$

where $\lambda = g^2/\delta$ is the effective coupling constant and $\delta = \omega_i - \omega_0$. In this case there is no photon exchange between the cavity field and the atomic system. The only allowed transitions are between the states with the same number of excited atoms and cavity field photons. The first and second terms in (3.5) describe the photon-number-dependent (dynamical) Stark shifts, while the third one can be interpreted as all possible flip operator of the atomic excitation through cavity induced dipole-dipole interaction between the $i-th$ and $j-th$ atom. Switching to the interaction representation with respect to the diagonal terms of $\mathcal{V}_{\text{eff}}$: $|\psi^{(\text{int})}_{\text{eff}}(t)\rangle = e^{-i\mathcal{V}_0 t}|\psi_{\text{eff}}(t)\rangle$, where

$$\mathcal{V}_0 = \lambda\Big(\sum_{i=1}^{N} |1_i\rangle\langle 1_i| aa^\dagger - |0_i\rangle\langle 0_i| a^\dagger a\Big), \tag{3.6}$$

one can describe the dynamics of the wave function by the reduced Hamiltonian [126, 127]

$$\mathcal{V}^{(\text{int})}_{\text{eff}} = \lambda \sum_{i\neq j} S_i^+ S_j^-. \tag{3.7}$$

However, if one intends to study the thermodynamic features of the DM in a dispersive limit, the complete Hamiltonian should be considered, i.e. we should switch back to the Schrödinger representation of (3.7), where the atomic and the field systems appear factorable:

$$\mathcal{H}_{\text{eff}} = \omega_0 a^\dagger a + \sum_{i=1}^{N}\Big(\frac{1}{2}\omega_i + \lambda a^\dagger a\Big) S_i^z + \lambda\Big(\sum_{i=1}^{N} |1_i\rangle\langle 1_i| + \sum_{i\neq j} S_i^+ S_j^-\Big). \tag{3.8}$$

An important feature of the final model is the tunability of the coupling constant. The latter can be in principle modified, e.g. by a change of the value of the detuning δ (in contrast with solid-state systems, where the coupling constant is more or less fixed). Note that the sign of the coupling constant can also be changed by a change of the sign of detuning. In magnetic systems this would correspond to a transition from a ferromagnetic regime ($\lambda < 0$) to an antiferromagnetic one ($\lambda > 0$). As it will be shown in the following subsections, different signs of λ correspond to different physical pictures. On the other hand one finds that the term $1/2\sum_{i=1}^{N}\omega_i S_i^z$ in (3.8), corresponding to the Hamiltonian of the free atomic system, is equivalent to the term of magnetic field effect in magnetic spin models [compare with Hamiltonians in Eqs. (1.1) and (1.13)].

In the present section we consider the state of the field to be a vacuum state $|vac\rangle$. Thus we can work with the following reduced Hamiltonian:

$$\mathcal{H}_{\text{eff}} = \lambda\left(\sum_{i=1}^{N}|1_i\rangle\langle 1_i| + \sum_{i\neq j} S_i^+ S_j^-\right) + \frac{1}{2}\sum_{i=1}^{N}\omega_i S_i^z. \tag{3.9}$$

We also emphasize that (3.9) is equivalent to a collective spin model [248–251]. Generally, this class of systems demands very special characteristics for experimental realization, since they feature in principle an infinite interaction range. However, quantum electrodynamical (QED) cavity allows a collective coupling between trapped atoms as photons are shared by all the atoms.

In this section we will consider identical atoms, i.e. atoms with equal transition frequencies: $\omega_i \equiv \omega$ for $i = 1, 2, ..., N$.

3.2.2 Entanglement of three coupled atoms

In this subsection we discuss the entanglement properties of three trapped atoms, coupled to each other by means of an effective dipole-dipole interaction (3.9) mediated by a cavity field.

The eigenvalues of $\mathcal{H}_{\text{eff}}$ are

$$\begin{aligned} &E_1 = -\frac{3\omega}{2}; \quad E_2 = E_3 = -\frac{\omega}{2}; \\ &E_4 = 3\lambda - \frac{\omega}{2}; \quad E_5 = E_6 = \lambda + \frac{\omega}{2}; \\ &E_7 = 4\lambda + \frac{\omega}{2}; \quad E_8 = \frac{3\omega}{2} + 3\lambda \end{aligned} \tag{3.10}$$

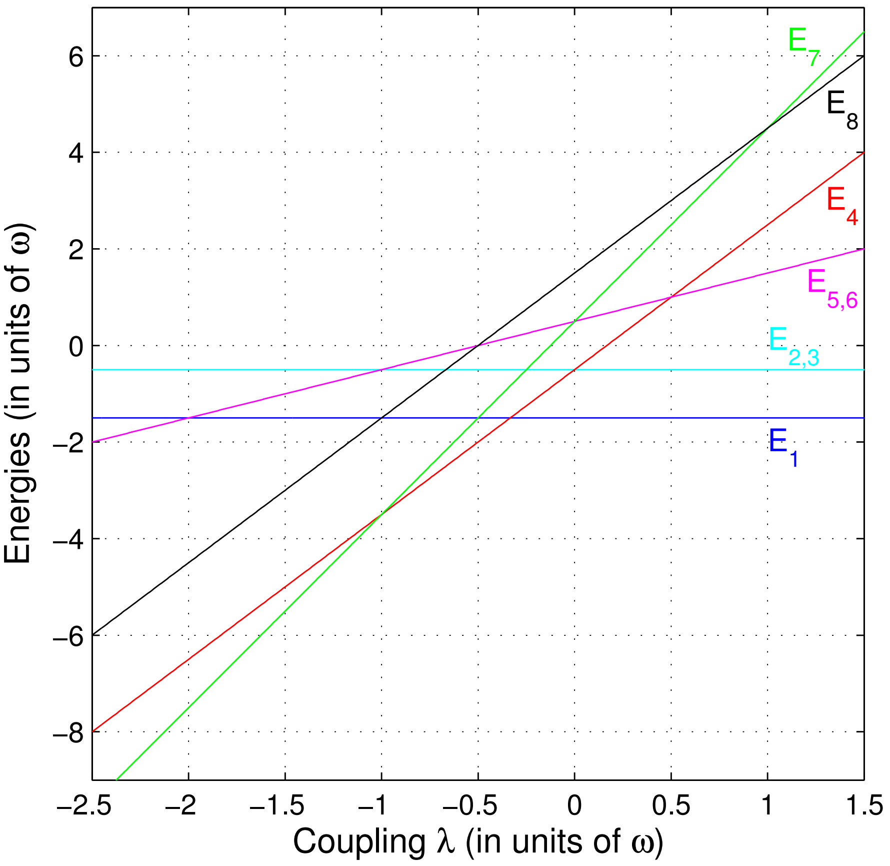

Figure 3.1: Eigenvalues as functions of λ.

with the corresponding eigenvectors given by

$$\begin{aligned}
|\psi_1\rangle &= |000\rangle \\
|\psi_2\rangle &= \frac{1}{\sqrt{3}}\left(q|001\rangle + q^2|010\rangle + |100\rangle\right) \\
|\psi_3\rangle &= \frac{1}{\sqrt{3}}\left(q^2|001\rangle + q|010\rangle + |100\rangle\right) \\
|\psi_4\rangle &= \frac{1}{\sqrt{3}}\left(|001\rangle + |010\rangle + |100\rangle\right) \\
|\psi_5\rangle &= \frac{1}{\sqrt{3}}\left(q|110\rangle + q^2|101\rangle + |011\rangle\right) \\
|\psi_6\rangle &= \frac{1}{\sqrt{3}}\left(q^2|110\rangle + q|101\rangle + |011\rangle\right) \\
|\psi_7\rangle &= \frac{1}{\sqrt{3}}\left(|110\rangle + |101\rangle + |011\rangle\right) \\
|\psi_8\rangle &= |111\rangle,
\end{aligned} \tag{3.11}$$

where $q = e^{i2\pi/3}$. The states of the whole system, including the dressing field, is of the form

$|\psi_i\rangle \otimes |vac\rangle$, $i = 1, ..., 8$. We have here omitted for simplification the vacuum state of the field. Note that the eigenstates of the present model have the same structure as the ones from Sec. 1.3.2 [Eq. (1.21)]. This is due to the fact that both systems possess similar symmetries. However, as shown below, the Stark shift term changes the physical picture drastically. As already mentioned in the previous subsection, $\mathcal{H}_{\text{eff}}$ couples only the states which have the same number of excited atoms. This is a consequence of the fact that the Hamiltonian (3.9) commutes with $\sum_{i=1}^{N} S_i^z$. In other words the total pseudospin of the system is a conserved quantity. This implies that state $|\psi_1\rangle$ (with no excited atoms) and state $|\psi_8\rangle$ (with all the atoms excited) are decoupled from each other and also from all the other states with one single atom excited and with two atoms excited, and while the states with one single atom excited and the ones with two atoms excited form two decoupled blocks. Transitions inside each of these two blocks are cavity mode driven Raman transitions.

The resulting eigenvalues (3.10) are plotted in Fig. 3.1 as functions of the coupling λ. They show a quite simple structure for positive values of λ, as only two crossings between excited states occur. On the other hand, negative values of λ imply crossing of excited states with the ground state. In particular, one notices the crossing of E_4 with E_1 for the relatively low value of the coupling $\lambda = \omega/3$. The vacuum induced Stark shift leads to a strong modification of the regimes. Therefore, we anticipate that the Stark shift terms play an important role in the formation of the ground state properties of a system, as it is confirmed below.

3.2.3 Entanglement and concurrence

We study concurrence $C(\rho)$, defined in Sec. 1.2.1, to quantify pairwise entanglement of the present model. Since we consider bipartite entanglement, we reduce the full density matrix ρ with respect to the rest of the system (i.e. the third atom) in the same way as was done in Chapter 1: $\rho_{12} = \text{Tr}_3\rho$. The overall density matrix ρ at a thermal equilibrium, which takes into account the thermal mixing of the eigenstates (3.11), has the form

$$\rho = \frac{1}{Z}\sum_{k=1}^{8} \exp(-E_k/T)|\psi_k\rangle\langle\psi_k|, \tag{3.12}$$

where

$$Z = e^{-\frac{8\lambda+3\omega}{2T}} \left[\left(2e^{\frac{3\lambda}{T}}+1\right) e^{\frac{\omega}{T}} + \left(2e^{\frac{3\lambda}{T}}+1\right) e^{\frac{\lambda+2\omega}{T}} + e^{\frac{4\lambda+3\omega}{T}} + e^{\frac{\lambda}{T}} \right] \tag{3.13}$$

is the partition function, E_k and $|\psi_k\rangle$ are taken from Eqs. (3.10) and (3.11) respectively.

Since in our case the system of three atoms [interacting via (3.9)] possesses a translational symmetry, the index number of the traced out atom can be chosen arbitrary. We skip the specific details here and provide the final result of the matrix ρ_{12}, taking also into account that the Hamiltonian $\mathcal{H}_{\text{eff}}$ satisfies $[S^z, \mathcal{H}_{\text{eff}}] = 0$ ($S^z = \sum_{i=1}^N S_i^z$):

$$\rho_{12} = \begin{pmatrix} u & 0 & 0 & 0 \\ 0 & w & y & 0 \\ 0 & y^* & w & 0 \\ 0 & 0 & 0 & v \end{pmatrix}, \tag{3.14}$$

where

$$\begin{aligned} u &= \frac{1}{3} e^{-\frac{8\lambda+3\omega}{2T}} \left(2e^{\frac{3\lambda+\omega}{T}} + 3e^{\frac{\lambda}{T}} + e^{\frac{\omega}{T}}\right) \\ v &= \frac{1}{3} e^{\frac{\omega-6\lambda}{2T}} \left(3e^{\frac{3\lambda+\omega}{T}} + 2e^{\frac{3\lambda}{T}} + 1\right) \\ w &= -\frac{1}{3} \left(e^{\frac{3\lambda}{T}} - 1\right) e^{-\frac{8\lambda+\omega}{2T}} \left(e^{\frac{\lambda+\omega}{T}} + 1\right) \\ y &= -\frac{1}{3} \left(e^{\frac{3\lambda}{T}} - 1\right) e^{-\frac{8\lambda+\omega}{2T}} \left(e^{\frac{\lambda+\omega}{T}} + 1\right). \end{aligned} \tag{3.15}$$

The concurrence $C(\rho)$ of such state has the following form (see Sec. 1.2.1):

$$C(\rho) = \frac{2}{Z} \max(|y| - \sqrt{uv}, 0). \tag{3.16}$$

Before investigating the ground state entanglement properties, we remark that all the states $|\psi_i\rangle$ with $i = 2, 3, ..., 7$ are entangled with an amount of 2/3 for any pair of atoms [hereafter the amount of *entanglement* refers to the defined above concurrence $C(\rho)$].

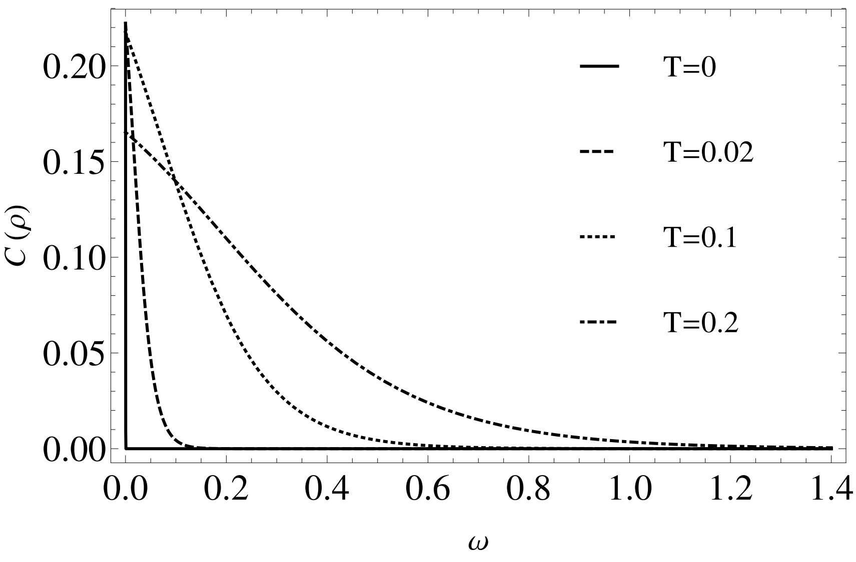

Figure 3.2: Concurrence $C(\rho)$ versus atomic transition frequency ω, for $\lambda = 1$ and different values of the temperature T.

3.2.4 Positive coupling

We first discuss the case of positive λ. Within the analogy of magnetic systems, for which the external magnetic field would correspond to ω and the interaction constant to λ, this regime can be considered as being antiferromagnetic. Figure 3.2 shows the concurrence $C(\rho)$ versus the atomic transition frequency ω for different values of temperature T. As one can see, at a zero temperature the system is not entangled. This is due to the fact that the ground state is the saturated $|\psi_1\rangle$ (with all atoms being non-excited). Solid state systems with antiferromagnetic coupling feature a frustrated ground state, persisting up to some critical value of ω, corresponding to a transition between frustrated and saturated phases. However this does not take place in this model for positive λ because of the vacuum induced Stark shift.

It is also of interest to discuss the case $\omega \to 0$. The ground state becomes three-fold degenerate in this limit, and it additionally contains $|\psi_2\rangle$ and $|\psi_3\rangle$ besides $|\psi_1\rangle$. The system is described by a mixture of these three states (i.e. by a density matrix) with a non-zero value of entanglement: $C(\rho) = 2/9$.

The appearance of a non-zero temperature will smooth the step-like behavior of $C(\rho)$. Since the temperature mixes all the eigenstates of the system, it can induce the so-called

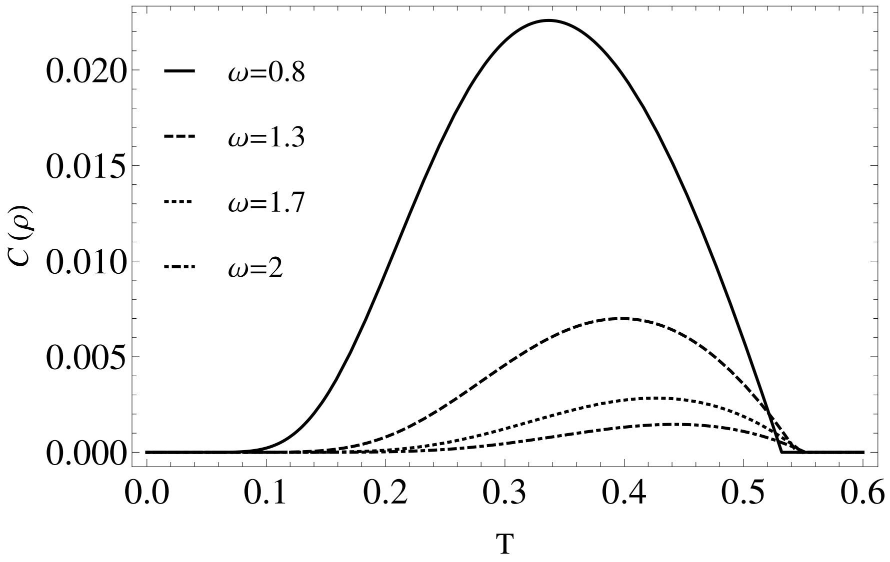

Figure 3.3: Dimensionless concurrence $C(\rho)$ versus temperature T (in units of λ), for different values of the atomic transition frequency ω (in units of λ).

thermal entanglement [19] despite a non-entangled ground state. Particularly, the thermal effects induce a larger amount of entanglement for ω closer to zero (see Fig. 3.2). Moreover, the dependency curve of $C(\rho)$ versus temperature exhibits a local maximum, corresponding to an optimal mixing of the system's eigenstates (Fig. 3.3). However, the quantum correlations between the atoms gradually disappear at some temperature T_d, referred in the literature to as sudden-death temperature and discussed in Sec. 1.2.2 (note that the thermal entanglement appears smoothly for low temperatures, i.e. concurrence becomes zero only at $T = 0$).

One can notice in Fig. 3.3 that the higher the atomic transition frequency ω is, the higher is the sudden-death temperature T_d. But it turns out that T_d remains finite with the growth of ω, i.e. there exists some saturation temperature T_s such that $T_d < T_s$, or $\lim_{\omega\to\infty} T_d = T_s$.

3.2.5 Negative coupling

Now we proceed to the case of negative coupling ($\lambda < 0$). Figure 3.4 shows the concurrence $C(\rho)$ versus the atomic transition frequency ω for different values of temperature T. At a zero temperature the system is entangled if ω is below the critical value $\omega_c^- = -3\lambda$ (the minus sign refers to the *negative* coupling constant λ), where the states $|\psi_1\rangle$ and $|\psi_4\rangle$ cross. This is due to the fact that for $\omega > \omega_c^-$ the ground state is the saturated $|\psi_1\rangle$. We also find a local dip which appears at a point $\omega = \omega_d = -\lambda$. At this point a transition between the respective frustrated ground states $|\psi_7\rangle$ ($\omega < \omega_d$) and $|\psi_4\rangle$ ($\omega_d < \omega < \omega_c$) occurs. For $\omega = \omega_d$, $|\psi_4\rangle$ and $|\psi_7\rangle$ form a doubly degenerate ground state. Although, each of these states has a value of entanglement equal to 2/3, their mixture is less entangled (with a value of 1/4). Note that we have a transition between states with the same amount of entanglement ($C(\rho) = 2/3$) but different number of excited atoms. We remark, that a transition between different number of excited atoms becomes possible only due to the vacuum Stark shift term, present in (3.9). Considering the state $|\psi_4\rangle$ ($|\psi_7\rangle$), we also see that the probability of each of three atoms being excited (non-excited) is equal to 1/3. This is an analog of frustration in magnetic systems [47, 48].

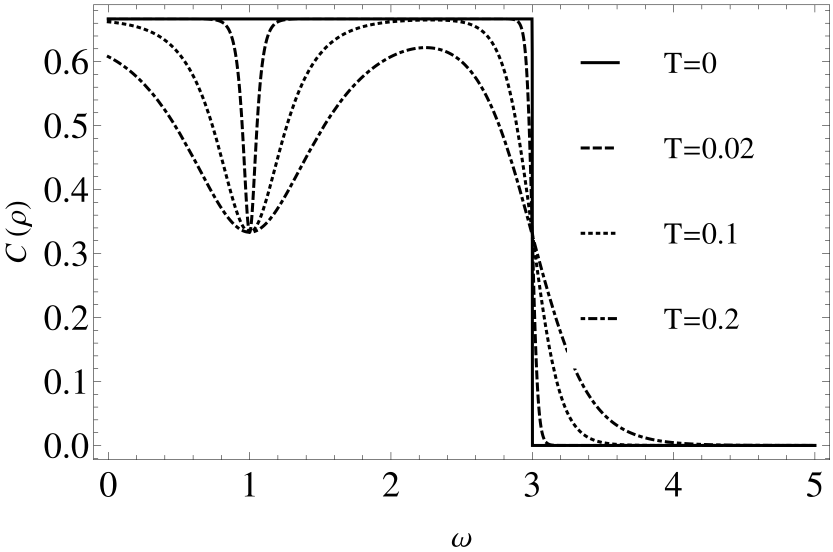

Figure 3.4: Concurrence $C(\rho)$ versus atomic transition frequency ω, for $\lambda = -1$ and different values of the temperature T.

Finally, the behavior of $C(\rho)$ versus temperature is exhibited in Fig. 3.5. When the ground state is not entangled, we find a similar picture as for the case of $\lambda > 0$ (see Fig. 3.3), but with a sudden death occurring for a larger temperature. When the ground state is entangled, we find a decrease of $C(\rho)$ and its eventual abrupt dying out a sudden-death temperature T_d.

3.2.6 Comparative studies of positive and negative coupling

The behavior of the sudden-death temperature T_d is analyzed in Fig. 3.6 for both cases of positive and negative couplings. Both curves in this figure tend to saturation temperature

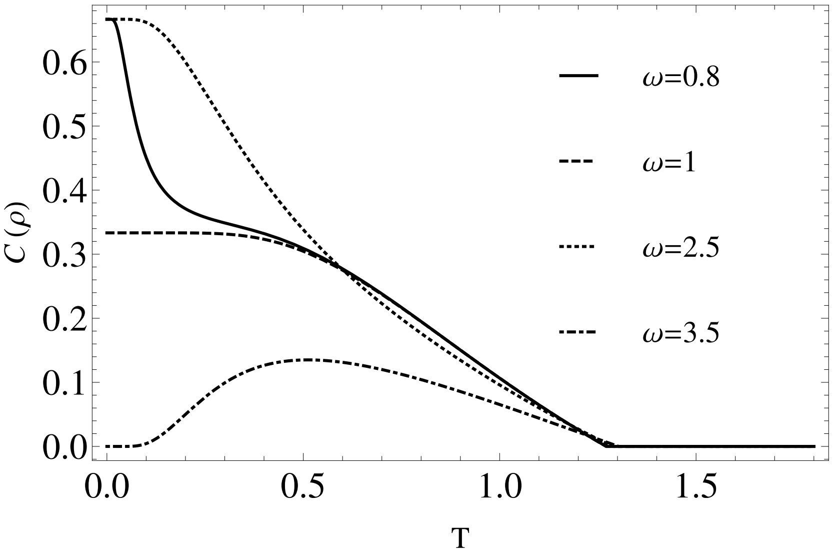

Figure 3.5: Concurrence $C(\rho)$ versus temperature T, for $\lambda = -1$ and different values of the atomic transition frequency ω.

T_s. The latter can be found from the equation

$$e^{\frac{\lambda}{T_s}}\sqrt{6e^{\frac{3\lambda}{T_s}}+3}-\left|e^{\frac{3\lambda}{T_s}}-1\right|=0. \tag{3.17}$$

The solution of Eq. (3.17) can be presented as $T_s/\lambda = const$, with the growth rate for T_s being higher for negative coupling strengths: $T_s/\lambda = -1.32639$ ($\lambda < 0$) in contrast with $T_s/\lambda = 0.554641$ ($\lambda > 0$). Another interesting effect can be found on Fig. 3.6: one can notice a non-monotonic behavior of T_d versus ω for $\lambda < 0$. If the vacuum Stark shift term was not taken into account, the temperature T_d would monotonically increase with ω.

Figure 3.7 shows a more global picture as three dimensional plots of $C(\rho)$ versus temperature and atomic transition frequency ω. One can infer that the case $\lambda < 0$ exhibits more robust entanglement behavior, both with respect to atomic frequency ω and the temperature T, as the system is entangled in a wider range of ω's and T's).

We make here another important remark. As mentioned above, the first level-crossing for the negative λ occurs at $\lambda = -\omega/3$, i.e. for a moderately strong coupling. Moreover, we additionally found that this crossing point behaves like $\lambda = -\omega/N$ (with N being the number of atoms) as well as for $N = 2, 3$ and 4. Thus, we anticipate that such a crossing will occur for a smaller λ (in absolute value) for a larger number of atoms N.

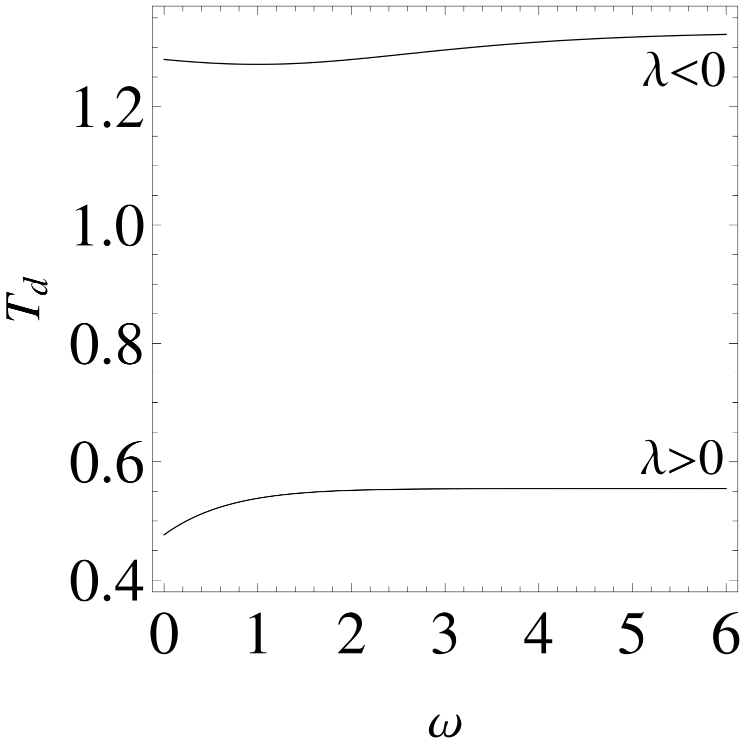

Figure 3.6: Sudden-death temperature T_d corresponding to the vanishing of entanglement versus transition eigenfrequency ω (in units of $|\lambda|$), for different signs of the coupling constant λ.

3.3 The stimulated Raman adiabatic passage in a medium of unequal oscillator strengths

3.3.1 The theoretical framework

The b-STIRAP process is defined with respect to population transfer in a three-level system, which we consider to possess a ground state $|1\rangle$, an excited state $|2\rangle$, and a final state $|3\rangle$ in which we wish to maximize the population (see Fig. 3.8). These matter states are coupled by two laser fields: a field that is resonant with the transition from the ground to the excited state (the pump field) and a field that is resonant with the excited to the final state transition (the Stokes field). The pump and Stokes pulses, detuned by $\Delta_{p,s}$ with respect to the corresponding resonances, have the Rabi frequencies Ω_p and Ω_s. The dressed eigenstates of the matter-field

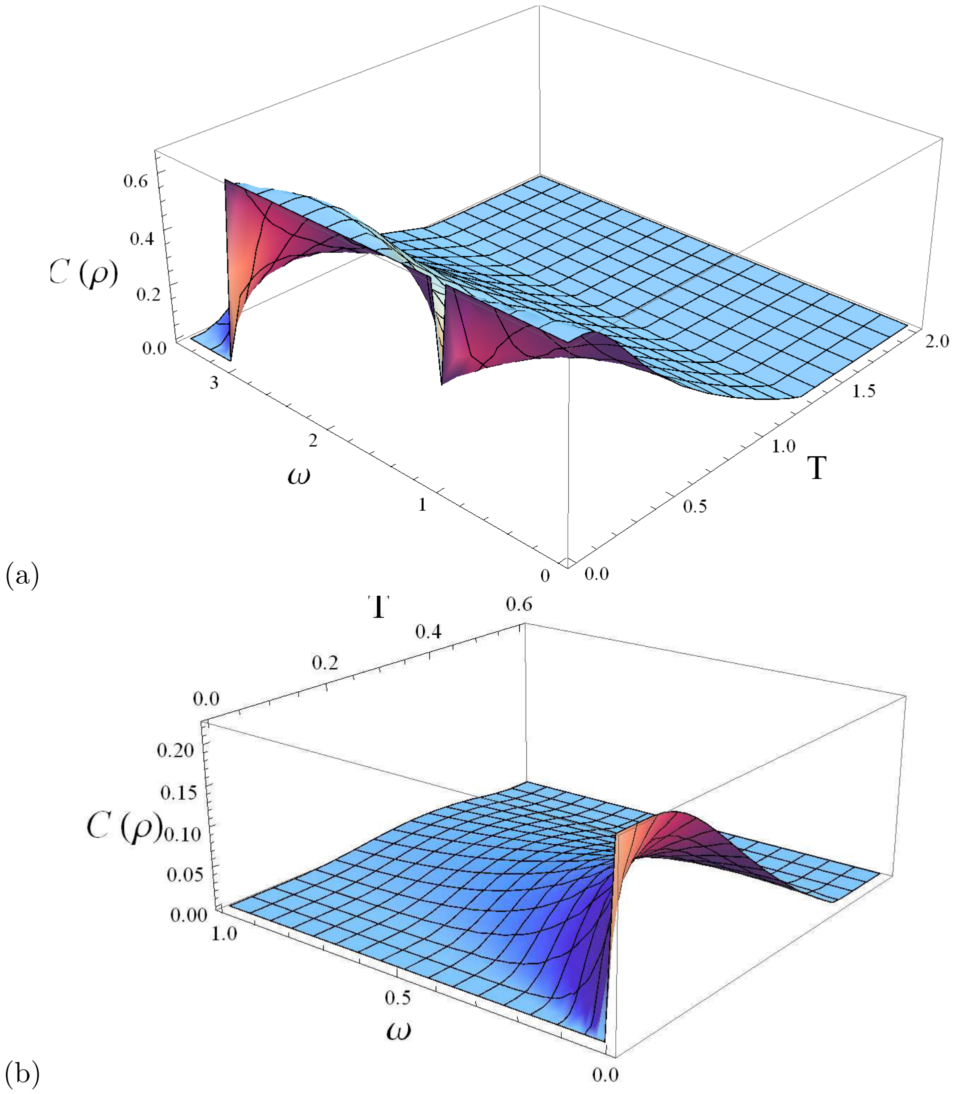

Figure 3.7: Concurrence $C(\rho)$ versus temperature T and atomic transition frequency ω, for (a) $\lambda = -1$; (b) $\lambda = 1$.

system in the case of exact-two photon resonance are well-known [130] and are given by

$$|b_1\rangle = \cos\psi \sin\theta |1\rangle + \cos\psi \cos\theta |3\rangle + \sin\psi |2\rangle, \tag{3.18a}$$

$$|b_2\rangle = \sin\psi \sin\theta |1\rangle + \sin\psi \cos\theta |3\rangle - \cos\psi |2\rangle, \tag{3.18b}$$

$$|d\rangle = \cos\theta |1\rangle - \sin\theta |3\rangle, \tag{3.18c}$$

where the time-dependent mixing angles are defined as $\tan\theta(t) = \Omega_p(t)/\Omega_s(t)$, and $\tan 2\psi(t) = 2\Omega(t)/\Delta_p$, with $\Omega(t) = \sqrt{\Omega_p^2(t) + \Omega_s^2(t)}$ being the generalized Rabi frequency. We assume that $\Delta_p > 0$ without loss of generality .

The central point of interest for b-STIRAP, among the dressed atomic eigenstates in

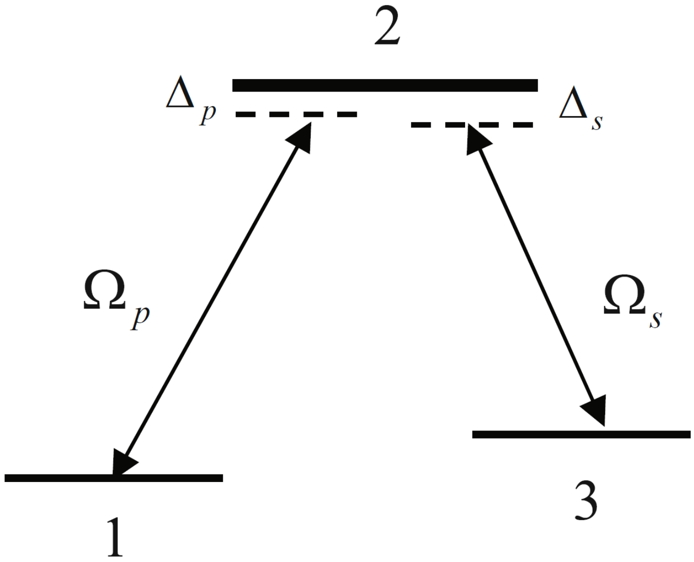

Figure 3.8: The three-level Λ-type system coupled by two near resonant pulses with Rabi frequencies Ω_p and Ω_s.

Eqs. (3.18), is the bright state $|b_1\rangle$ which is a linear combination of all three bare states $|1\rangle$, $|2\rangle$ and $|3\rangle$. Let $\Delta_p \neq 0$ and all population initially in $|1\rangle$. If the pump pulse precedes (but overlaps) the Stokes pulse, at time $t \to -\infty$, one finds for the mixing angles: $\theta = 90°$ and $\psi = 0°$. Thus the dressed state $|b_1\rangle$ corresponds to the bare state $|1\rangle$. Meanwhile, at the end of the interaction, at time $t \to \infty$, where the Stokes pulse is applied after the pump pulse, we have mixing angles of $\theta = 0°$ and $\psi = 0°$. Therefore, the state $|b_1\rangle$ becomes the bare state $|3\rangle$ (i.e., the population was projected onto the final state). If both dressing angles θ and ψ are varied slowly, i.e. by ensuring an adiabatic evolution, all population remains in $|b_1\rangle$. Additionally, there is a low probability that the system will make a non-adiabatic transition to another dressed state.

3.3.2 Description of the model

In the present section we study the population transfer from state $|1\rangle$ to state $|3\rangle$ by means of b-STIRAP taking into consideration propagation effects. We consider two time-dependent laser fields propagating in a medium of three-level atoms in the lambda configuration as shown in Fig. 3.8. We assume that both fields propagate in the positive x direction. Let

$$E_p(x,t) = \mathcal{E}_p(x,t)\cos(\omega_p t - k_p x - \varphi_p), \tag{3.19a}$$

$$E_s(x,t) = \mathcal{E}_s(x,t)\cos(\omega_s t - k_s x - \varphi_s), \tag{3.19b}$$

where $\mathcal{E}_p$ and $\mathcal{E}_s$ are the slowly varying envelopes of the electric fields of carrier frequencies ω_p and ω_s, wave numbers k_p, k_s and phases φ_p, φ_s. We assume that the temporal durations of both laser pulses are sufficiently short that we can neglect decay terms, such as arising from loss to other atomic states, spontaneous emission, or collisional dephasing effects.

The corresponding time-dependent Hamiltonian in the basis $\{|1\rangle, |2\rangle, |3\rangle\}$ in the Rotating Wave Approximation (RWA) reads [130]

$$H = \hbar \begin{pmatrix} 0 & -\Omega_p & 0 \\ -\Omega_p & \Delta_p & -\Omega_s \\ 0 & -\Omega_s & \delta \end{pmatrix}, \tag{3.20}$$

where the Rabi frequencies and the one- and two-photon detunings are defined as follows : $\Omega_{p,s} = |\mathcal{E}_{p,s} d_{p,s}|/2\hbar$ with $d_{p,s}$ being the transition dipole moments, $\Delta_p = \omega_2 - \omega_1 - \omega_p + \dot{\varphi}_p$, and $\delta = \omega_3 - \omega_1 - \omega_p + \omega_s + \dot{\varphi}_p - \dot{\varphi}_s$. Here dot means differentiation with respect to time.

The evolution of the populations in the system is determined by the time-dependent Schrödinger equation

$$i\frac{\partial a_1}{\partial t} = -\Omega_p a_2, \tag{3.21a}$$

$$i\frac{\partial a_2}{\partial t} = -\Omega_p a_1 + \Delta_p a_2 - \Omega_s a_3, \tag{3.21b}$$

$$i\frac{\partial a_3}{\partial t} = -\Omega_s a_2 + \delta a_3. \tag{3.21c}$$

All atoms are assumed to be initially in the ground state $|1\rangle$:
$a_1(-\infty, x) = 1$, $a_2(-\infty, x) = a_3(-\infty, x) = 0$. The propagation of the pulses is governed by the Maxwell wave equations which in the slowly varying envelope approximation can be reduced to two independent first-order wave equations for each individual pulse that in terms

of traveling coordinates $z = x/c, \tau = t - x/c$ reads [130]:

$$\frac{\partial \Omega_p}{\partial z} = -q_p N \operatorname{Im}(a_1^* a_2), \tag{3.22a}$$

$$\frac{\partial \Omega_s}{\partial z} = -q_s N \operatorname{Im}(a_3^* a_2), \tag{3.22b}$$

$$\Omega_p \frac{\partial \varphi_p}{\partial z} = q_p N \operatorname{Re}(a_1^* a_2), \tag{3.22c}$$

$$\Omega_s \frac{\partial \varphi_s}{\partial z} = q_s N \operatorname{Re}(a_3^* a_2). \tag{3.22d}$$

Here $q_{p,s} = 2\pi \omega_{p,s} d_{p,s}^2/\hbar c$ are the oscillator strengths of the atom-field couplings with N being the atomic number density.

The coupled equations (3.21) and (3.22) give a complete description of the problem we are considering. Analytical solution to the set of coupled equations for the case of equal oscillator strengths ($q_p = q_s$) was given and studied in the adiabatic approximation in [153]. It was shown that the efficiency of the population transfer in the case of equal oscillator strengths decreases rapidly with the propagation length for small one-photon detunings, $\Delta_p \sim \Omega$, meanwhile for large one photon detunings, $\Delta_p \gg \Omega$, the population transfer process is more efficient in the medium and can occur for longer propagation distances.

However, in most practical cases, the oscillator strengths of the allowed transitions are not equal. We will analyze what happens when the oscillation strengths of the corresponding transitions are different.

We first solve numerically the set of coupled Schrödinger-Maxwell equations (3.21) and (3.22), and in Sec. 3.3.6 we interpret them using approximate analytical solutions. Additionally, we define the ratio of the transition strengths $q = q_p/q_s$.

3.3.3 Numerical results and analysis

For the desired population transfer it is required that state vector $|\Phi\rangle$ follows adiabatically the bright $|b_1\rangle$ state in the course of the evolution: $|\langle b_1(z,\tau)|\Phi\rangle| \approx 1$. This is achieved by switching on the pulses in the intuitive order (the pump laser first) and by meeting the adiabaticity condition [256]

$$|\lambda_{b_1} - \lambda_{b_2}| \gg |\langle b_2|\dot{b_1}\rangle|, \tag{3.23a}$$

$$|\lambda_{b_1} - \lambda_d| \gg |\langle d|\dot{b_1}\rangle|, \tag{3.23b}$$

where λ_{b_1}, λ_{b_2} and λ_d are the eigenvalues associated with the dressed states $|b_1\rangle$, $|b_2\rangle$ and $|d\rangle$, respectively. These adiabaticity conditions are generally satisfied, for smooth pulses, if:

$$|\Delta_p T| \gg 1, \quad |\Delta_p T|\, \psi^2 \sim \Omega^2 T / |\Delta_p| \gg 1. \tag{3.24}$$

For the numerical investigation we consider Gaussian pulses at the medium entrance ($z = 0$) with equal durations and Rabi frequencies. The pulses should act in a way that eliminates transitions between different dressed states, i.e., they should satisfy conditions (3.24). For that we choose the following parameters for the pulses: $\Omega_0 T = \Delta_p T = 40$, $\tau_d/T = 1.3$, where τ_d is the time delay between the peaks of the pulses and Ω_0 is the peaks value of Ω. The chosen parameters correspond to the case $\Delta_p \simeq \Omega_0$.

3.3.4 Case of equal oscillator strengths

We start with the example when the oscillator strengths of the corresponding atomic transitions are equal, corresponding to $q = 1$. Figure 3.9 shows the time evolution of the propagating pulses (top left), atomic state populations (bottom left), state vector $|\Phi\rangle$ projections onto the dressed states (top right) and mixing angles θ and ψ (bottom right) at the entrance of the medium. The curves are obtained from a numerical solution of Eqs. (3.21)-(3.22) using the above mentioned parameters. The figure shows that the pulses induce a very efficient adiabatic population transfer. However, as the pulses propagate inside the medium, the population transfer efficiency rapidly decreases. Indeed, as one can see from Fig. 3.10, at the propagation length $q_s zNT = 7$ [see Fig. 3.10(a)] the population transfer is already not complete (the achieved efficiency is $\sim 95\%$), and at $q_s zNT = 20$ [see Fig. 3.10(b)] the transfer efficiency is reduced by a factor of 50 (the achieved efficiency $\sim 2\%$). The reason for such a loss of the efficiency of the transfer process is that during the propagation the

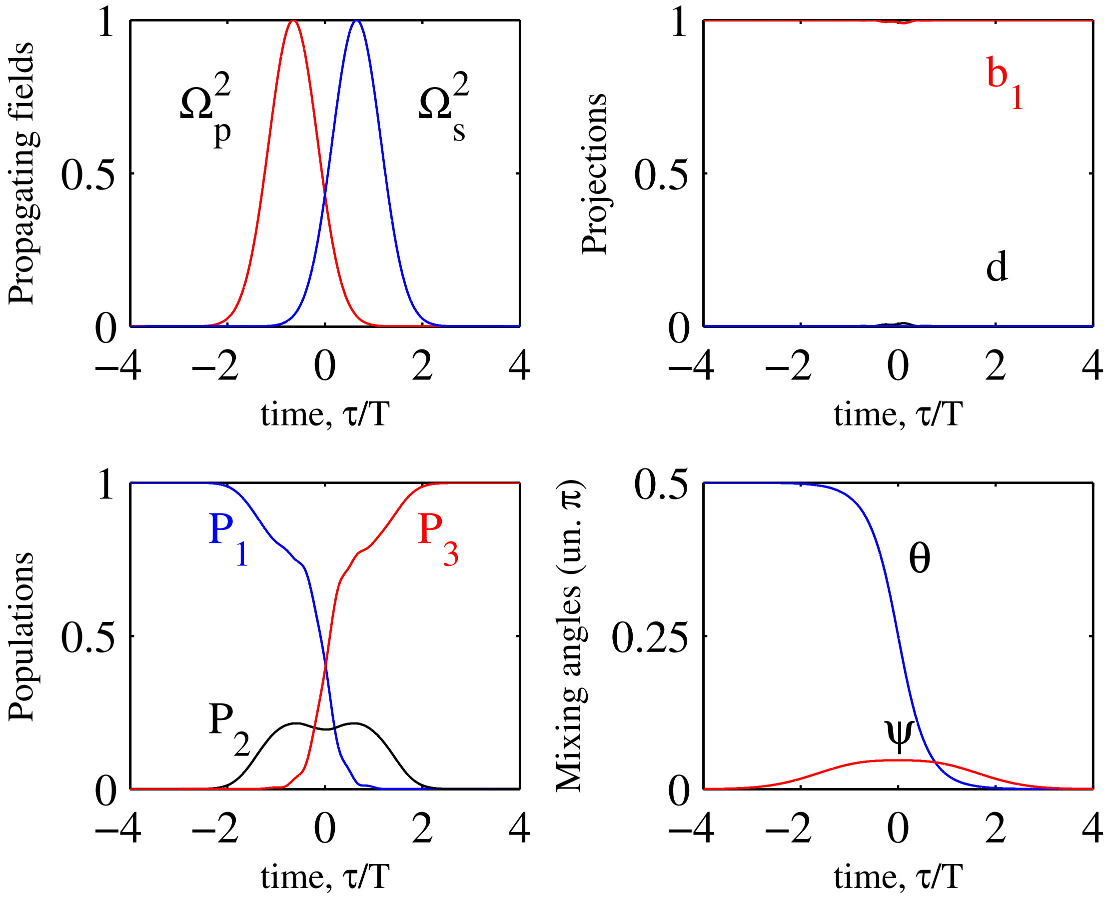

Figure 3.9: The interaction dynamics at the input face of the medium ($z = 0$) with equal oscillator strengths, $q_p = q_s$. Top left: propagating fields; top right: projections of the state vector $|\Phi\rangle$ onto dressed $|b_1\rangle$, $|d\rangle$ (projection on the state $|b_2\rangle$ is negligible); bottom left: atomic state populations; bottom right: mixing angles θ and ψ.

adiabaticity of the interaction is more and more disturbed. Indeed, the time evolution of the mixing angle $\theta(z,\tau)$ inside the medium is not anymore a smooth decreasing monotonic function (ensuring the evolution of the bright state $|b_1\rangle$ from the bare state $|1\rangle$ initially to the target state $|3\rangle$ at the end of the interaction), but reveals some oscillating behavior, resulting in nonadiabatic couplings (proportional to $\dot{\theta}$) between the adiabatic states. The violation of the adiabaticity is more apparent when we look at the top right panels in Figs. 3.10(a) (b) presenting the populations of the dressed states. One can see that the bright state $|b_1\rangle$ is not the only adiabatic state that is populated, as it is depopulated in the course of propagation and there appears a non-adiabatic coupling to the dark state $|d\rangle$, resulting in loss of transfer efficiency. This is what we also see from the top left panels presenting the atomic state populations $P_{1,3}$: the interference between different evolution paths leads to oscillations in the populations, rather than to complete population transfer.

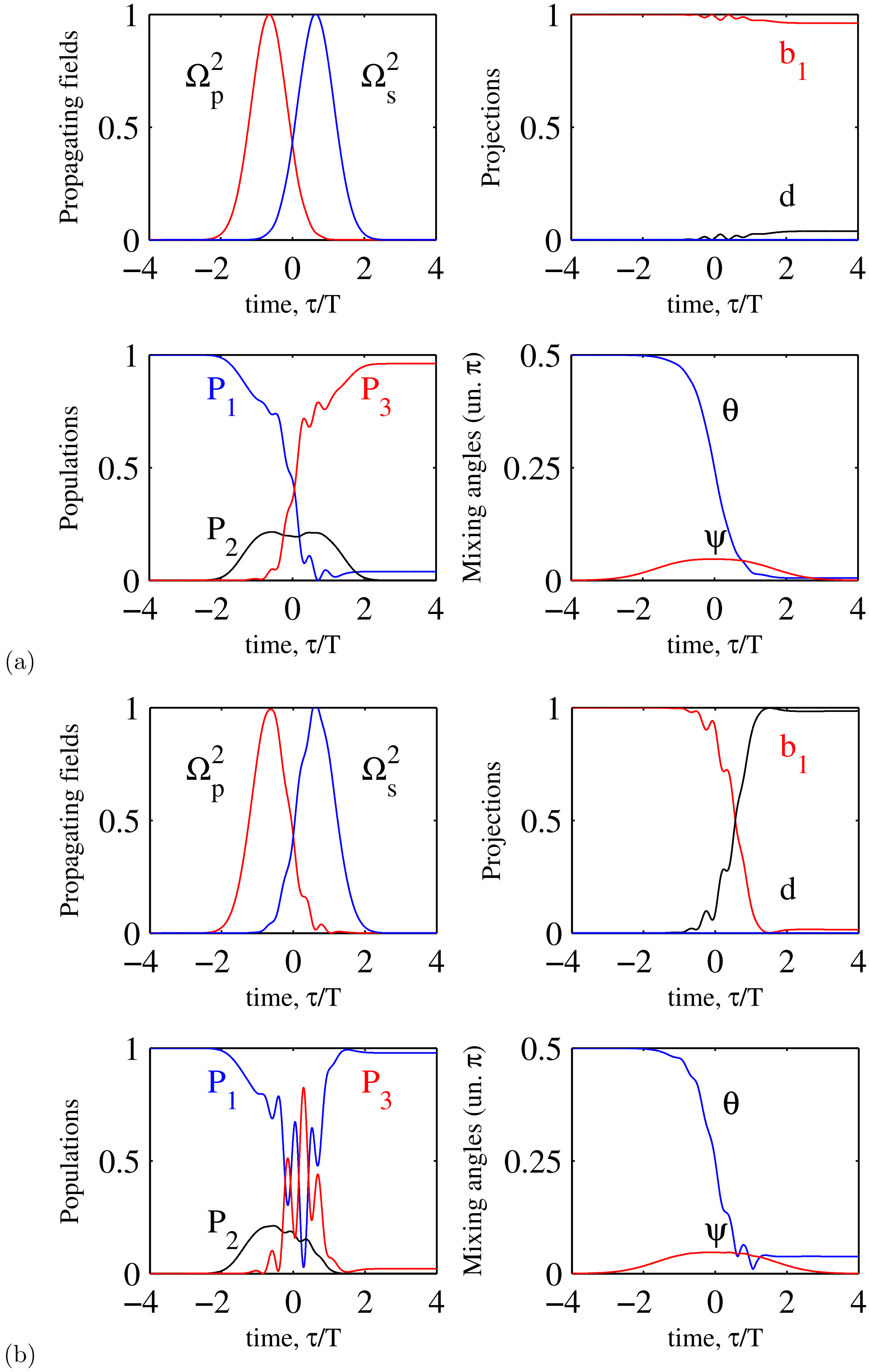

Figure 3.10: The same dynamics as in Fig. 3.9 but at the propagation length: (a) $q_s z N T = 7$. The efficiency achieved for population transfer is $\sim 95\%$; (b) $q_s z N T = 20$. The efficiency achieved for population transfer is $\sim 2\%$.

3.3.5 Case of unequal oscillator strengths

In this subsection we proceed with the same input conditions, but we lift the requirement of equal coupling constants. Figure 3.11 shows the time evolution of the propagating pulses (top left), atomic state populations (bottom left), state vector $|\Phi\rangle$ projections (top right) and dressing angles θ and ψ (bottom right) at the entrance of a medium with $q = 0.1$. As seen, in this case the pulses also provide an adiabatic evolution and a very efficient population transfer at the entry of the medium. We will study whether this capacity of propagating pulses is maintained or not in the course of propagation.

In Figs. 3.12(a), (b) we report a numerical plot of the dynamics of the propagating pulses and of the atomic system at the propagation lengths $q_s zNT = 7$ and $q_s zNT = 20$, respectively. As seen from the figures, in the course of propagation the interaction adiabaticity is better preserved as compared to the case $q = 1$. Indeed, at the propagation length $q_s zNT = 7$ the population transfer is still complete (compare with Fig. 3.10(a) where at this propagation length the transfer is already not perfect). As to the propagation length $q_s zNT = 20$, the situation is not perfect. However, the time dependence of the mixing angle θ is without pronounced peaks, its final value goes to zero, and the majority of population (about 87.5 %) is transferred to the final state $|3\rangle$ [compare this result with 2% in case of equal oscillator strengths, see Fig. 3.10(b)]. It is also notable that while in the case of $q = 1$ the pulses are considerably distorted at this propagation length, in case of $q = 0.1$ the pulse distortion is much less [compare top left panels in Figs. 3.10(b) and 3.12(b)]. Even though the pulses produce perfect adiabatic population transfer at the entry into the medium both for $q = 1$ and $q = 0.1$, in the course of propagation they maintain this ability much longer in case of $q < 1$ as compared to the case where $q = 1$.

Consider now a medium of unequal oscillator strengths such that $q > 1$. The dynamics of the transfer process together with the pulse shapes for this case is shown in Figs. 3.13 and 3.14 for $q = 10$. It is seen that the population transfer process in the medium is less efficient compared to the cases $q = 0.1$ and $q = 1$. Indeed, by comparing Figs. 3.10(a), 3.12(a) and

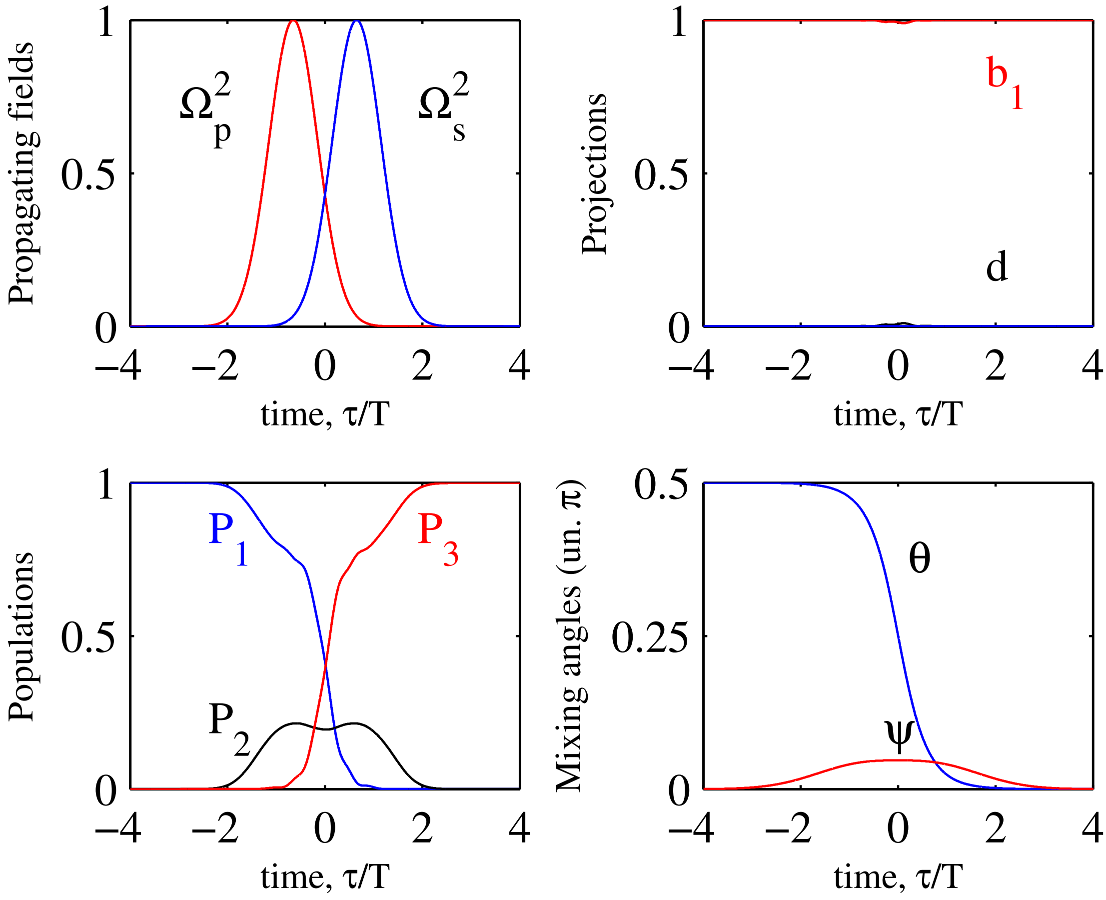

Figure 3.11: The dynamics at the input face of the medium with unequal coupling constants, $q = 0.1$. Top left: propagating fields; top right: projections of the state vector $|\Phi\rangle$ onto dressed b_1, d; bottom left (projection on the state $|b_2\rangle$ is negligible): atomic state populations; bottom right: mixing angles θ and ψ.

3.14(a) one can see that while for $q \leq 1$, at the propagation length $q_s zNT = 7$, the population transfer works quite well, in case of $q = 10$ the efficiency of the transfer already at this length is far from perfect ($\sim 25\%$). So, in this case, in the course of propagation in the medium, the adiabaticity breaks down rather quickly, and both pulses undergo severe reshaping and, consequently, loose their capacity to produce an effective population transfer. Hence, the case $q > 1$ is more harmful to the transfer process than that of $q \leq 1$. In conclusion to this subsection one can see that the pulse dynamics depends on the ratio of the oscillator strengths as they characterize the speed of energy transfer from the pulses to the medium and vice-versus.

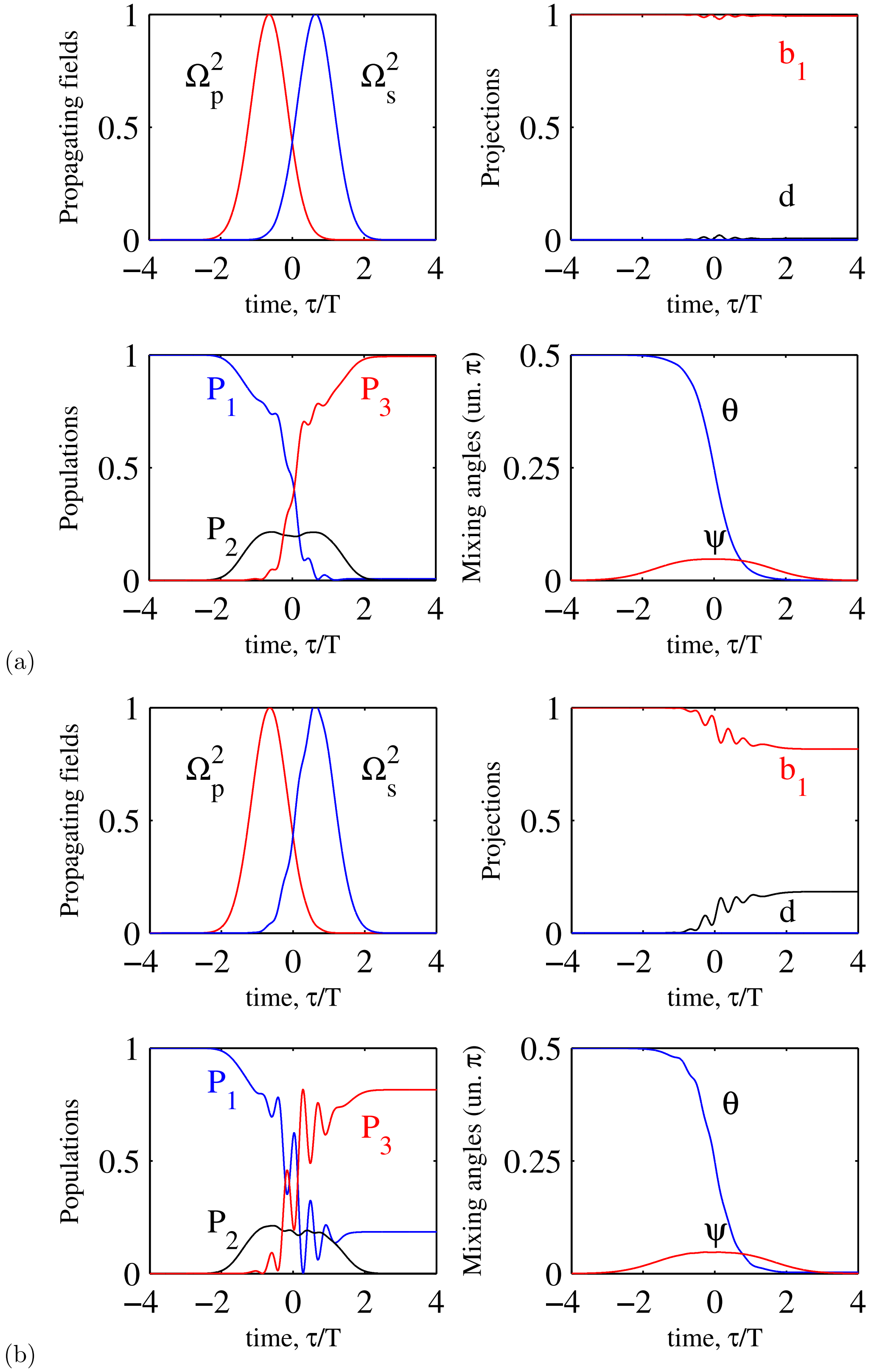

Figure 3.12: The same dynamics as in Fig. 3.11 but at the propagation length: (a) $q_s zNT = 7$. The efficiency achieved for population transfer is 100%; (b) $q_s zNT = 20$. The efficiency achieved for population transfer is 87.5%.

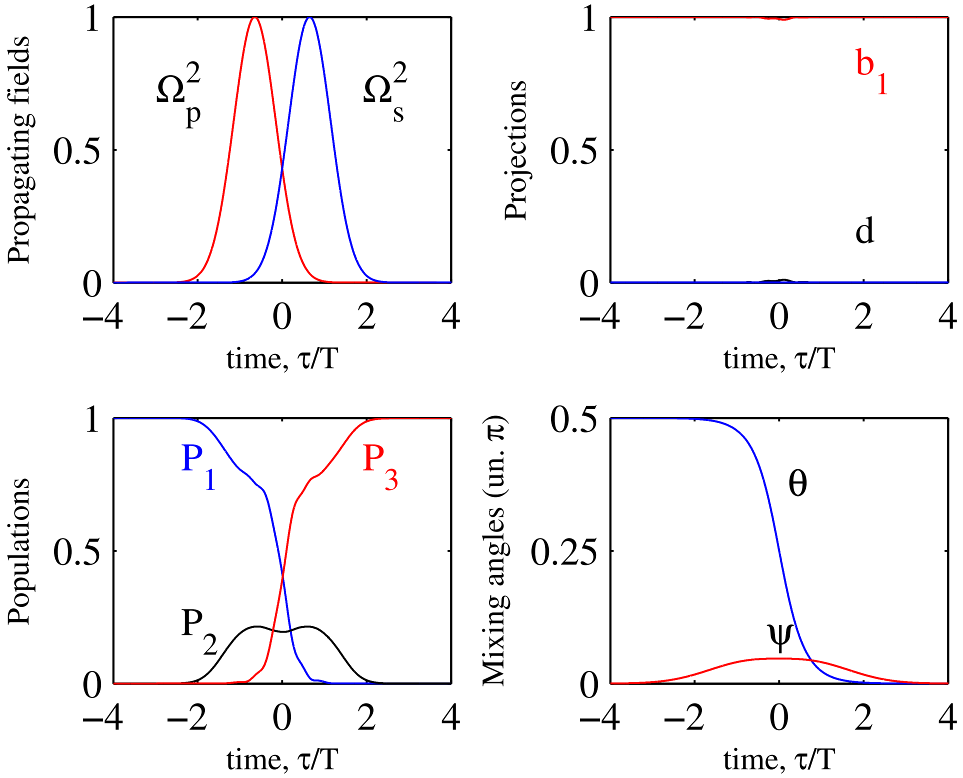

Figure 3.13: The dynamics at the input face of the medium with unequal coupling constants, $q = 10$. Top left: propagating fields; top right: projections of the state vector $|\Phi\rangle$ onto dressed $|b_1\rangle$, $|d\rangle$ (projection on the state $|b_2\rangle$ is negligible); bottom left: state populations; bottom right: mixing angles θ and ψ.

3.3.6 Analytical solutions

We now focus our attention on approximate analytical solutions that give an explanation for the above numerical results.

By combining Maxwell and Schrödinger equations and differentiating the phase equations (3.22c) and (3.22d) with respect to time we obtain the following system of equations for the Rabi frequencies $\Omega_{p,s}$ and the one-photon detunings $\Delta_{p,s}$

$$\frac{\partial \Omega_p^2}{\partial z} = q_p N \frac{\partial}{\partial \tau} |a_1|^2, \tag{3.25a}$$

$$\frac{\partial \Omega_s^2}{\partial z} = q_s N \frac{\partial}{\partial \tau} |a_3|^2, \tag{3.25b}$$

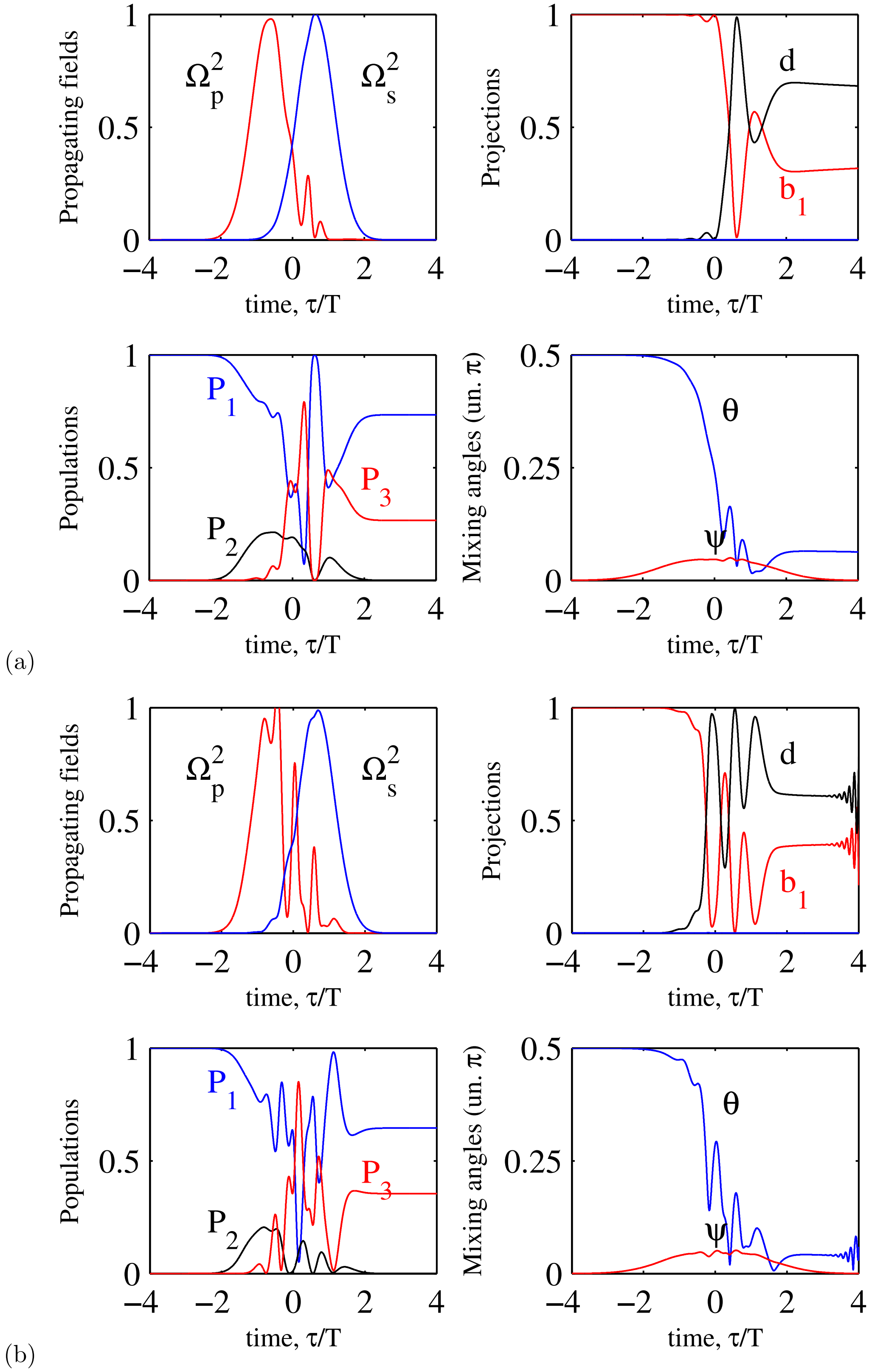

Figure 3.14: The same dynamics as in Fig. 3.13 at the propagation length: (a) $q_s zNT = 7$. The efficiency achieved for population transfer is 25%; (b) $q_s zNT = 20$. The efficiency achieved for population transfer is 34%.

$$\frac{\partial \Delta_p}{\partial z} = q_p N \frac{\partial}{\partial \tau} \frac{\mathrm{Re}(a_1^* a_2)}{\Omega_p}, \tag{3.26a}$$

$$\frac{\partial \Delta_s}{\partial z} = q_s N \frac{\partial}{\partial \tau} \frac{\mathrm{Re}(a_3^* a_2)}{\Omega_s}. \tag{3.26b}$$

Equations (3.26) describe the change in carrier frequencies of the pulses during propagation in a non-linear medium due to the parametric broadening of the pulse spectrum (phase-self modulation).

In the process we are concerned with, the population of the level $|1\rangle$ decreases $\big(\partial|a_1|^2/\partial\tau < 0\big)$, while that of the third level increases $\big(\partial|a_3|^2/\partial\tau > 0\big)$. Hence, the intensity of the pump pulse decreases proportionally to q_p, and that of the Stokes one increases proportionally to q_s. Choosing a medium with a small value of $q = q_p/q_s$, we slow down the process of pump pulse depletion (but not the process of Stokes pulse amplification), so one would expect to extend the population transfer process up to longer propagation lengths for such media.

From Eqs. (3.25) we obtain immediately the following equation of motion for the total photon number density $n = \left(\frac{\Omega_p^2}{q_p} + \frac{\Omega_s^2}{q_s}\right)$, since the system is conservative ($|a_1|^2 + |a_2|^2 + |a_3|^2 = 1$):

$$\frac{\partial n}{\partial z} = -N \frac{\partial |a_2|^2}{\partial \tau}. \tag{3.27}$$

According to this equation, the total photon number density $n(z,\tau)$ during the propagation of the pulses in the medium is not conserved if the intermediate level $|2\rangle$ is populated, i.e. a part of the energy of the pulses is transferred to the medium.

We introduce now a quantity $Q = \dfrac{\Omega^2}{n}$ that we call two-photon transition strength (similar to $q_{p,s} = \Omega_{p,s}^2/n_{p,s}$) defined as

$$Q = \frac{q_s q_p}{q_s \sin^2\theta + q_p \cos^2\theta}. \tag{3.28}$$

Note that in the case of equal oscillator strengths ($q_p = q_s = q$) $Q = q$, while for $q_p \neq q_s$ Q is a function of both time and propagation length $Q = Q(z,\tau)$.

From Eqs. (3.25) and (3.28), using the adiabatic approximation along the eigenstate $|b_1\rangle$ [see Eq. (3.18)] and the definition of the two-photon detuning, we arrive at the following system of propagation equations for n and δ

$$\frac{\partial n}{\partial z}+\frac{N\Delta_p Q}{(\Delta_p^2+4nQ)^{3/2}}\frac{\partial n}{\partial \tau}=-\frac{Nn\Delta_p}{(\Delta_p^2+4nQ)^{3/2}}\frac{\partial Q}{\partial \tau}, \tag{3.29}$$

$$\frac{\partial \delta}{\partial z}=\frac{2(q_p-q_s)}{\Delta_p}\frac{\partial n}{\partial z}. \tag{3.30}$$

As can be seen from these equations, the evolution dynamics of both, n and δ, during the pulse propagation in the medium is clearly dependent on the ratio of q_p and q_s. Indeed, in case of equal transition strengths ($q_p = q_s$) the condition of two-photon resonance ($\delta = 0$) is kept automatically. However, for unequal oscillator strengths ($q_p \neq q_s$), the two-photon detuning δ is affected by the evolution dynamics of $n(z,\tau)$, and the condition of two-photon resonance can be broken during the propagation of the pulses in the medium. So, self-phase modulation can start to develop as the pulses propagate inside the medium leading to a change in the spectra of both pulses, and consequently to the destruction of the bright state $|b_1\rangle$.

However, the analysis of Eq. (3.29) shows that $\frac{\partial n}{\partial z} \sim 0$ at the propagation length satisfying the condition

$$\frac{\Delta_p Q N}{(\Delta_p^2+4nQ)^{3/2}T}z \ll 1, \tag{3.31}$$

which at large one-photon detunings reduces to

$$\frac{QN}{\Delta_p^2 T}z \ll 1. \tag{3.32}$$

Under this condition the two-photon resonance is preserved: $\frac{\partial \delta}{\partial z} \approx 0$. Condition (3.32) is similar to that of the generalized adiabaticity for a simple two-level system when replacing the two-photon oscillator strength by a one-photon oscillator strength.

Note that when deriving Eq. (3.30) we neglected the time dependence of the one-photon detuning Δ_p which is valid for large initial values of this parameter and at the propagation lengths satisfying the condition (3.32).

Thus, provided that one remains in the regime given by the condition (3.31), the conservation law of the total photon number density is guaranteed in case of different transition strengths, i.e. $n(z,\tau) = n_0(\tau)$, and one can neglect small deviations from the two-photon resonance condition.

In case of equal oscillator strengths ($q_p = q_s$) the dynamics of the photon number density n in a medium coincides with that of the generalized Rabi frequency Ω and is studied in [153]. As shown in this subsection, the photon number density n propagates in a medium with a non-linear group velocity less than c. In this case the condition (3.31) means that the group delay in the medium is negligibly small.

3.3.7 Equations and solutions for the mixing angle θ: superluminal population transfer.

As seen from the numerical study performed in Sec. 3.3.3, the mixing angle $\theta(z,\tau)$ appears to be the key dynamical parameter in the interaction between the atoms and the fields. In order to follow the propagation dynamics of the angle $\theta(z,\tau)$ we will derive an evolution equation for $\theta(z,\tau)$.

Using the definitions of θ, Ω and Q, we obtain the following expressions for $\Omega^2_{p,s}$

$$\Omega_p^2(z,\tau) = nQ(\theta(z,\tau))\sin^2(\theta(z,\tau)), \tag{3.33a}$$

$$\Omega_s^2(z,\tau) = nQ(\theta(z,\tau))\cos^2(\theta(z,\tau)). \tag{3.33b}$$

A suitable combination of Eqs. (3.25) and (3.33), yields the desired evolution equation for $\theta(z,\tau)$:

$$\sin 2\theta(z,\tau)\left[\frac{\partial\theta(z,\tau)}{\partial z} - \frac{q_p q_s N}{Q^2(\theta(z,\tau))}\frac{\cos^2\psi}{n_0}\frac{\partial\theta(z,\tau)}{\partial\tau}\right] = 0. \tag{3.34}$$

This equation is a central equation of our study that helps to understand the main properties and limitations for population transfer process during propagation in a medium.

For simplicity we consider the case of large one-photon detunings ($\Delta_p T \gg 1$) where $\cos^2\psi \sim 1$. In this case Eq. (3.34) can be solved analytically by the method of characteristics as in Ref. [148], and the solution reads

$$\theta(z,\tau) = \theta_0(\xi), \tag{3.35}$$

where $\theta_0(\xi) \equiv \theta(z=0, \tau=\xi)$ is the function given at the medium entrance, $z=0$. Here $\xi(z,\tau)$ is an implicit function governing the nonlinear propagation of the pulses and determined from the following integral equation

$$\int_{-\infty}^{\xi} n_0(\tau')d\tau' = \int_{-\infty}^{\tau} n_0(\tau')d\tau' + \frac{q_p q_s}{Q^2(\xi(z,\tau))}Nz. \tag{3.36}$$

Equation (3.36) defines the "nonlinear" time $\xi = \tau - z/u(z,\tau)$ with $u(z,\tau)$ being the "nonlinear" velocity at which the mixing angle θ propagates. As seen from this equation, at the medium entrance ($z=0$) $\xi=\tau$, while inside the medium ($z \neq 0$) the nonlinear time ξ is larger than τ: $\xi > \tau = t - x/c$. This means that the mixing angle $\theta(z,\tau)$ propagates with a velocity exceeding the light speed in vacuum c, i.e. superluminally.

3.3.8 The adiabaticity criterion

The obtained analytical result (3.35) relies on the adiabaticity condition (3.23) requiring the energy spacing between the eigenvalues to be much larger than the dynamic coupling term (given by $\dot{\theta}$) which ensures the adiabatic following of the bright state $|b_1\rangle$ during the propagation of the pulses. Let us see whether the adiabaticity condition satisfied at the medium entrance remains valid in the course of propagation.

With propagation effects taken into account, the time derivative $\dot{\theta}$ takes the form $d\theta_0/d\tau = (d\theta_0/d\xi)\partial\xi/\partial\tau$. So, even though we impose at the medium entrance a small derivative $d\theta_0/d\xi$, the adiabaticity condition can break down, since during the propagation process the derivative $\partial\xi/\partial\tau$ can become considerably large. Indeed, differentiating Eq. (3.36) with respect to τ, we obtain for the derivative $\partial\xi/\partial\tau$

$$\frac{\partial\xi}{\partial\tau} = \frac{n_0(\tau)}{n_0(\xi)}A^{-1}, \tag{3.37}$$

with

$$A = 1 - \frac{2(q_s - q_p)}{\Omega_0^2(\xi)}Nz\frac{d\theta_0(\xi)}{d\xi}\sin 2\theta, \tag{3.38}$$

where $\Omega_0(\xi)$ is the function given at the medium entrance, $z=0$. As seen from the obtained equation, at small values of A the derivative $\partial\xi/\partial\tau$ becomes large leading to the violation of the adiabaticity condition. The adiabaticity condition is satisfied if $A \geqslant 1$, namely under the following condition

$$(q_s - q_p)\frac{d\theta_0}{d\xi}\sin 2\theta_0 \leqslant 0. \tag{3.39}$$

In particular, for a medium with equal transition strengths ($q_s = q_p$) we have $A = 1$. For an intuitive pulse sequence the angle θ changes from $\pi/2$ to 0, so the derivative $\frac{d\theta_0(\xi)}{d\xi} \leqslant 0$ throughout the interaction. Hence, in the case where $q_s \geqslant q_p$ the factor A is always more than 1, and consequently, the adiabaticity condition in principle never breaks down during the propagation process. In the opposite case of $q_s < q_p$, at the propagation lengths defined by the following condition

$$z \approx -\frac{\Omega_0^2 T}{2(q_s - q_p)}, \tag{3.40}$$

the factor $A \to 0$, and consequently $\partial\xi/\partial\tau \to \infty$ ($\dot{\theta} \to \infty$). The condition $q_s < q_p$ means that the probability of the transition $|1\rangle \to |2\rangle$ is greater than that of the transition $|2\rangle \to |3\rangle$ and, thus, the population transfer $|1\rangle \to |2\rangle$ dominates the depletion of level $|2\rangle$, i.e., the interaction adiabaticity breaks down, and the state $|b_1\rangle$ does not carry the dynamics anymore.

Thus, the generalized condition for the interaction adiabaticity is very sensitive to the ratio of the transition strengths on the adjacent transitions. Note that the increase in the derivative $\partial\theta/\partial\tau$ during the propagation process (i.e. increase of the influence of superadiabatic corrections) is a property of media consisting of atoms with nonequal transition strengths.

The above arguments are illustrated in Fig. 3.15 presenting the time evolution of the mixing parameter $\theta(z,\tau)$ as given by Eq. (3.36) for different values of the parameter q at the propagation length $q_s zNT = 20$. Identifying the slope of θ as the measure of nonadiabaticity, we can see from this figure that the evolution of the mixing parameter is more adiabatic in the case where $q = 0.1$ (dashed curve), while for $q = 14$ (full curve) the slope becomes steeper in the course of propagation, implying that the adiabaticity condition breaks down. So, the population transfer process is more stable against the nonadiabaticity caused by nonequality of coupling constants in case of $q_p \leqslant q_s$.

The analytical solution given above is valid in the region where both pulses overlap, and

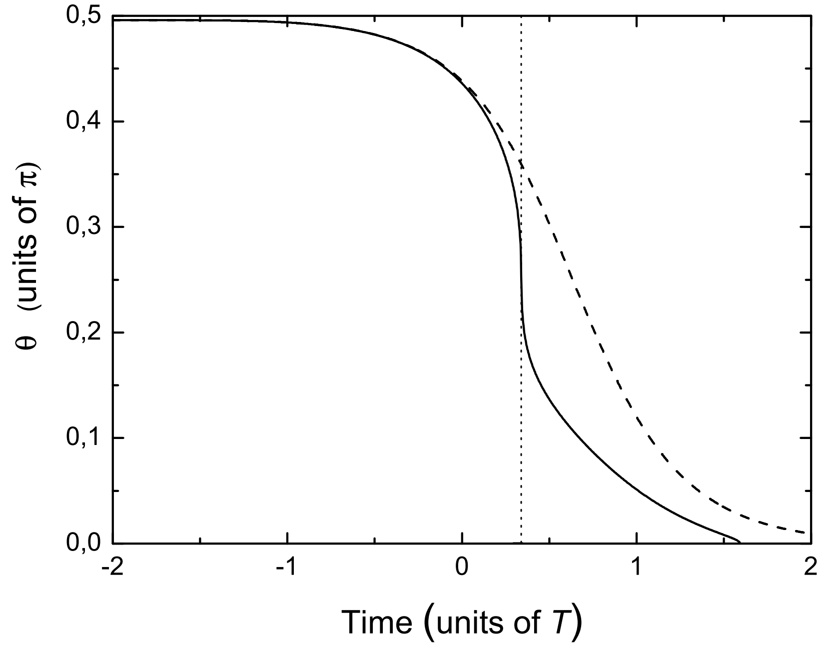

Figure 3.15: Time evolution of the mixing parameter θ for different relationships between q_p and q_s : $q = 0.1$ (dashed curve), and $q = 14$ (full curve) at the propagation length $q_s z N T = 20$. The dotted line corresponds to the case where $\dot{\theta} \rightarrow \infty$, i.e., when the adiabatic approximation breaks down.

where the two-photon resonance is physically significant. The overlapping region is defined by $\Omega_p \Omega_s = \Omega^2 \sin 2\theta \neq 0$. Note that outside the overlapping region where $\Omega \rightarrow 0$, even for an isolated atom the adiabaticity condition (3.23) can not be satisfied.

3.3.9 Population transfer in the adiabatic limit

We now investigate the possibility of a complete population transfer during the pulse propagation in the medium in the adiabatic limit. In this limit the population of the final level evolves as

$$P_3(z,\tau) = \cos^2 \psi(z,\tau) \cos^2 \theta_0(\xi(z,\tau)). \tag{3.41}$$

Taking $\cos^2 \psi \sim 1$ (which is valid for large single-photon detunings), we see that a complete population transfer in the medium at a given propagation length z occurs when $\theta_0(\xi) = 0$ which is realized at the times $\xi(z,\tau) \rightarrow \infty$. Setting $\xi(z,\tau)$ equal to ∞ in the analytical

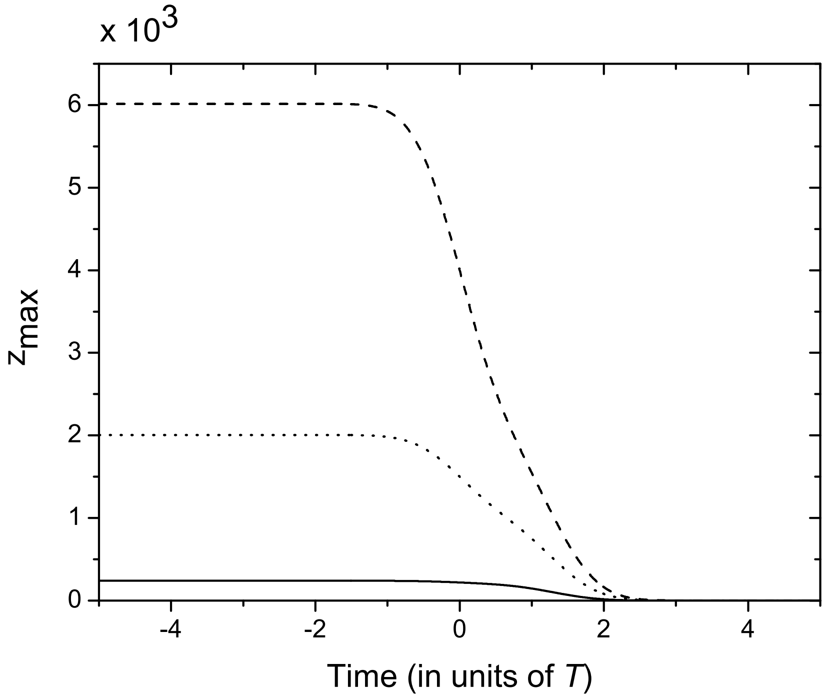

Figure 3.16: The maximal propagation length $z_{max}(\tau)$ ($\equiv q_s z_{max} NT$) as given by Eq. (3.43) for different relationships between q_p and q_s: $q = 0.5$ (dashed curve), $q = 1$ (dotted curve) and $q = 5$ (full curve). The curves delimit the regions where the analytical solution obtained can be applied.

solution (3.36), we can obtain from the curve $z(\tau)$ defined from the following equation

$$\int_{\tau}^{\infty} n_0(\tau')d\tau' = (q_p/q_s)Nz(\tau), \tag{3.42}$$

a set of points (located on $z(\tau)$) at which the population transfer is complete. The question is whether for each given value of z there exists τ such that Eq. (3.42) is satisfied. As one can see, at the medium entrance ($z = 0$) a complete population transfer is realized at the end of the interaction ($\tau \to \infty$), while for atoms located at $z \neq 0$, a complete transferral process occurs at earlier times τ (before the interaction is switched off). As compared to an isolated atom, the population transfer process via b-STIRAP in a medium is a faster process, that is, a superluminal population transfer, as long as the distortion of the pulses do not prevent adiabatic passage.

In principle, Eq. (3.42) leads to the maximal propagations length z_{max} defined by the equation

$$\int_{-\infty}^{\infty} n_0(\tau')d\tau' = (q_p/q_s)Nz_{max}, \tag{3.43}$$

beyond which population transfer cannot occur. This means in terms of energy that population transfer can in principle lasts until the transfer process uses all the photons available in the pulses.

Figure 3.16 shows the normalized value of z_{max} as given by solution (3.43) for different values of the ratios between q_p and q_s. The analytical solution obtained can not be applied beyond the regions delimited by the presented curves. Besides condition (3.31), we thus obtain a second limitation on propagation lengths at which our solution is valid.

The physical meaning of the maximal propagation length z_{max} given by Eq. (3.43) becomes more clear in case of equal oscillator strengths. Indeed in this case on the left-hand side of Eq. (3.43) we have the total number of photons in both pulses N_{ph} passing through the unit area, and on the right-hand side of this equation we have the total number of atoms Nz_{max} interacting with the radiation in the unit area. So, in the completely symmetric case where the number of photons in the pump and Stokes pulses are equal, it has a trivial meaning: two photons correspond to each atom of the medium where the population transfer occurs at a two-photon resonance. In the asymmetric case, considered in the present subsection, we have an "effective photon number" given by

$$(q_p/q_s)N_{ph} = N_{atoms}. \tag{3.44}$$

As follows from the above theoretical analysis, for small propagation lengths at which pulse deformations are still negligible, the population transfer process does not differ from that of an isolated atom. However, at large propagation lengths the population transfer process becomes faster. The transfer process is restricted up to certain propagation lengths determined from the conditions (3.31) and (3.43) that should be met for a successful transfer. In case of $q_p/q_s > 1$ there is an additional limitation on the propagation length given by the adiabaticity condition (3.40). The propagation length z_{max} [as given by Eq. (3.43)] at which a complete population transfer is possible in a medium is the smallest length among those defined by the conditions (3.31) and (3.40). To estimate propagation distances z, we consider a set of parameters relevant to a typical alkali atom vapor: $N = 10^{13}$ atoms/cm^3, $\omega = 10^{15}$ s^{-1}, $d \simeq 0.8 \times 10^{-17}$ SGS units, $T = 10^{-9}$ s. Estimations show that $q_s zNT = 1$ corresponds to $z \approx 0.05$ cm. For a medium with $q = 0.5$ an efficient b-STIRAP transfer is possible, in principle, up to $z = 300$ cm, while for $q = 5$ it is limited up to $z = 13$ cm.

3.4 Summary

1. We studied the entanglement and statistical properties of three atoms, coupled by means of a dipole-dipole interaction induced by a single cavity mode. The properties of the system are described by the Dicke model in the so-called dispersive limit. We pointed out the strong relation of the present model to problems of frustrated magnetism and the relative simplicity of the interaction strength tunability, what is rather complicated in the case of solids.

2. We considered the entanglement critical properties, namely, the critical temperature and transition eigenfrequency values, corresponding to vanishing of entanglement. Additionally, two, physically distinct regimes, depending on the sign of the interaction strength were revealed. We showed that the case of negative coupling strength is more robust with respect to the entanglement properties.

3. On the other hand, a detailed study of population transfer process via b-STIRAP in a medium of three-level Λ-atoms with unequal oscillator strengths of corresponding atomic transitions is performed. The propagation equations describing the dynamics of the process have been derived and approximate analytical solutions have been obtained.

4. We revealed the sensitivity of the transfer efficiency to the ratio of the oscillator strengths, $q = q_p/q_s$, and pointed out that the transfer efficiency is severely affected in the case of $q > 1$ and rapidly decreases with the propagation length. Meanwhile, in the case of $q \leqslant 1$, propagating pulses maintain their capacity to produce a complete population transfer over larger propagation lengths.

5. The conditions restricting the propagation length at which a complete population transfer via b-STIRAP in a medium occurs are derived.

Chapter 4

ENTANGLEMENT DISTILLATION IN REALISTIC QUANTUM MEMORIES [1]

4.1 Introduction

Efficient distribution of entanglement between distant parties is fundamental to essentially all practical applications of quantum information science. However, entanglement is fragile and suffers from decoherence, which is detrimental to the performance of any communication protocol upon which it relies. Thus, entanglement distillation, which allows to increase entanglement between communicating parties, becomes vitally important for realization of most quantum communication protocols. Particularly, continuous-variable entanglement distillation protocols are currently considered to be relatively easy to implement within existing technologies. The essential entanglement resource here is provided through Gaussian two-mode squeezed states, which are relatively easy to produce in the laboratory. These states are widely used in the realization of several other quantum protocols, including dense coding, entanglement swapping and others [257–259]. The continuous-variable entanglement distillation protocols [156, 157] circumvent restrictions imposed by the no-go theorem relating to the distillation of entanglement using only Gaussian local operations and classical communi-

---

[1] The results considered in this chapter are published in Ref. [170].

cation [260–262]. Namely, the proposed procedure offers a complete distillation of Gaussian states to (asymptotically exact) Gaussian states, but via non-Gaussian territory. Implementation of some elements of the scheme has already been reported [263–266], though a full demonstration is still lacking. This is due to demanding technical specifications [267] and the exponential resource requirements of the protocol. The "de-Gaussification" of the initial state plays a crucial role in this protocol and can be achieved by subtracting a photon from the initial state. Note that this process itself can increase the entanglement in the state. Different strategies for enhancing quantum entanglement in continuous-variable systems within this technique have been found [268].

A continuous-variable entanglement distillation protocol using quantum memories was recently proposed in Ref. [158]. This scheme uses the same space for both Gaussification and "de-Gaussification". Moreover, it has doubly-exponential temporal and exponential spatial advantage over the earlier procedures. This compact protocol involves only four quantum memories, allowing one to store results from previous iterations while the subsequent ones succeed [269], bringing about an exponential advantage in time. Additionally, one can repeatedly perform probabilistic operations on the same copy of a quantum state, without starting the whole process anew as in the case of a failure of a probabilistic local operation. Another resource-saving comes from the asymmetric Gaussification procedure: in contrast with earlier schemes, where two identical states are used, in the present protocol one operates on a fixed resource state and a distinct current state. This approach results in an additional exponential saving in time (we provide more details on this later). Note that another Gaussifying scheme, which circumvents the need for a growing memory, was proposed in Ref. [270]. The protocol, referred to as the pumping Gaussifier, uses a fixed initial state to repeatedly pump a target state and results in the same output as an analogous recursive protocol.

In the present chapter we address the question of how a realistic quantum memory affects the performance of the original compact continuous-variable entanglement distillation protocol discussed above. Note that the decoherence dynamics (loss) we are interested in does not alter the Gaussian character of the state [271], and can be considered as a Gaussian channel. The approach that we use here for incorporating the dissipation dynamics is based on the so-called beam splitter model for losses. The latter considers a quantum memory as a set of beam splitters, with a lost reflected mode. The model is applicable in the Markovian limit, when the system dynamics is much slower than the one of the environment. Note that the dissipation drives the initial pure two-mode squeezed state to a mixed one. For quantifying entanglement of such states we use the logarithmic negativity [41, 42].

We show that the dissipation can modify strongly the preparatory "malting" step of the protocol [158], which consists in de-Gaussifying the initial two-mode squeezed state (distributed over two quantum memories), by retrieving a single photon from the quantum state stored in a memory. The spin-wave-type excitations of the quantum memories we are considering are similar to optical phonons in condensed matter systems, and so we refer to this operation as "phonon subtraction". Particularly, we point out that one may not find entanglement increase after de-Gaussifying the initial state, which is not the case in a perfect memory. This effect puts additional constraints on the memory time-bandwidth product and the subtraction probability, which, however, do not complicate much the experimental realization of the protocol. We also show that high values of the average entanglement of the output state can be achieved by increasing the subtraction strength.

4.2 A beam splitter model for losses in a quantum memory

Consider an arbitrary two-mode density matrix, represented in the number basis $|n\rangle$ by coefficients $p_{n,m,k,l}$ (subscripts A and B differentiate the modes):

$$\rho = \sum_{n,m,k,l=0}^{\infty} p_{n,m,k,l} |n\rangle_A \otimes |m\rangle_B \langle k|_A \otimes \langle l|_B. \tag{4.1}$$

We are interested in modeling losses of such a state, when the latter is distributed over two quantum memories. For that we use a beam splitter model for losses, i.e., we consider the quantum memory as a set of beam splitters, with the state ρ and a two-mode vacuum $|0\rangle_A \otimes |0\rangle_B$ as inputs (Fig. 4.1). In the present model the reflected mode accounts for the loss.

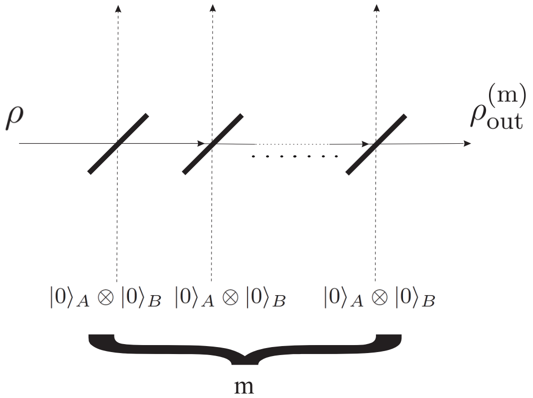

Figure 4.1: The beam splitter model for losses (schematically). Decoherence within a quantum memory is modeled as a set of m beam splitters with a state ρ and a two-mode vacuum $|0\rangle_A \otimes |0\rangle_B$ as inputs.

A beam splitter has two input modes a_1 and a_2, and implements the transformation

$$\begin{pmatrix} a_1' \\ a_2' \end{pmatrix} = U \begin{pmatrix} a_1 \\ a_2 \end{pmatrix} \tag{4.2}$$

with

$$U = \begin{pmatrix} t & r \\ -r & t \end{pmatrix}, \tag{4.3}$$

where t^2 and r^2 are, respectively, the transmissivity and reflectivity: $t^2 + r^2 = 1$ (hereafter we refer to t and r as simply the transmissivity and reflectivity). Thus, mixing a two-mode vacuum $|0\rangle_A \otimes |0\rangle_B$ and the state (4.1) on a beam splitter, one obtains the output state

$$\rho_{\mathrm{out}}' = \sum_{n,m,k,l=0}^{\infty} \sum_{K=0}^{n,m,k,l} p_{n,m,k,l} A_{n,k_1}(t) A_{m,k_2}(t) A_{k,k_3}(t) A_{l,k_4}(t) |n-k_1, k_1\rangle_A |m-k_2, k_2\rangle_B \times \langle k-k_3, k_3|_A \langle l-k_4, k_4|_B, \tag{4.4}$$

with $K = \{k_1, k_2, k_3, k_4\}$ representing the indices,

$$A_{qq'}(t) = \sqrt{\begin{pmatrix} q \\ q' \end{pmatrix}} t^{q-q'} r^{q'} \tag{4.5}$$

and $\left(\begin{array}{c} q \\ q' \end{array}\right)$ are the binomial coefficients. The next step in the beam splitter model for losses is the trace out operation over the reflected (lost) mode, which yields

$$\rho_{\text{out}}^{(1)} = \sum_{n,m,k,l=0}^{\infty} \sum_{k_1=0}^{\min(n,k)} \sum_{k_2=0}^{\min(m,l)} p_{n,m,k,l} A_{n,k_1}(t) A_{m,k_2}(t) A_{k,k_1}(t) A_{l,k_2}(t) |n-k_1\rangle_A |m-k_2\rangle_B \times \langle k-k_1|_A \langle l-k_2|_B. \tag{4.6}$$

Hereafter, the superscript of the output state labels the number of loss events (beam splitters) that the initial state has undergone. Note that photons may or may not be lost at each loss event, but purity of the state decreases after each loss event. The general expression (4.6) can be used iteratively, considering the output state of the i^{th} beam splitter as an input for the $(i+1)^{\text{th}}$ one. Note, that the transmissivity t can be also related to the time-bandwidth product τ of a quantum memory: $\tau = 1/(1-t^2)$. Below we use the latter quantity, since it is a more convenient parameter for characterizing a memory: it determines the number of iterations that can be executed within the coherence lifetime of the memory.

In the present work, we are mainly interested in a two-mode squeezed state $\rho_{\text{TMSS}} = |\Psi_{\text{TMSS}}\rangle\langle\Psi_{\text{TMSS}}|$

$$|\Psi_{\text{TMSS}}\rangle = \sqrt{1-\lambda^2} \sum_{n=0}^{\infty} \lambda^n |n\rangle_A |n\rangle_B, \tag{4.7}$$

where λ is the squeezing parameter (for the compact distillery protocol [158], $|n\rangle$ corresponds to the number of phonons in the matter mode). Using Eq. (4.6), after one loss event for this particular input state we obtain

$$\rho_{\text{out}}^{(1)} = (1-\lambda^2) \sum_{n,n'=0}^{\infty} \lambda^{n+n'} \sum_{k,k'=0}^{\mathcal{N}} A_{n,k}(t) A_{n,k'}(t) A_{n',k}(t) A_{n',k'}(t) |n-k\rangle_A |n-k'\rangle_B \langle n'-k|_A \langle n'-k'|_B, \tag{4.8}$$

where $\mathcal{N} = \min(n, n')$. After m loss events, a two-mode squeezed state is mapped into

$$
\begin{aligned}
\rho_{\text{out}}^{(\text{m})} \quad &= (1-\lambda^2)\sum_{n,n'=0}^{\infty}\lambda^{n+n'}\sum_{k_1,k_1'=0}^{\min(n,n')}\sum_{k_2,k_2'=0}^{\min(n-k_1,n'-k_1)}\ldots\sum_{k_m,k_m'=0}^{\min(n-k_1-k_2-\ldots-k_{m-1},n'-k_1-k_2-\ldots-k_{m-1})}\\
&A_{n,k_1}(t)A_{n,k_1'}(t)A_{n',k_1}(t)A_{n',k_1'}(t)A_{n-k_1,k_2}(t)A_{n-k_1',k_2'}(t)A_{n'-k_1,k_2}(t)A_{n'-k_1',k_2'}(t)\\
&\times\, A_{n-k_1-k_2-\ldots-k_{m-1},k_m}(t)A_{n-k_1'-k_2'-\ldots-k_{m-1}',k_m'}(t)A_{n'-k_1-k_2-\ldots-k_{m-1},k_m}(t) \qquad (4.9)\\
&\times A_{n'-k_1'-k_2'-\ldots-k_{m-1}',k_m'}(t)|n-k_1-\ldots-k_m\rangle_A|n-k_1'-\ldots-k_m'\rangle_B\\
&\langle n'-k_1-\ldots-k_m|_A\langle n'-k_1'-\ldots-k_m'|_B.
\end{aligned}
$$

Although, this formula is analytical, it is not convenient for quantitative analyzes. Thus in what follows, we use the recursive approach, based on Eq. (4.6).

4.3 Malting step with losses

In this section we show how the losses affect the preparatory (malting) step of the original compact distillery protocol, described in Ref. [158]. The malting procedure results in a non-Gaussian output state, prepared from an initial two-mode squeezed state (4.7). Namely, the latter undergoes a non-Gaussian operation of a phonon subtraction from each of the modes, which can be achieved by sending in weak control pulses and detecting the emission of a photon at the output. The quantum memories we are considering are based on Raman interactions in atomic ensembles, where light can be stored into a material excitation (phonon mode) and retrieved from it on-demand, by the application of ancillary "control pulses" that drive the Raman scattering. There is a formal correspondence between the Raman interaction, which couples optical and material modes, and a standard beam splitter interaction between two optical modes [272]. Making use of this analogy, we are able to implement phonon subtraction by applying a weak control pulse to the memory, which partially retrieves the stored excitation onto a photon detector. This is equivalent to placing a highly transmissive beam splitter in the path of an all-optical state, and reflecting a small portion of it towards a detector, which is the standard procedure for photon subtraction [264].

Here we assume that a discrete loss event occurs between two consecutive phonon subtraction attempts. More precisely, malting starts with one loss event, followed by an attempt of a phonon subtraction on both arms. If the attempt was not successful on either of the modes (i.e. if a vacuum detection took place on both arms), another loss event happens, followed by a consecutive phonon subtraction attempt, and so on. When one detects a phonon at one of the arms, it is left to undergo subsequent loss events, with loss and vacuum detection taking place on the other mode, until a successful phonon retrieval [Fig. 4.2(a)]. The non-Gaussian output state is considered to be ready when phonons have been subtracted from both modes.

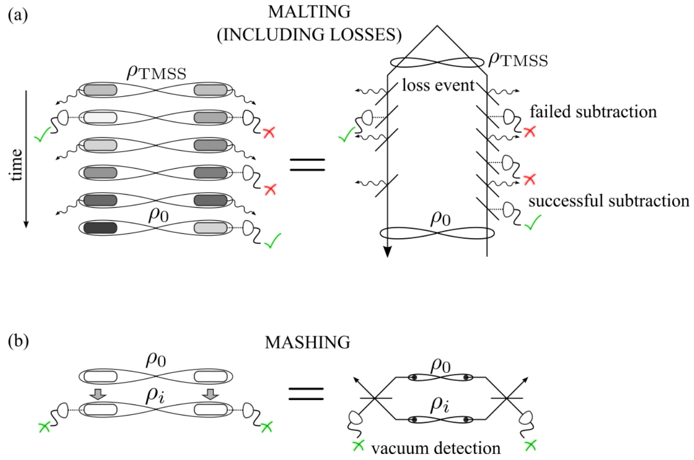

Figure 4.2: (a) Malting step with losses. The initial two-mode squeezed state $\rho_{\rm TMSS}$ undergoes phonon subtraction attempts (achieved by sending in weak control pulses, which implement the beam splitter interaction, and by detecting the emission of a photon at the output), with interstitial loss events (modeled by a beam splitter model for losses). The state is considered to be ready (malted), when phonons have been retrieved from both modes. The left hand side shows the scheme with memories, and the right hand side shows the all-optical analog. (b) Mashing step. At the $i^{\rm th}$ iteration of the mashing step a state ρ_0 is mapped into the memories containing the state ρ_i, with vacuum detected in the transmitted modes. This is equivalent to the all-optical scheme shown on the right, where the states are interfered on beam splitters with subsequent vacuum detection.

If a given state (4.1) undergoes a detection of q phonons by an ideal number-resolving detector, the unnormalized output state reads

$$\begin{aligned}\rho'_{\rm sub} &= \sum_{n,m,k,l=0}^{\infty} A_{n,q}(t_s)A_{m,q}(t_s)A_{k,q}(t_s)A_{l,q}(t_s)\\ &\quad\times|n-q\rangle_A|m-q\rangle_B\langle k-q|_A\langle l-q|_B,\end{aligned}\tag{4.10}$$

where t_s stands for the transmissivity of the subtraction beam splitter interaction. The trace of $\rho'_{\rm sub}$ gives the probability of a detection of q phonons, and the normalized output state reads $\rho_{\rm sub} = \rho'_{\rm sub}/{\rm Tr}\,(\rho'_{\rm sub})$. In the present protocol we deal only with vacuum detection

($q = 0$) and a single phonon subtraction ($q = 1$).

For quantifying entanglement we use the logarithmic negativity, defined as

$$N(\rho) = \log_2 \left|\left|\rho^{T_A}\right|\right|, \tag{4.11}$$

where $\left|\left|\rho^{T_A}\right|\right|$ is the trace norm of the partial transposed ρ^{T_A} of a bipartite density matrix ρ [41, 42].

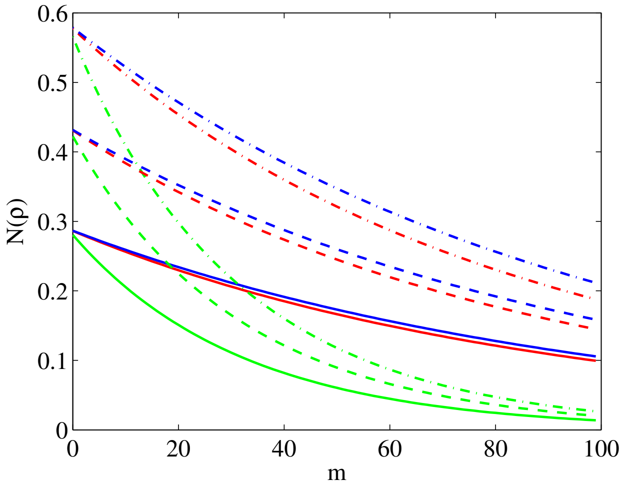

Figure 4.3: Logarithmic negativity $N(\rho)$ of a two-mode squeezed state (4.7), versus discrete time step (memory clock-cycle) m, for $\lambda = 0.1$ (full curves), $\lambda = 0.15$ (dashed curves) and $\lambda = 0.2$ (dot-dashed curves). The state undergoes m vacuum detections with $\tau = 1/(1-t^2) = 100$, $t_s = t$ (upper curve of each block); the state undergoes m losses with $\tau = 1/(1-t^2) = 100$, $t_s = t$ (middle curve of each block); the state undergoes m losses and vacuum detections with $\tau = 1/(1-t^2) = 100$, $t_s = 0.99$ (lower curve of each block).

In Fig. 4.3 we show how the entanglement [quantified by $N(\rho)$] of a two-mode squeezed state (4.7) evolves in a discrete time scale if either vacuum detection or loss or both occur. The curves start from a point corresponding to the amount of entanglement of a two-mode squeezed state: $N(\rho) = \log_2 \frac{1+\lambda}{1-\lambda}$. As expected, in all of these three cases the entanglement decreases exponentially versus time. However, for equal values of t and t_s the loss affects the rate of decrease more than the vacuum detection. When combined together, these two effects bring about a steeper slope.

Note that in an ideal memory one finds an increase of entanglement even after a phonon subtraction on only one arm. However, as we show below, this is not the case if losses are taken into account. Figure 4.4 shows the evolution of entanglement versus the memory clock-cycle m. Although here we suppose that the phonon subtraction happens at a fixed step on each arm ($m_A = 15$, and $m_B = 20$), the picture remains qualitatively the same for any values of m_A and m_B.

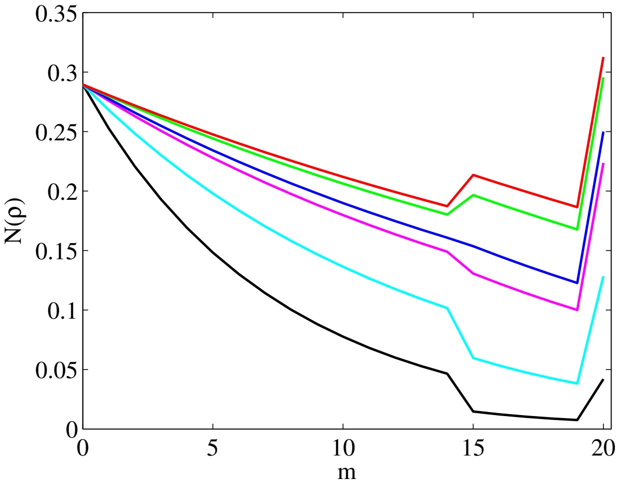

Figure 4.4: Logarithmic negativity $N(\rho)$ of a two-mode squeezed state (4.7), versus discrete time step (memory clock-cycle) m, for $\lambda = 0.1$, $t_s = 0.99$ and different values of $\tau = 1/(1-t^2)$: $\tau = 100, 80, 50, 40, 20, 10$ from the upper to the lower curve. The phonon subtraction occurs at $m_A = 15$ on the mode A, and at $m_B = 20$ on the mode B.

Additionally, as one finds here, the smaller τ is, the less benefit of entanglement increase we get. In other words, the decoherence damages the initial state, driving its properties away from that of a two-mode squeezed state. Furthermore, for extremely low values of the time-bandwidth product, one does not achieve any entanglement increase through a successful malting step. In this case the distillation attempt can be considered to be ineffective. In the next section we return to the question of the possible number of phonon subtraction attempts.

Obviously, the phonon subtraction is a probabilistic process. Thus, it is of interest to study the behavior of the probability P_{ij} of a phonon subtraction, depending on i and j, i.e., on the index number, at which a detection occurs on the arms A and B respectively. The success probability is given by the trace of the matrix ρ'_{sub} in Eq. (4.10), with $q = 1$. In Fig. 4.5 we show the matrix P_{ij}. It is symmetric, which confirms the symmetry of the distillation protocol with respect to the modes A and B. Secondly, the probability P_{ij} decreases exponentially with i and j. Thus, most probably the two-mode squeezed state is malted at the first attempt, which additionally guarantees the least amount of entanglement loss due to decoherence.

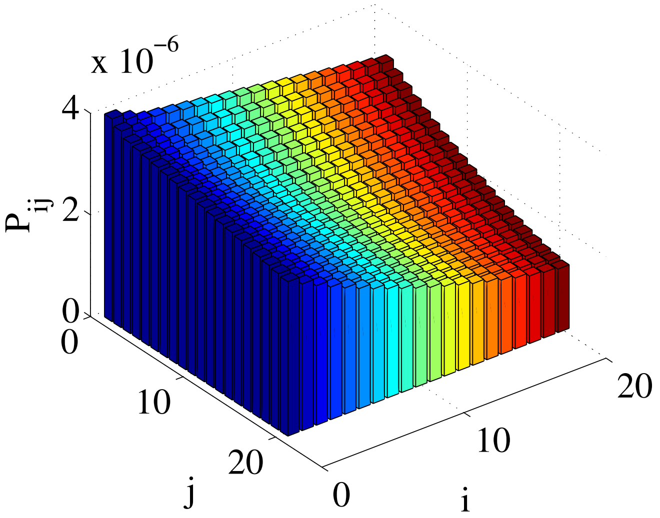

Figure 4.5: The matrix P_{ij} of probabilities of a phonon subtraction at i^{th} and j^{th} step on the first and second arms respectively. Here $\lambda = 0.1$, $\tau = 1/(1-t^2) = 100$ and $t_s = 0.99$ $(i, j = 1, ..., 20)$.

4.4 Mashing step and the full distillation protocol

After the initial two-mode squeezed state has been malted in two pairs of quantum memories, one proceeds to the iterative mashing step. The resource state obtained through malting is denoted here by ρ_0. Note that the Fock decomposition of the state ρ_0 retains its original Fock space structure in the ideal distillery protocol. However, when losses are taken into account, the Fock decomposition of ρ_0 is not similar to that of the two-mode squeezed state: the decoherence damages its original structure.

In brief, the mashing step involves the following operations. In the first step of its iteration, two copies of the state ρ_0 are combined on two 50/50 beam splitters. In the case that each party detects vacuum on one of the emerging modes from each beam splitter, the resultant state in the other two modes is ρ_1. Next, ρ_1 is interfered with a fresh copy of ρ_0 to produce ρ_2 upon a vacuum detection, and so on. At stage i of the protocol, we combine ρ_i with ρ_0 on beam splitters and detect vacuum, to produce the state ρ_{i+1} [Fig 4.2(b)]. This iterative procedure can be expressed as

$$\rho_{i+1} = \langle 0_{A_1}| \otimes \langle 0_{A_2}|(U_{A_1A_2} \otimes U_{B_1B_2})(\rho_i^{A_2B_2} \otimes \rho_0^{A_1B_1})(U_{A_1A_2}^\dagger \otimes U_{B_1B_2}^\dagger)|0_{A_1}\rangle \otimes |0_{A_2}\rangle, \quad (4.12)$$

where A_1, A_2, B_1 and B_2 distinguish the four memories used in the protocol and the matrices U correspond to 50/50 beam splitters.

In the above described scheme of the mashing step we do not take into account the decoherence affecting a state ρ_i, while it awaits new states to malt. Although being an approximation, this assumption keeps the calculations simple, still providing a good insight into the effects of losses of the protocol. Additionally, as shown below, a large part of the possible entanglement increase comes from the malting step. Thus one can consider the above simplification as a good starting point aimed towards the understanding of loss effects in the present distillation protocol.

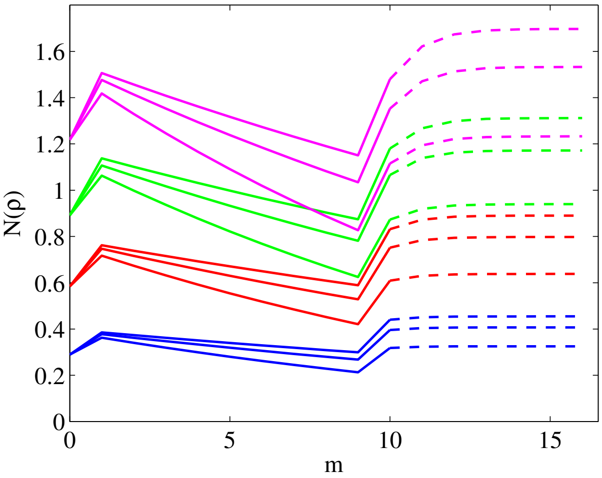

Figure 4.6: The negativity $N(\rho)$ versus the full distillation protocol clock-cycle number m for $\lambda = 0.1, 0.2, 0.3, 0.4$ from the lower to the upper block of three curves. Here, $\tau = 1/(1-t^2) = 100$ and $t_s = 0.99, 0.98, 0.96$ from the upper to the lower curve of each block of the same color. The phonon subtraction occurs at $m_A = 1$ and $m_B = 10$. The full curves correspond to the malting step, while the dashed ones stand for mashing.

In Fig. 4.6 we show how the full distillation protocol modifies the entanglement properties of an initial two-mode squeezed state. Firstly, we find that the above mapping, transforming ρ_i to ρ_{i+1}, converges to its fixed point after quite a small number of iterations. Secondly, the mashing step does not increase the entanglement of a malted state by very much for low values of the squeezing parameter. Meanwhile, its impact becomes significant for relatively high values of λ.

In Fig. 4.6 we have fixed the number of attempts after which a successful phonon subtraction occurs. However, as already mentioned in the previous section, a long storage in a lossy memory during the malting step can result in an absence of a positive entanglement gain. For moderate amount of losses in a memory, this corresponds to a relatively large number of unsuccessful subtraction attempts. It is of interest to consider the latter's threshold number, after which the protocol should be restarted. More precisely, we are interested in the critical value m_c of subtraction attempts, within which we must succeed if we are to have a gain in entanglement in the full distillation protocol. Here we propose two possible definitions of this quantity:

1. m_c is the critical number of simultaneous detection attempts on both arms
2. m_c is the critical number of subtraction attempts on one of the arms, when the index m_i $(i = A, B)$ of a successful attempt on the opposite arm is considered to be fixed.

Below we study the second option. Additionally, we assume that a successful phonon subtraction on one of the arms occurs at the first clock-cycle. The reason for this choice is that it leads to a maximal entanglement gain and has the highest probability. Note that this option is still symmetric, in a sense that the value of m_c does not depend on whether it is obtained at a fixed m_A or m_B.

Figure 4.7 shows how the above defined quantity m_c depends on the transmissivity t_s. We find that there exists a critical value t_s^c such, that if $t_s < t_s^c$, one does not have any increase of entanglement through the distillation protocol, even if the state was malted at the very first phonon subtraction attempt. Our calculations show that $t_s^c \approx 0.7$ for a wide range of parameters τ and λ. This condition puts a constraint on the experimental realization of the subtraction beam splitter interaction transmissivity t_s^2: it should be not less than $\sim 50\%$. On the other hand, for moderate values of t_s, the critical m_c properties of the protocol does not differ much with respect to changes in the time-bandwidth product τ. The difference becomes significant for values of t_s close to one. Note that the quantity m_c additionally

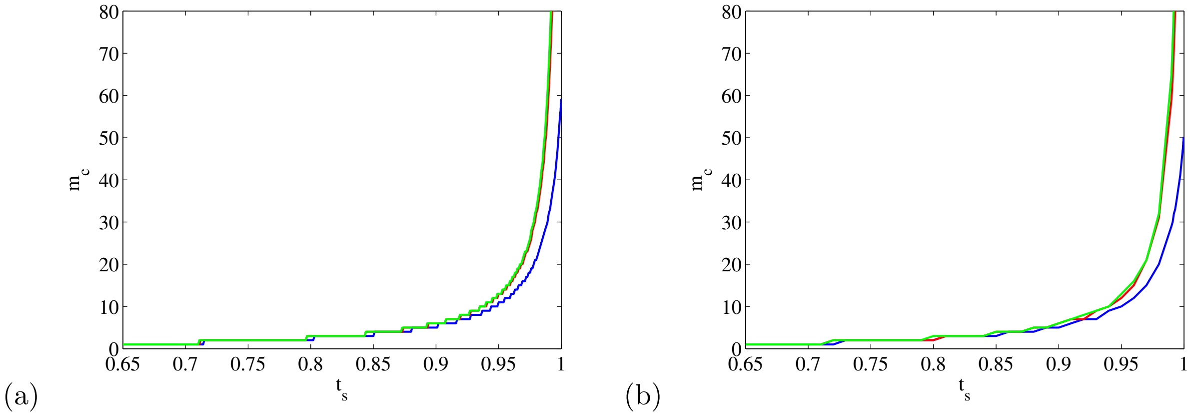

Figure 4.7: The critical number of phonon subtraction attempts m_c, versus transmissivity t_s for (a) $\lambda = 0.1$ and (b) $\lambda = 0.2$. A successful subtraction on the first arm is considered to occur at the first clock cycle. Here, $\tau = 1/(1-t^2) = 100$ (blue curve), 1000 (red curve), and 10000 (green curve).

contains the memory lifetime property. Namely, m_c does not increase infinitely: its upper bound value m_c^u is of the order of the time-bandwidth product τ ($m_c^u \sim \tau$).

As an additional measure of the efficiency of the protocol, which incorporates its probabilistic nature, we consider the average entanglement rate $\langle E \rangle$. We define it using the above discussed quantity m_c:

$$\langle E \rangle = \sum_{j=1}^{m_c} P^f_{m_A,j} N_f(\rho), \tag{4.13}$$

where $P^f_{i,j}$ corresponds to the joint probability of detecting a phonon at i^{th} and j^{th} attempts (on arms A and B respectively), with a consequent success probability of a vacuum detection in the mashing step. The quantity $N_f(\rho)$ stands for the negativity of the final state at the output of the distillery. Here we put an additional constraint on the phonon subtraction on arm A: we assume that it occurs at the first step, i.e., $m_A = 1$. Additionally, we truncate the sum in Eq. (4.13) to incorporate the fact that the protocol is restarted if one does not succeed to malt the initial two-mode squeezed state within m_c attempts.

Figure 4.8 shows that one can increase the average entanglement rate by increasing the subtraction beam splitter interaction transmissivity t_s. This is an obvious consequence of the fact that higher values of t_s allow a larger number of subtraction attempts, each of which contributes to the above defined average entanglement. Note, however, that the limit $t_s \to 1$ reduces the probability of a successful malting (time required to finish the malting step tends

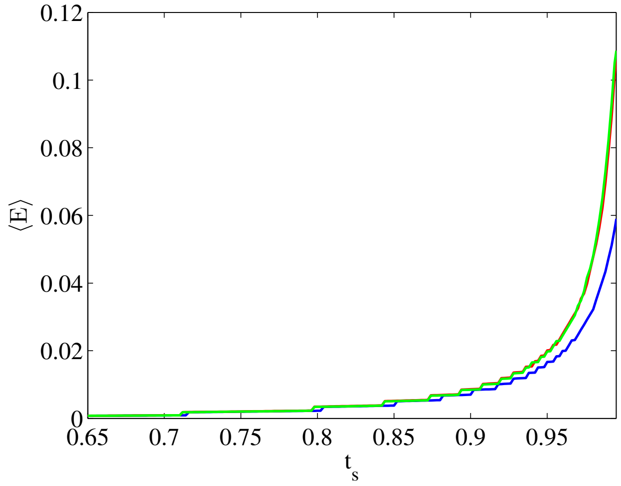

Figure 4.8: The average entanglement rate $\langle E \rangle$ defined in Eq. (4.13), versus transmissivity t_s, for $\lambda = 0.1$ and $m_A = 1$. Here, $\tau = 1/(1-t^2) = 100$ (blue curve), 1000 (red curve), and 10000 (green curve).

to infinity), which should result in a decrease of the average entanglement for values of t_s sufficiently close to one. One does not find this effect in the above figure, because of the assumption of a perfect mashing step. The additional entanglement gain due to the increase of t_s compensates the probability decrease.

4.4.1 Possible realization of the protocol within existing technologies

Here we briefly address the possible realization of the above discussed protocol within existing technologies. High efficiency photodetectors based on extremely sensitive phase transitions in superconducting materials are set to enable vacuum detection and photon number resolution [273, 274]. Several research groups are developing high efficiency quantum memories with long storage times [275–279], and the formal analogy between the interaction in a Raman memory and a beam splitter has been demonstrated [280, 281]. Here it was found that a wide range of beam splitting ratios can be readily achieved, so that the constraints derived above can be readily satisfied. Moreover, large values for the time-bandwidth product τ have been demonstrated, exceeding several thousands [282, 283]. We therefore expect that the entanglement distillery we have modeled here, including realistic losses, will be feasible in the near term.

4.5 Summary

1. We adopt the beam splitter model for losses to analyze the performance of a recent compact continuous-variable entanglement distillation protocol [158] implemented using realistic quantum memories. We show that the decoherence undergone by a two-mode squeezed state while stored in a quantum memory can strongly modify the results of the preparatory step of the protocol.
2. We find that the well-known method for locally increasing entanglement, phonon subtraction, may not result in entanglement gain when losses are taken into account. Thus, we investigate the critical number m_c of phonon subtraction attempts from the matter modes of the quantum memory. If the initial state is not de-Gaussified within m_c attempts, the protocol should be restarted to obtain any entanglement increase.
3. The condition $m_c > 1$ implies an additional constraint on the subtraction beam splitter interaction transmissivity, *viz.* it should be about 50% for a wide range of protocol parameters.
4. We consider the average entanglement rate, which takes into account both the unavoidable probabilistic nature of the protocol and its possible failure as a result of a large number of unsuccessful subtraction attempts. We find that a higher value of the average entanglement can be achieved by increasing the subtraction beam splitter interaction transmissivity.
5. We conclude that the compact distillation protocol with the practical constraints coming from realistic quantum memories allows a feasible experimental realization within existing technologies.

Conclusion

We conclude by summarizing our main results. The thesis is devoted to the analysis of problems of quantum information theory and their strong relation to frustrated spin systems and propagation of light in media. Our conclusions can be summarized as follows.

We considered the recently proposed Ising-Heisenberg model, for investigating entanglement features of some particular compounds, such as the natural mineral azurite ($Cu_3(CO_3)_2(OH)_2$) and a series of two-dimensional isostructural polymeric coordination compounds Cu_9X_2 $(cpa)_6 \cdot nH_2O$ (X = F, Cl, Br and cpa=carboxypentonic acid). The magnetic lattice of the first material is presented by a spin-1/2 diamond chain, while the second one is described by a triangulated Kagomé lattice. Although being an approximation of a pure Heisenberg exchange interaction, the Ising-Heisenberg model provides a satisfactory insight into the main features of these materials. Owing to the separable character of Ising-type interaction, we calculated entanglement (quantified by concurrence) for each of quantum clusters of the materials. The mean-field-like treatment based on the Gibbs-Bogoliubov inequality, which implicitly takes into account the interaction between quantum triangular clusters, was additionally applied to the triangulated Kagomé lattice. Here we revealed a strong relation between the thermodynamic and entanglement properties of the model. Particularly, we pointed out that the peaks of the magnetic susceptibility correspond to the values of parameters at which entanglement vanishes. Additionally the entanglement sudden-death temperature coincides with the second order phase transition point of the system. As for the diamond chain compound, we studied the ground-state structure of the system in a wide range of interaction strengths, revealing distinct regimes with qualitatively different quantum features. The results with respect to these problems were published in [159–162].

We have also considered another, purely classical limit of the Heiseneberg-type interaction, which results in classical spin models. The main motivation of exploring these models is their exact solvability in some particular cases. This leads to a possibility of deriving analytical expressions for thermodynamic quantities of interest. In particular, we looked into the phase structure of the Q-state Potts and the three-site interaction Ising models on recursive lattices, which are efficient in analysis of a number of magnetic systems. Note that the Bethe-Peierls approach, which approximates real lattices with hierarchical (recursive) ones, is more reliable in some cases than the above discussed mean-field treatment. The models were solved exactly by means of the recursion relation technique, reducing the thermodynamic properties of a model to the features of rational mappings. The phase structure of the above models was investigated by detecting bifurcation points of obtained rational mappings. A particular attention was devoted to the appearance of three-periodic window in chaotic region of both Potts and Ising models (with antiferromagnetic coupling between lattice nodes). We pointed out some intrinsic properties here, such as intermittency, occurring at both edges of the window and a finite number of periodic cycles (modulated phases), confined inside the window. The corresponding results are presented in [163–166].

Finally, we addressed to systems of interacting atoms and fields, which are also at the heart of quantum information processing. Particularly, we considered the Dicke model, for modeling the interaction of three trapped atoms in a cavity, interacting by means of effective coupling, mediated by the radiation field (the dispersive limit). We pointed out the strong relation of the model to the problems of frustrated magnetism, and applied similar tools for investigation of entanglement and thermodynamic properties of the system. Meanwhile, a crucial difference of the present system is the tunability of the coupling strength, which is rather complicated in the case of solids. Another important remark here concerns the effect of the vacuum induced Stark shift, which naturally arises in the problem: it turns out that this term changes the physical picture drastically.

We also presented a detailed study of population transfer process via b-STIRAP in a medium of three-level Λ-atoms with unequal oscillator strengths of corresponding atomic transitions. The propagation equations describing the dynamics of the process were derived and approximate analytical solutions were obtained. We showed that the population transfer efficiency is sensitive to the ratio of the oscillator strengths, $q = q_p/q_s$, and can be increased by a proper choice of this parameter. In particular, we find that the transfer efficiency is severely affected in case of $q > 1$ and rapidly decreases with propagation length, while in case of $q \leqslant 1$ propagating pulses maintain their capacity to produce a complete population transfer over larger propagation lengths. Additionally, we pointed out that the transfer can occur superluminally. The conditions restricting the propagation length at which a complete population transfer via b-STIRAP in a medium occurs were also derived. The details on these problems can be found in Refs. [167–169].

In addition, we considered another problem, closely related to the issues of quantum information processing and communication: the problem of entanglement distillation in quantum memories. We modeled the dissipations that a two-mode squeezed state (the initial entanglement resource) undergoes while stored in a memory, and showed that losses affect much the original protocol. Particularly, the preparatory step, aimed towards the de-Gaussification of the initial two-mode squeezed state, may not result in entanglement increase, although being a well-known method for locally increasing entanglement in a perfect memory. Thus we analyzed the constraints on the parameters of the protocol, within which one still gets an entanglement gain, and showed that the additional restrictions still allow experimental realization of the discussed scheme. The corresponding results are presented in Ref. [170].

The main results of the thesis were reported at the following conferences: 39*th* Conference of the Middle European Cooperation in Statistical Physics - MECO39 (Coventry, UK, 2014) [284], IOTA Workshop on Cold Molecular Ions (Arosa, Switzerland, 2013) [285], Control of Quantum Dynamics of Atoms, Molecules and Ensembles by Light workshop - CAMEL9 (Nessebar, Bulgaria, 2013) [286], Les 14èmes Journées de l'Ecole Doctorale Carnot Pasteur (Dijon, France, 2013) [287], 38*th* Conference of the Middle European Cooperation in Statistical Physics - MECO38 (ICTP, Trieste, Italy, 2013) [288], Laser Physics (Ashtarak, Armenia, 2011, 2012 & 2013) [289–291], The 7*th* International Conference Quantum Theory and Symmetries (Prague, Czech Republic, 2011) [292], The 19*th* International Colloquium on Integrable Systems and Quantum symmetries (Prague, Czech Republic, 2010) [293], Workshop on Principles and Design of Strongly Correlated Electronic Systems (ICTP, Miramare-Trieste, Italy, 2010) [294], Pseudochaos and Stable-Chaos in Statistical Mechanics and Quantum Physics (ICTP, Miramare - Trieste, Italy, 2009) [295]. Some parts of the work were discussed at seminars of the Institute for Physical Research of Armenian NAS and A. I. Alikhanyan National Science Laboratory, Armenia; Laboratoire Interdisciplinaire Carnot de Bourgogne, Université de Bourgogne, France; Oxford University and Coventry University, UK; University of Florence, Italy.

Bibliography

[1] L. Amico, R. Fazio, A. Osterloh, V. Vedral, "Entanglement in many-body systems", Rev. Mod. Phys **80**, 517 (2008).

[2] O. Gühne, G. Tóth, "Entanglement detection", Phys. Reports **474**, 1 (2009).

[3] C. H. Bennett, D. P. DiVincenzo, J. A. Smolin, W. K. Wootters, "Mixed-state entanglement and quantum error correction", Phys. Rev. A **54**, 3824 (1996).

[4] C. H. Bennett, G. Brassard, S. Popescu, B. Schumacher, J. A. Smolin, and W. K. Wootters, "Purification of noisy entanglement and faithful teleportation via noisy channels", Phys. Rev. Lett, **76**, 722 (1996).

[5] A. K. Ekert, "Beating the code breakers", Nature (London) **358**, 14 (1992).

[6] C. H. Bennett, G. Brassard, C. Crépeau, R. Jozsa, A. Peres, and W. K. Wootters, "Teleporting an unknown quantum state via dual classical and Einstein-Podolsky-Rosen channels", Phys. Rev. Lett. **70**, 1895 (1993).

[7] D. Bouwmeester, J. W. Pan, K. Mattle, M. Eibl, H. Weinfurter, and A. Zeilinger, "Experimental quantum teleportation", Nature (London) **390**, 575 (1997).

[8] J. Cho and H.-W. Lee, "Generation of atomic cluster states through the cavity input-output process", Phys. Rev. Lett. **95**, 160501 (2005).

[9] X.-M. Jin, J.-G. Ren, B. Yang, Z.-H. Yi, F. Zhou, X.-F. Xu, S.-K. Wang, D. Yang, Y.-F. Hu, S. Jiang, T. Yang, H. Yin, K. Chen, C.-Z.Peng and J.-W. Pan, "Experimental free-space quantum teleportation", Nature Photonics **4**, 376 (2010).

[10] M. Baur, A. Fedorov, L. Steffen, S. Filipp, M. P. da Silva, and A. Wallraff, "Benchmarking a quantum teleportation protocol in superconducting circuits using tomography and an entanglement witness", Phys. Rev. Lett. **108**, 040502 (2012).

[11] G. Björk, A. Laghaout, and U. L. Andersen, "Deterministic teleportation using single-photon entanglement as a resource", Phys. Rev. A **85**, 022316 (2012).

[12] P. Kok, W. J. Munro, K. Nemoto, T.C. Ralph, J. P. Dowling, G. J. Milburn, "Linear optical quantum computing with photonic qubits", Rev. Mod. Phys. **79**, 135 (2007).

[13] J. Kim, J.-S. Lee, and S. Lee, C. Cheong, "Implementation of the refined Deutsch-Jozsa algorithm on a three-bit NMR quantum computer", Phys. Rev. A **62**, 022312 (2000).

[14] A. Brodutch and D. R. Terno, "Entanglement, discord, and the power of quantum computation", Phys. Rev. A **83**, 010301(R) (2011).

[15] V. Vedral and E. Kashefi, "Uniqueness of the entanglement measure for bipartite pure states and thermodynamics", Phys. Rev. Lett. **89**, 037903 (2002).

[16] Sasaki *et al.*, "Field test of quantum key distribution in the Tokyo QKD Network", Optics Express **19**, 10387 (2011).

[17] A. Avella, G. Brida, I. P. Degiovanni, M. Genovese, M. Gramegna, and P. Traina, "Experimental quantum-cryptography scheme based on orthogonal states", Phys. Rev. A **82**, 062309 (2010).

[18] E. Schrodinger, "Discussion of probability relations between separated systems", Proc. Cambridge Phil. Soc. **31**, 555 (1935).

[19] M. C. Arnesen, S. Bose, and V. Vedral, "Natural thermal and magnetic entanglement in the 1D Heisenberg model", Phys. Rev. Lett. **87**, 017901 (2001).

[20] D. Gunlycke, V. M. Kendon, V. Vedral, and S. Bose, "Thermal concurrence mixing in a one-dimensional Ising model", Phys. Rev. A **64**, 042302 (2001).

[21] X. Wang, "Entanglement in the quantum Heisenberg XY model", Phys. Rev. A **64**, 012313 (2001).

[22] X. Wang, "Effects of anisotropy on thermal entanglement", Phys. Lett. A **281**, 101 (2001).

[23] J. Vidal, G. Palacios, and R. Mosseri, "Entanglement in a second order quantum phase transition", Phys. Rev. A **69**, 022107 (2004).

[24] D. Larsson and H. Johannesson, "Entanglement scaling in the one-dimensional Hubbard model at criticality", Phys. Rev. Lett. **95**, 196406 (2005).

[25] V. Alba, L. Tagliacozzo, and P. Calabrese, "Entanglement entropy of two disjoint blocks in critical Ising models", Phys. Rev. B **81**, 060411(R) (2010).

[26] V. S. Abgaryan, N. S. Ananikian, L. N. Ananikyan and A. N. Kocharian, " Phase transitions and entanglement properties in spin-1 Heisenberg clusters with single-ion anisotropy", Phys. Scr. **83**, 055702 (2011).

[27] N. Ananikian, L. Ananikyan, H. Lazaryan, "Magnetic properties and concurrence for fluid ^{3}He on kagome lattice", Physics of Atomic Nuclei **75**, 1250 (2012).

[28] N. Ananikian, H. Lazaryan, M. Nalbandyan, "Magnetic and quantum entanglement properties of the distorted diamond chain model for azurite", Eur. Phys. J. B **85**, 223 (2012).

[29] M. Wieśniak, V. Vedral and Č. Brukner, "Magnetic susceptibility as a macroscopic entanglement witness", New J. Phys. **7**, 258 (2005).

[30] A. M. Souza, M. S. Reis, D. O. Soares-Pinto, I. S. Oliveira, and R. S. Sarthour, "Experimental determination of thermal entanglement in spin clusters using magnetic susceptibility measurements", Phys. Rev. B **77**, 104402 (2008).

[31] A. L. Lima Sharma and A. M. Gomes, "Experimental investigation of the entanglement in the magnetization of the layered $CaMn_2Sb_2$ compound", Europhys. Lett. **84**, 60003 (2008).

[32] T. G. Rappoport, L. Ghivelder, J. C. Fernandes, R. B. Guimarães, and M. A. Continentino "Experimental observation of quantum entanglement in low-dimensional spin systems", Phys. Rev. B **75**, 054422 (2007).

[33] D. O. Soares-Pinto, A. M. Souza, R. S. Sarthour, I. S. Oliveira, M. S. Reis, P. Brandão, J. Rocha and A. M. dos Santos, "Entanglement temperature in molecular magnets composed of S-spin dimers", Europhys. Lett. **87**, 40008 (2009).

[34] A. M. Souza, D. O. Soares-Pinto, R. S. Sarthour, I. S. Oliveira, M. S. Reis, P. Brandão, and A. M. dos Santos, "Entanglement and Bells inequality violation above room temperature in metal carboxylates", Phys. Rev. B **79**, 054408 (2009).

[35] K. C. Lee, M. R. Sprague, B. J. Sussman, J. Nunn, N. K. Langford, X.-M. Jin, T. Champion, P. Michelberger, K. F. Reim, D. England, D. Jaksch, I. A. Walmsley "Entangling macroscopic diamonds at room temperature", Science **334**, 1253 (2011).

[36] R. Jozsa, "Fidelity for mixed quantum states", J. Mod. Opt. **41**, 2315 (1994).

[37] K. Mattle, H. Weinfurter, P. G. Kwiat, and A. Zeilinger, "Dense coding in experimental quantum communication", Phys. Rev. Lett. **76**, 4656 (1996).

[38] C. H. Bennett, H. J. Bernstein, S. Popescu, and B. Schumacher, "Concentrating partial entanglement by local operations", Phys. Rev. A **53**, 2046 (1996).

[39] S. Hill and W. K. Wootters, "Entanglement of a pair of quantum bits", Phys. Rev. Lett. **78**, 5022 (1997).

[40] W. K. Wootters, "Entanglement of formation of an arbitrary state of two qubits", Phys. Rev. Lett. **80**, 2245 (1998).

[41] M. B. Plenio, "Logarithmic negativity: a full entanglement monotone that is not convex", Phys. Rev. Lett. **95**, 090503 (2005).

[42] G. Vidal, R. F. Werner, "Computable measure of entanglement", Phys. Rev. A **65**, 032314 (2002).

[43] A. Peres, "Separability criterion for density matrices", Phys. Rev. Lett. **77**, 1413 (1996).

[44] D. E. Liu, S. Chandrasekharan, and H. U. Baranger, "Quantum phase transition and dynamically enhanced symmetry in quadruple quantum dot system", Phys. Rev. Lett. **105**, 256801 (2010).

[45] J. R. de Sousa and N. S. Branco, ”Two-dimensional quantum spin-1/2 Heisenberg model with competing interactions”, Phys. Rev. B **72**, 134421 (2005).

[46] E. Y. Vedmedenko, L. Udvardi, P. Weinberger, R. Wiesendanger, ”Chiral magnetic ordering in two-dimensional ferromagnets with competing Dzyaloshinsky-Moriya interactions”, Phys. Rev. B **75**, 104431 (2007).

[47] H. T. Diep (ed.), *Frustrated Spin Sysytems* (World Scientific, Singapore, 2004).

[48] J. S. Gardner, M. J. P. Gingras, J. E. Greedan, ”Magnetic pyrochlore oxides”, Rev. Mod. Phys **82**, 53 (2010).

[49] S.-H. Lee, H. Kikuchi, Y. Qiu, B. Lake, Q. Huang, K. Habicht, and K. Kiefer, ”Quantum-spin-liquid states in the two-dimensional kagome antiferromagnets $Zn_xCu_{4-x}(OD)_6Cl_2$”, Nature Materials **6**, 853 (2007).

[50] D. Grohol, K. Matan, J. H. Cho, S.-H. Lee, J. W. Lynn, D. G. Nocera, and Y. S. Lee, ”Spin chirality on a two-dimensional frustrated lattice”, Nature Materials **4**, 323 (2005).

[51] M. B. Stone, I. Zaliznyak, D. H. Reich, C. Broholm, ”Frustration-induced two-dimensional quantum disordered phase in piperazinium hexachlorodicuprate”, Phys. Rev. B **64**, 144405 (2001).

[52] E. Wawrzyńska, R. Coldea, E. M. Wheeler, T. Sörgel, M. Jansen, R. M. Ibberson, P. G. Radaelli, and M. M. Koza, ”Charge disproportionation and collinear magnetic order in the frustrated triangular antiferromagnet $AgNiO_2$”, Phys. Rev. B **77**, 094439 (2008).

[53] M. E. Zhitomirsky, A. Honecker, O. A.Petrenko, ”Field induced ordering in highly frustrated antiferromagnets”, Phys. Rev. Lett. **85**, 3269 (2000).

[54] S. Lee and K.-C. Lee, ”Phase transitions in the fully frustrated triangular XY model”, Phys. Rev. B **57**, 8472 (1998).

[55] G.-W. Chern, N. Perkins, and G. I. Japaridze, ”Quantum criticality of vanadium chains with strong relativistic spin-orbit interaction”, Phys. Rev. B **82**, 172408 (2010).

[56] T. Vekua, G. I. Japaridze, and H.-J. Mikeska, "Magnetic-field-induced phase transitions in spin ladders with ferromagnetic legs", Phys. Rev. B **70**, 014425 (2004).

[57] L. Craco, P. Lombardo, R. Hayn, G. I. Japaridze, and E. Müller-Hartmann, "Electronic phase transitions in the half-filled ionic Hubbard model", Phys. Rev. B **78**, 075121 (2008).

[58] H. M. Babujian, "Exact solution of the isotropic Heisenberg chain with arbitrary spins: thermodynamics of the model", Nucl. Phys. B **215**, 317 (1982).

[59] H. M. Babujian, "Exact solution of the one-dimensional isotropic Heisenberg chain with arbitrary spins S", Phys. Lett A **90**, 479 (1982).

[60] L. A. Takhtajan, "The picture of low-lying excitations in the isotropic Heisenberg chain of arbitrary spins", Phys. Lett. A **87**, 479 (1982).

[61] L. Čanova, J. Strečka and T. Lučivjanský, "Exact solution of the mixed spin-1/2 and spin-S Ising-Heisenberg diamond chain", Condens. Matter Phys. **12**, 353 (2009).

[62] L. Čanova, J. Strečka, M. Jaščur, "Geometric frustration in the class of exactly solvable Ising-Heisenberg diamond chains", J. Phys.: Condens. Matter **18**, 4967 (2006).

[63] M. Jaščur, J. Strečka, "Spin frustration in an exactly solvable Ising-Heisenberg diamond chain", J. Magn. Magn. Mater. **272**, 984 (2004).

[64] B. M. Lisnii, "Spin-1/2 asymmetric diamond Ising-Heisenberg chain", Ukr. J. Phys. **56**, 1237 (2011).

[65] D. Antonosyan, S. Bellucci, V. Ohanyan, "Exactly solvable Ising-Heisenberg chain with triangular XXZ-Heisenberg plaquettes", Phys. Rev. B **79**, 014432 (2009).

[66] O. Rojas, J. S. Valverde S. M. de Sousa, "Generalized transformation for decorated spin models", Physica A **388**, 1419 (2009).

[67] J. S. Valverde, O. Rojas, S. M. de Sousa, "Phase diagram of the asymmetric tetrahedral IsingHeisenberg chain", J. Phys.: Condens. Matter **20**, 345208 (2008).

[68] J. Strečka, "Magnetic properties of the geometrically frustrated spin-1/2 Heisenberg model on the triangulated Kagom lattice", J. Magn. Magn. Mater. **316**, e346 (2007).

[69] N. N. Bogoliubov, "On the theory of superfluidity", J. Phys. (USSR), **11** (1947).

[70] R. P. Feynman, "Slow Electrons in a Polar Crystal", Phys. Rev. **97**, 660 (1955).

[71] H. Kikuchi, Y. Fujii, M. Chiba, S. Mitsudo, T. Idehara, T. Tonegawa, K. Okamoto, T. Sakai, T. Kuwai, and H. Ohta, "Experimental observation of the 1/3 magnetization plateau in the diamond-chain compound $Cu_3(CO_3)_2(OH)_2$", Phys. Rev. Lett. **94**, 227201 (2005).

[72] R. E. Norman, N. J. Rose, and R. E. Stenkamp, "Crystal structure of a copper complex of 2-carboxypentonic acid; a decomposition product of dehydroascorbic acid", J. Chem. Soc.: Dalton Trans. **12**, 2905 (1987).

[73] R. E. Norman, and R. E. Stenkamp, "Structure of a copper(II) complex of 2-C-carboxypentonic acid (H_3cpa); $[Cu_9Br_2(cpa)_6]_{2-n} \cdot xH_2O$", Acta Cryst. **46**, 6 (1990).

[74] M. Gonzalez, F. Cervantes-Lee, L. W. Haar, "Structural and magnetic properties of the topologically novel 2-D material $Cu_9F_2cpa_6$: A triangulated Kagome - like hexagonal network of Cu(II) trimers interconnected by Cu(II) monomers", Mol. Cryst. Liq. Cryst. **233**, 317 (1993).

[75] S. Maruti and L. W. ter Haar, "Magnetic properties of the two-dimensional "triangles-in-triangles" Kagom lattice $Cu_9X_2(cpa)_6$ (X=F,Cl,Br)", J. Appl. Phys. **75**, 5949 (1994).

[76] S. Ateca, S. Maruti and L. W. ter Haar, "The two-dimensional triangles-in-triangles Kagom antiferromagnet $Cu_9X_2(cpa)_6$: a topological spin-glass?", J. Magn. Magn. Mater. **147**, 398 (1995).

[77] M. Roger, J. H. Hetherington, J. M. Delrieu, "Magnetism in solid ^{3}He", Rev. Mod. Phys. **55**, 1 (1983).

[78] T. A. Arakelyan, V. R. Ohanyan, L. N. Ananikian, N. S. Ananikian and M. Roger, "Multisite-interaction Ising model approach to the solid 3He system on a triangular lattice", Phys. Rev. B **67**, 024424 (2003).

[79] N. S. Ananikian, L .N. Ananikyan, R. Artuso, V. V. Hovhannisyan, "One-dimensional mapping, modulated phases and Lyapunov exponent for the antiferromagnetic Q-state Potts and multi-site exchange interaction Ising models", Physica D **239**, 1723 (2010).

[80] J. L. Monroe, "Potts models with period doubling cascades, chaos, etc", J. Phys. A: Math. Gen. **29**, 5421 (1996).

[81] R. F. S. Andrade and D. Cason, "Ising model with long range correlated disorder on hierarchical lattices", Phys. Rev. B **81**, 014204 (2010).

[82] T. Iharagi, A. Gendiar, H. Ueda, T. Nishino, "Phase transition of the Ising model on a hyperbolic lattice", J. Phys. Soc. Jpn. **79**, 104001 (2010).

[83] J. Gujrati, "Thermal and percolative transitions and the need for independent symmetry breakings in branched polymers on a Bethe lattice", J. Chem. Phys. **98**, 1613 (1993).

[84] J. Gujrati, "Bethe or Bethe-like lattice calculations are more reliable than conventional mean-field calculations", Phys. Rev. Lett. **74**, 809 (1995).

[85] V. V. Hovhannisyan and N. S. Ananikian, "Antiferromagnetic model and magnetization plateaus on the zigzag ladder with two- and three-site exchanges", Phys. Lett. A **372**, 3363 (2008).

[86] M. Udagawa, H. Ishizuka, and Y. Motome, "Quantum melting of charge ice and non-Fermi-liquid behavior: an exact solution for the extended Falicov-Kimball model in the ice-rule limit", Phys. Rev. Lett. **104**, 226405 (2010).

[87] N. S. Ananikian, S. K. Dallakian, N. Sh. Izmailian, and K.A. Oganessyan, "Strange attractors in an antiferromagnetic Ising model", Fractals **5**, 175 (1997).

[88] R. A. Zara, M. Pretti, "Exact solution of a RNA-like polymer model on the Husimi lattice", J. Chem. Phys. **127**, 184902 (2007).

[89] V. V. Cheianov, O. Syljuasen, B. L. Altshuler, and V. Falko, "Ordered states of adatoms on graphene", Phys. Rev. B **80**, 233409 (2009).

[90] A. Cruz *et. al*, "Spin glass phase in the four-state three-dimensional Potts model", Phys. Rev. B **79**, 184408 (2009).

[91] R. G. Ghulghazaryan, N. S. Ananikian, and P. M. A. Sloot, "Yang-Lee zeros of the Q-state Potts model on recursive lattices", Phys. Rev. E **66**, 046110 (2002).

[92] T. C. Lubensky and J. Isaacson, "Field theory for the statistics of branched polymers, gelation, and vulcanization", Phys. Rev. Lett. **41**, 829 (1978).

[93] C. B. Anfinsen, "Principles that govern the folding of protein chains", Science **181**, 223 (1973).

[94] C. M. Fortuin and P. W. Kasteleyn, "On the random-cluster model: I. Introduction and relation to other models", Physica **57**, 536 (1972).

[95] A. Aharony and P. Pfeuty, "Dilute spin glasses at zero temperature and the 1/2-state Potts model", J. Phys. C: Solid State Phys. **12**, L125 (1979).

[96] P. Whittle, "Polymer models and generalized Potts-Kasteleyn models", J. Stat. Phys. **75**, 1063 (1994).

[97] B. Duplantier, "Two-dimensional copolymers and exact conformal multifractality", Phys. Rev. Lett. **82**, 880 (1999).

[98] B. Yurke, A. N. Pargellis, S. N. Majumdar, and C. Sire, "Experimental measurement of the persistence exponent of the planar Ising model", Phys. Rev. E **56**, R40 (1997).

[99] B. Berche, P. E. Berche, C. Chatelain, W. Janke, "Random Ising model in three dimensions: theory, experiment and simulation - a difficult coexistence", Condens. Matter Phys. **8**, 47 (2005).

[100] M. Blume and V. J. Emery, R. B. Griffiths, "Ising model for the λ transition and phase separation in He^3-He^4 mixtures", Phys. Rev. A **4**, 1071 (1971).

[101] E. Stryjewski and N. Giordano, "Metamagnetism", Adv. Phys. **26**, 487 (1977).

[102] K. Furuya, M. C. Nemes, and G. Q. Pellegrino, "Quantum dynamical manifestation of chaotic behavior in the process of entanglement", Phys. Rev. Lett. **80**, 5524 (1998).

[103] R. M. Angelo, K. Furuya, M. C. Nemes, and G. Q. Pellegrino, "Recoherence in the entanglement dynamics and classical orbits in the N-atom Jaynes-Cummings model", Phys. Rev. A **64**, 043801 (2001).

[104] X.-W. Hou and B. Hu, "Decoherence, entanglement, and chaos in the Dicke model", Phys. Rev. A **69**, 042110 (2004).

[105] V. Bužek, M. Orszag, and M. Roško, "Instability and entanglement of the ground state of the Dicke model", Phys. Rev. Lett. **94**, 163601 (2005).

[106] T. Wilk, S. C. Webster, A. Kuhn, and G. Rempe, "Single-atom single-photon quantum interface", Science **317**, 488 (2007).

[107] J. Beugnon, M. P. A. Jones, J. Dingjan, B. Darquié, G. Messin, A. Browaeys, and P. Grangier, "Quantum interference between two single photons emitted by independently trapped atoms", Nature (London) **440**, 779 (2006).

[108] Y.-A. Chen, S. Chen, Z.-S. Yuan, B. Zhao, C.-S. Chuu, J. Schmiedmayer, and J.-W. Pan, "Memory-built-in quantum teleportation with photonic and atomic qubits", Nature Physics **4**, 103 (2008).

[109] X.-M. Lin, Z.-W. Zhou, M.-Y. Ye, Y.-F. Xiao, and G.-C. Guo, "One-step implementation of a multiqubit controlled-phase-flip gate", Phys. Rev. A **73**, 012323 (2006).

[110] Z. J. Deng, M. Feng, and K. L. Gao, "Preparation of entangled states of four remote atomic qubits in decoherence-free subspace", Phys. Rev. A **75**, 024302 (2007).

[111] G. S. Agarwal, R. R. Puri, and R. P. Singh, "Atomic Schrödinger cat states", Phys. Rev. A **56**, 2249 (1997).

[112] L. Jiang, J. M. Taylor, A. S. Sörensen, and M. D. Lukin, "Distributed quantum computation based-on small quantum registers", Phys. Rev. A **76**, 062323 (2007).

[113] L.-M. Duan and H. J. Kimble, "Efficient engineering of multiatom entanglement through single-photon detections", Phys. Rev. Lett. **90**, 253601 (2003).

[114] X. B. Zou, K. Pahlke, and W. Mathis, "Quantum entanglement of four distant atoms trapped in different optical cavities", Phys. Rev. A **69**, 052314 (2004).

[115] K. Hepp and E. H. Lieb, "Equilibrium statistical mechanics of matter interacting with the quantized radiation field", Phys. Rev. A **8**, 2517 (1973).

[116] Y. K. Wang and F. T. Hioe, "Phase transition in the Dicke model of superradiance", Phys. Rev. A **7**, 831 (1973).

[117] K. Baumann, C. Guerlin, F. Brennecke, and T. Esslinger, "Dicke quantum phase transition with a superfluid gas in an optical cavity", Nature (London) **464**, 1301 (2010).

[118] K. Baumann, R. Mottl, F. Brennecke, and T. Esslinger, "Exploring symmetry breaking at the Dicke quantum phase transition", Phys. Rev. Lett. **107**, 140402 (2011).

[119] V. M. Bastidas, C. Emary, B. Regler, and T. Brandes, "Nonequilibrium quantum phase transitions in the Dicke model", Phys. Rev. Lett. **108**, 043003 (2012).

[120] B. W. Shore and P. L. Knight, "The Jaynes-Cummings model", J. Mod. Opt. **40**, 1195 (1993).

[121] G. Ramon, C. Brif, and A. Mann, "Collective effects in the collapse-revival phenomenon and squeezing in the Dicke model", Phys. Rev. A **58**, 2506 (1998).

[122] P. Schleich, *Quantum Optics in Phase Space* (Wiley-VCH, Berlin, 2001).

[123] J. G. Peixoto de Faria and M. C. Nemes, "Dissipative dynamics of the Jaynes-Cummings model in the dispersive approximation: analytical results", Phys. Rev. A **59**, 3918 (1999).

[124] V. V. Dodonov, W. D. José and S. S. Mizrahi, "Dispersive limit of the dissipative Jaynes-Cummings model with a squeezed reservoir", J. Opt. B: Quantum Semiclass. Opt. **5**, S567 (2003).

[125] S.-B. Zheng, "One-step synthesis of multiatom Greenberger-Horne-Zeilinger states", Phys. Rev. Lett. **87**, 230404 (2001).

[126] S.-B. Zheng, and G.-C. Guo, "Teleportation of atomic states within cavities in thermal states", Phys. Rev. A **63**, 044302 (2001).

[127] S.-B. Zheng, and G.-C. Guo, "Efficient scheme for two-atom entanglement and quantum information processing in cavity QED", Phys. Rev. Lett. **85**, 2392 (2000).

[128] A. Imamoḡlu, D. D. Awschalom, G. Burkard, D. P. DiVincenzo, D. Loss, M. Sherwin, and A. Small, "Quantum information processing using quantum dot spins and cavity QED", Phys. Rev. Lett. **83**, 4204 (1999).

[129] C. A. Sackett, D. Kielpinski, B. E. King, C. Langer, V. Meyer, C. J. Myatt, M. Rowe, Q. A. Turchette, W. M. Itano, D. J. Wineland, and C. Monroe, "Experimental entanglement of four particles", Nature **404**, 256 (2000).

[130] B. W. Shore, *The Theory of Coherent Atomic Excitation* (John Wiley &. Sons, New York, 1990).

[131] M. Shapiro and P. Brumer, *Principles of the Quantum Control of Molecular Processes* (Wiley, New York, 2003).

[132] M. A. Nielson and I. L. Chuang, *Quantum Computation and Quantum Information* (Cambridge University Press, Cambridge, England, 2000).

[133] J. Oreg, F. T. Hioe, and J. H. Eberly, "Adiabatic following in multilevel systems", Phys. Rev. A **29**, 690 (1984).

[134] U. Gaubatz, P. Rudecki, S. Schiemann, and K. Bergmann, "Population transfer between molecular vibrational levels by stimulated Raman scattering with partially overlapping laser fields. A new concept and experimental results", J. Chem. Phys. **92** , 5363 (1990).

[135] N. V. Vitanov, T. Halfmann, B. W. Shore, and K. Bergmann, "Laser-induced population transfer by adiabatic passage techniques", Annu. Rev. Phys. Chem. **52,** 763 (2001).

[136] P. Král, I. Thanopulos, and M. Shapiro, "Colloquium: Coherently controlled adiabatic passage", Rev. Mod. Phys. **79**, 53 (2007).

[137] S. Guérin and H.R. Jauslin, "Control of quantum dynamics by laser pulses: adiabatic Floquet theory", Adv. Chem. Phys **125**, 147 (2003).

[138] H. Goto, K. Ichimura, "Population transfer via stimulated Raman adiabatic passage in a solid", Phys. Rev. A **74**, 053410 (2006).

[139] H. Goto, K. Ichimura, "Observation of coherent population transfer in a four-level tripod system with a rare-earth-metal-ion-doped crystal", Phys. Rev. A **75**, 033404 (2007).

[140] J. Klein, F. Beil, and T. Halfmann, "Robust Population Transfer by Stimulated Raman Adiabatic Passage in a Pr^{3+}:Y_2SiO_5 crystal", Phys. Rev. Lett. **99**, 113003 (2007).

[141] J. Klein, F. Beil, and T. Halfmann, "Experimental investigations of stimulated Raman adiabatic passage in a doped solid", Phys. Rev. A **78**, 033416 (2008).

[142] L. P. Yatsenko, S. Guérin, and H. R. Jauslin, "Topology of adiabatic passage", Phys. Rev. A **65**, 043407 (2002).

[143] M. Scala, B. Militello, A. Messina, and N. V. Vitanov, "Stimulated Raman adiabatic passage in an open quantum system: Master equation approach", Phys. Rev. A **81**, 053847 (2010).

[144] I. I. Boradjiev and N. V. Vitanov, "Transition time in the stimulated Raman adiabatic passage technique", Phys. Rev. A **82,** 043407 (2010).

[145] M. Scala, B. Militello, A. Messina, and N. V. Vitanov, "Stimulated Raman adiabatic passage in a Λ system in the presence of quantum noise", Phys. Rev. A **83,** 012101 (2011).

[146] V. Chaltykyan, E. Gazazyan, G. Grigoryan, D. Schraft, "Implementation of all optical Toffoli gate in Λ-systems", Journal of Contemporary Physics (NAS of Armenia), **37**, 328 (2012).

[147] F. Beil, T. Halfmann, F. Remacle, and R. D. Levine, "Logic operations in a doped solid driven by stimulated Raman adiabatic passage", Phys. Rev. A **83**, 033421 (2011).

[148] G. G. Grigoryan and Y. T. Pashayan, "Propagation of pulses in a three-level medium at exact two-photon resonance", Phys. Rev. A **64**, 013816 (2001).

[149] E. Mazets, B.G. Matisov, "Nonlinear wavefront sharpening in the adiabatic population transfer regime", Quantum Semiclass. Opt. **8**, 909 (1996).

[150] V. G. Arkhipkin, I. V. Timofeev, "Spatial evolution of short laser pulses under coherent population trapping", Phys. Rev A **64**, 053811 (2001).

[151] A. B. Matsko, Y. V. Rostovcev, O. Kocharovskaya, A. S. Zibrov, M. O. Scully, "Nonadiabatic approach to quantum optical information storage", Phys. Rev A **64**, 043809 (2001)

[152] M. Fleischhauer, A. Imamoglu, J.P. Marangos, "Electromagnetically induced transparency: optics in coherent media", Rev. Mod. Phys. **77**, 633 (2005).

[153] G. G. Grigoryan, G. V. Nikoghosyan, T. Halfmann, Y. T. Pashayan-Leroy, C. Leroy, S. Guérin, "Theory of the bright-state stimulated Raman adiabatic passage", Phys. Rev A **80**, 033402 (2009).

[154] Z. Zhao, J.-W. Pan, M.S. Zhan, "Practical scheme for entanglement concentration", Phys. Rev. A **64**, 014301 (2001).

[155] P.G. Kwiat, S. Barraza-Lopez, A. Stefanov, N. Gisin, "Experimental entanglement distillation and 'hidden' nonlocality", Nature (London) **409**, 1014 (2001).

[156] D. E. Browne, J. Eisert, S. Scheel, M. B. Plenio, "Driving non-Gaussian to Gaussian states with linear optics", Phys. Rev. A **67**, 062320 (2003).

[157] J. Eisert, D. E. Browne, S. Scheel, M. B. Plenio, "Distillation of continuous-variable entanglement with optical means", Ann. Phys. (N.Y.) **311**, 431 (2004).

[158] A. Datta, L. Zhang, J. Nunn, N. K. Langford, A. Feito, M. B. Plenio, and I. A. Walmsley, "Compact continuous-variable entanglement distillation", Phys. Rev. Lett. **108**, 060502 (2012).

[159] N. S. Ananikian, L. N. Ananikyan, L. A. Chakhmakhchyan, A. N. Kocharian, "Magnetic properties and thermal entanglement on a triangulated Kagomé lattice", J. Phys. A: Math. Theor. **44**, 025001 (2011).

[160] N. Ananikian, L. Ananikyan, L. Chakhmakhchyan and A. Kocharyan, "Thermal entanglement and critical behavior of magnetic properties on triangulated Kagome lattice", Acta Polytechnica **51**, 7 (2011).

[161] N. S. Ananikian, L. N. Ananikyan, L. A. Chakhmakhchyan, O. Rojas, "Thermal entanglement of a spin-1/2 Ising-Heisenberg model on a symmetrical diamond chain", J. Phys.: Condens. Matter, **24**, 256001 (2012).

[162] L. Chakhmakhchyan, N. Ananikian, L. Ananikyan and Č. Burdík, "Thermal entanglement of the spin-1/2 diamond chain", J. Phys: Conf. Series **343**, 012022 (2012).

[163] L. N. Ananikyan, N. S. Ananikian, and L. A. Chakhmakhchyan, "Arnold tongues and Feigenbaum exponents of the rational mapping for Q-state Potts model on recursive Lattice: $Q < 2$", Fractals **18**, 371 (2010).

[164] N. S. Ananikian, L. N. Ananikyan, and L. A. Chakhmakhchyan, "Cyclic period-3 window in antiferromagnetic Potts and Ising models on recursive lattices", JETP Lett. **94**, 39 (2011).

[165] L. Chakhmakhchyan, D. Shepelyansky, "Pagerank Model of Opinion Formation on Ulam Networks", Phys. Lett. A **377**, 3119 (2013).

[166] N. Ananikian, R. Artuso, L. Chakhmakhchyan, "Superstable Cycles for Antiferromagnetic Q-State Potts and Three-Site Interaction Ising Models on Recursive Lattices", Commun. Nonlinear Sci. Numer. Simulat. **19**, 3671 (2014).

[167] L. A. Chakhmakhchyan, "Entanglement of effectively coupld three atoms", Journal of Contemporary Physics (NAS of Armenia) **48**, 193 (2013).

[168] G. Grigoryan, C. Leroy, L. Chakhmakhchyan, Y. Pashayan-Leroy, S. Guérin, and H.R. Jauslin, "Stimulated Raman Adiabatic Passage via bright state in Λ medium of unequal oscillator strengths", Eur. Phys. J. D **66**, 256 (2012).

[169] L. Chakhmakhchyan, G. Grigoryan, C. Leroy, Y. Pashayan-Leroy, S. Guérin, and H.R. Jauslin, ”Influence of unequal oscillator strengths on Stimulated Raman Adiabatic Passage via bright state”, Int. J. Mod. Phys.: Conf. Series **15**, 147 (2012).

[170] L. Chakhmakhchyan, S. Guérin, J. Nunn, A. Datta, ”A compact entanglement distillery using realistic quantum memories”, Phys. Rev. A **88**, 042312 (2013).

[171] M. Drillon, E. Coronado, M. Belaiche, and R. L. Carlin, ”Low-dimensional magnetic systems; from 1D to 3D ferrimagnets”, J. Appl. Phys. **63**, 3551 (1988).

[172] M. Drillon, M. Belaiche, P. Legoll, J. Aride, A. Boukhari, A. Moqine, ”1D ferrimagnetism in copper(II) trimetric chains: specific heat and magnetic behavior of $A_3Cu_3(PO_4)_4$ with A = Ca, Sr”, J. Magn. Magn. Mater. **128**, 83 (1993).

[173] H. Sakurai, K. Yoshimura, K. Kosuge, N. Tsujii, H. Abe, H. Kitazawa, G. Kido, H. Michor, and G. Hilscher, ”Antiferromagnetic order in $Bi_4Cu_3V_2O_{14}$ with novel spin chain”, J. Phys. Soc. Jpn. **71**, 1161 (2002).

[174] D. Uematsu, M. Sato, ”Magnetic properties of $Cu_3(TeO_3)_2Br_2$ with spin 1/2 diamond lattice”, J. Phys. Soc. Jpn. **76**, 084712 (2007).

[175] H. Kikuchi *et al.*, ”Magnetic properties of the diamond chain compound $Cu_3(CO_3)_2(OH)_2$”, Progr. Theor. Phys. Suppl. **159**, 1 (2005).

[176] S. Valverde, O. Rojas and S. M. de Souza, ”Phase diagram of the asymmetric tetrahedral IsingHeisenberg chain”, J. Phys.: Condens. Matter **20**, 345208 (2008).

[177] Y.-Ch. Li, S.-S. Li, ”Quantum phase transitions in the $S = 1/2$ distorted diamond chain”, Phys. Rev. B **78**, 184412 (2008).

[178] K. C. Rule, A. U. B. Wolter, S. Süllow, D. A. Tennant, A. Brühl, S. Kühler, B. Wolf, M. Lang, and J. Schreuer, ”Nature of the spin dynamics and 1/3 magnetization plateau in azurite”, Phys. Rev. Lett. **100**, 117202 (2008).

[179] F. Aimo, S. Krämer, M. Klanjšek, M. Horvatić, and C. Berthier, ”Magnetic structure of azurite above the magnetization plateau at 1/3 of saturation”, Phys. Rev. B **84**, 012401 (2011).

[180] K. Takano, K. Kubo, and H. Sakamoto, "Ground states with cluster structures in a frustrated Heisenberg chain", J. Phys.: Condens. Matter **8**, 6405 (1996).

[181] T. Tonegawa, K. Okamoto, T. Hikihara, Y. Takahashi, M. Kaburagi, "Ground state of an $S = 1/2$ distorted diamond chain in a finite magnetic field", J. Phys. Chem. Solids **62**, 125 (2001).

[182] T. Tonegawa, K. Okamoto, T. Hikihara, "Possible quasi-one-dimensional Fermi surface in $La_{2-x}Sr_xCuO_4$", J. Phys. Soc. Jpn. **69**, 332 (2000).

[183] A. Honecker and A. Lauchli, "Frustrated trimer chain model and $Cu_3Cl_6(H_2O)_2{\cdot}2H_8C_4SO_2$ in a magnetic field", Phys. Rev. B **63**, 174407 (2001).

[184] N. B. Ivanov, J. Richter, J. Schulenburg, "Diamond chains with multiple-spin exchange interactions", Phys. Rev. B **79**, 104412 (2009).

[185] A. Honecker, S. Hu, R. Peters, J. Richter, "Dynamic and thermodynamic properties of the generalised diamond chain model for azurite", J. Phys.: Condens. Matter **23**, 164211 (2011).

[186] K. C. Rule, M. Reehuis, M. C. R. Gibson, B. Ouladdiaf, M. J. Gutmann, J.-U. Hoffmann, S. Gerischer, D. A. Tennant, S. Süllow, and M. Lang6 "Magnetic and crystal structure of azurite $Cu_3(CO_3)_2(OH)_2$ as determined by neutron diffraction" Phys. Rev. B **83**, 104401 (2011).

[187] J. Kang, C. Lee, R. K. Kremer, M.-H. Whangbo, "Consequences of the intrachain dimermonomer spin frustration and the interchain dimermonomer spin exchange in the diamond-chain compound azurite $Cu_3(CO_3)_2(OH)_2$", J. Phys.: Condens. Matter **21**, 392201 (2009).

[188] H. Jeschke *et al.*, "Multistep approach to microscopic models for frustrated quantum magnets: the case of the natural mineral azurite", Phys. Rev. Lett. **106**, 217201 (2011).

[189] J. Strecka, M. Jascur, M. Hagiwara, K. Minami, Y. Narumi, and K. Kindo, "Thermodynamic properties of a tetramer Ising-Heisenberg bond-alternating chain as a model system for Cu(3-Chloropyridine)$_2$(N$_3$)$_2$", Phys. Rev. B **72**, 024459 (2005).

[190] N. Ryo, W. Yuichi, N. Yuhei, "A theoretical study of magnons for Heisenberg model in triangulated Kagomé lattice - characteristic dispersionless modes", J. Phys. Soc. Jpn. **66**, 3687 (1997).

[191] J. Zheng and G. Sun, "Exact results for Ising models on the triangular Kagomé lattice", Phys. Rev. B **71**, 052408 (2005).

[192] J. Strečka, L. Čanova, M. Jaščur, and M. Hagiwara, "Exact solution of the geometrically frustrated spin-1/2 Ising-Heisenberg model on the triangulated Kagome (triangles-in-triangles) lattice", Phys. Rev. B **78**, 024427 (2008).

[193] D.-X. Yao, Y. L. Loh and E. W. Carlson, "XXZ and Ising spins on the triangular Kagome lattice" Phys. Rev. B **78**, 024428 (2008).

[194] M. Mekata, M. Abdulla, T. Asano, H. Kikuchi, T. Goto, T. Morishita, H. Hori, "Magnetic ordering in triangulated Kagomé lattice compound, $Cu_9Cl_2(cpa)_6\cdot nH_2O$", J. Magn. Magn. Mater. **177**, 731 (1998).

[195] V. Subrahmanyam, "Quantum entanglement in Heisenberg antiferromagnets", Phys. Rev. A **69**, 022311 (2004).

[196] X. Wang, H. Fu, A. I. Solomon, "Thermal entanglement in three-qubit Heisenberg models", J. Phys. A.: Math. Gen. **34**, 11307 (2001).

[197] G. D. Mahan, *Many-Particle Physics* (Kluwer/Plenum, New York, 2000).

[198] X.-G. Wen, *Quantum Field Theory of Many-Body Systems* (OUP, Oxford, 2004).

[199] G. Wei, J. Liu, H. Miao, and A. Du, "Multicritical behavior of the Ising metamagnet in both external longitudinal and transverse fields", Phys. Rev. B **76**, 054402 (2007).

[200] S.-S. Gong, G. Su, "Thermal entanglement of one-dimensional Heisenberg quantum spin chains in magnetic fields", Phys. Rev. A **80**, 012323 (2009).

[201] M. Asoudeh and V. Karimipour, "Thermal entanglement of spins in mean-field clusters", Phys. Rev. A **73**, 062109 (2006).

[202] N. Canosa, J. M. Matera, R. Rossignoli, "Description of thermal entanglement with the static path plus random-phase approximation", Phys. Rev. A **76** 022310 (2007).

[203] V. Vedral, "Mean-field approximations and multipartite thermal correlations", New J. Phys. **6** 22 (2004).

[204] G. Benenti, G. Casati, G. Strini, *Principles of Quantum Computation and Information - Volume II: Basic Tools and Special Topics* (World Scientific, Singapore, 2004).

[205] A. R. P. Rau, "Algebraic characterization of X-states in quantum information", J. Phys. A: Math. Gen. **42**, 412002 (2009).

[206] A. R. P. Rau, M. Ali, G. Alber, " Hastening, delaying, or averting sudden death of quantum entanglement", Eur. Phys. Lett. **82**, 40002 (2008).

[207] K. M. O'Connor and W. K. Wootters, "Entangled rings", Phys. Rev. A **63**, 052302 (2001).

[208] X. Wang and P. Zanardi, "Quantum entanglement and Bell inequalities in Heisenberg spin chains", Phys. Lett. A **301**, 1 (2002).

[209] T. Yu and J. H. Eberly, "Quantum Open System Theory: Bipartite Aspects", Phys. Rev. Lett. **97**, 140403 (2006).

[210] S. Morrison and A. S. Parkins, "Dynamical Quantum Phase Transitions in the Dissipative Lipkin-Meshkov-Glick Model with Proposed Realization in Optical Cavity QED", Phys. Rev. Lett. **100**, 040403 (2008).

[211] A. N. Kocharian, C. Yang, Y. L. Chiang, and T. Y. Chou, "Exact and self-consistent results in one-dimensional repulsive Hubbard model", Int. J. Mod. Phys. B **17**, 5749 (2003).

[212] M. S. S. Pereira, F. A. B. F. de Moura, and M. L. Lyra, "Magnetization plateau in diamond chains with delocalized interstitial spins", Phys. Rev. B **77**, 024402 (2008).

[213] G. Chaboussant, A. Sieber, S. Ochsenbein, H.-U. Güdel, M. Murrie, A. Honecker, N. Fukushima, B. Normand, "Exchange interactions and high-energy spin states in Mn_{12}-acetate", Phys. Rev. B **70**, 104422 (2004).

[214] H. Z. Kou, B. C. Zhou, S. Gao, D.-Z. Liao, R.-J. Wang, "Pendant macrocyclic metallic building blocks for the design of cyano-bridged heterometallic complexes with 1D chain and 2D layer structures", Inorg. Chem. **42**, 5604 (2003).

[215] M. Hagiwara, H. Tsujii, C. R. Rotundu, B. Andraka, Y. Takano, N. Tateiwa, T. C. Kobayashi, T. Suzuki, and S. Suga, "Tomonaga-Luttinger liquid in a quasi-one-dimensional $S = 1$ antiferromagnet observed by specific heat measurements", Phys. Rev. Lett. **96**, 147203 (2006).

[216] M. E. Zhitomirsky, and A. Honecker, "Magnetocaloric effect in one-dimensional antiferromagnets", J. Stat. Mech.: Theor. Exp. P07012 (2004).

[217] C. Trippe, A. Honecker, A. Klumper, and V. Ohanyan, "Exact calculation of the magnetocaloric effect in the spin-1/2 XXZ chain", Phys. Rev. B **81**, 054402 (2010).

[218] J. Abouie, A. Langari, and M. Siahatgar, "Thermodynamic behavior of the XXZ Heisenberg $s = 1/2$ chain around the factorizing magnetic field", J. Phys.: Condens. Matter **22**, 216008 (2010).

[219] S. Maegawa, R. Kaji, S. Kanou, A. Oyamada, and M. Nishiyama, "Spin dynamics in classical and quantum Kagome lattice magnets studied by NMR", J. Phys.: Condens. Matter **19**, 145250 (2007).

[220] R. J. Baxter, *Exactly Solved Models in Statistical Mechanics* (Academic Press, New York, 1982).

[221] A. Z. Akheyan and N. S. Ananikian, "Global Bethe lattice consideration of the spin-1 Ising model", J. Phys. A: Math. Gen. **29**, 721 (1996).

[222] A. Z. Akheyan, N. S. Ananikian, S. K. Dallakian, "The phase structure of the antiferromagnetic Ising model in the presence of frustrations", Phys. Lett. A **242**, 111 (1998).

[223] N. S. Ananikian, A. R. Avakian, N. Sh. Izmailian, "Phase diagrams and tricritical effects in the BEG model", Physica A **172**, 391 (1991).

[224] N.S. Ananikian, R. R. Lusiniants, K. A. Oganessyan, "The multisite antiferromagnetic Ising spin model and the univeisality of Feingenbaum exponents", JETP Lett. **61**, 482 (1995).

[225] P. Manneville, Y. Pomeau, "Intermittency and the Lorenz model", Phys. Lett. A **75**, 1 (1979).

[226] P. Manneville, Y. Pomeau, "Different ways to turbulence in dissipative dynamical systems", Physica D **1**, 219 (1980).

[227] D. V. Vagin, O. P. Polyakov, "Effect of sample shape on nonlinear magnetization dynamics under an external magnetic field", J. Magn. Magn. Mater. **320**, 3394 (2008).

[228] S. Ishii, M. -A. Sato, "Chaotic Potts spin model for combinatorial optimization problems", Neural Networks **10**, 941 (1997).

[229] D. M. Maranhao, M. S. Baptista, J. C. Sartorelli, and I. L. Caldas, "Experimental observation of a complex periodic window", Phys. Rev. E **77**, 037202 (2008).

[230] N. Ananikian, L. Ananikyan, R. Artuso, H. Lazaryan, "Magnetization and Lyapunov exponents on a Kagome chain with multi-site exchange interaction", Phys. Lett. A **374**, 4084 (2010).

[231] C. Anteneodo, R. N. P. Maia, and R. O. Vallejos, "Lyapunov exponent of many-particle systems: testing the stochastic approach", Phys. Rev. E **68**, 036120 (2003).

[232] N. S. Ananikian, L .N. Ananikyan, R. Artuso, and V. V. Hovhannisyan, "Modulated phases and Lyapunov exponent for the antiferromagnetic Q-state Potts and multi-site exchange interaction Ising models", Physica D **239**, 1723 (2009).

[233] L. P. Kadanoff, "Scaling and universality in statistical physics", Physica A **163**, 1 (1990).

[234] M. J. Feigenbaum, ”The transition to aperiodic behavior in turbulent systems”, Commun. Math. Phys. **77**, 65 (1980) 65.

[235] M. J. Feigenbaum, ”Quantitative universality for a class of nonlinear transformations”, J. Stat. Phys. **19**, 25 (1978).

[236] A. Z. Akheyan, N. S. Ananikian, ”Antiferromagnetic Potts model: phase transition through doubling bifurcation”, Phys. Lett. A **186**, 171 (1994).

[237] J. L. Monroe, ”Phase diagrams of Ising models on Husimi trees. I. Pure multisite interaction systems”, J. Stat. Phys. **65**, 255 (1991).

[238] N. S. Ananikian and S. K. Dallakian, ”Multifractal approach to three-site antiferromagnetic Ising model”, Physica D **107**, 75 (1997).

[239] N. S. Ananikian, S. K. Dallakian and B. Hu, ”The chaotic properties of the Q-state Potts model on the Bethe lattice: $Q < 2$”, Complex Systems **11**, 213 (1997).

[240] H. G. Schuster, *Deterministic Chaos* (Physic-Verlag, Weinheim, 1984).

[241] J. Marsden, M. McCracken (eds.), *The Hopf-Bifurcation and its Applications* (Springer-Verlag, New York, 1976).

[242] S. Zambrano, I. P. Mariño, and M. A. F Sanjuán, ”Controlling crisis-induced intermittency using its relation with a boundary crisis”, New J. Phys. **11**, 023025 (2009).

[243] A. P. Kuznetsov, N. V. Stankevich, and L. V. Tyuryukina, ”Stabilizing the Rössler system by external pulses on a runaway trajectory”, Tech. Phys. Lett. **34**, 618 (2008).

[244] C. Grebogi, E. Ott, J. A. Yorke, ”Crises, sudden changes in chaotic attractors, and transient chaos”, Physica D **7**, 181 (1983).

[245] J. Guckenheimer, G. Oster, and A. Ipaktchi, ”The dynamics of density dependent population models”, J. Math. Biol. **4**, 101 (1977).

[246] M. H. Lee, ”Analytical study of the superstable 3-cycle in the logistic map”, J. Math. Phys. **50**, 122702 (2009).

[247] L. Ermann and D. L. Shepelyansky, "Google matrix and Ulam networks of intermittency maps", Phys. Rev. E **81**, 036221 (2010).

[248] S. Morrison, A. S. Parkins, "Dissipation-driven quantum phase transitions in collective spin systems", J. Phys. B: At. Mol. Opt. Phys. **41**, 195502 (2008).

[249] G. Chen, J.-Q. Liang and S. Jia, "Interaction-induced Lipkin-Meshkov-Glick model in a Bose-Einstein condensate inside an optical cavity", Optics Express **17**, 19682 (2009).

[250] Y. L. Zhou, M. Ortner, and P. Rabl, "Long-range and frustrated spin-spin interactions in crystals of cold polar molecules", Phys. Rev. A **84**, 052332 (2011).

[251] R. Orús, S. Dusuel, J. Vidal, "Equivalence of critical scaling laws for many-body entanglement in the Lipkin-Meshkov-Glick model", Phys. Rev. Lett. **101**, 025701 (2008).

[252] K. Bergmann, H. Theuer, B. W. Shore, "Coherent population transfer among quantum states of atoms and molecules", Rev. Mod. Phys. **70**, 1003 (1998).

[253] G. Alzetta, A. Gozzini, L. Moi, and G. Orriols, "An experimental method for the observation of R.F. transitions and laser beat resonances in oriented Na vapour", Nuovo Cim. B **36**, 5 (1976).

[254] N. V. Vitanov and S. Stenholm, "Properties of stimulated Raman adiabatic passage with intermediate-level detuning", Opt. Commun. **135**, 394 (1997).

[255] N. V. Vitanov and S. Stenholm, "Analytic properties and effective two-level problems in stimulated Raman adiabatic passage", Phys. Rev. A **55**, 648 (1997).

[256] A. Messiah, *Quantum Mechanics* (North-Holland/Elsevier Science, New York, 1962).

[257] S. L. Braunstein and H. J. Kimble, "Teleportation of continuous quantum variables", Phys. Rev. Lett. **80**, 869 (1998).

[258] A. Furusawa, J. L. Sorensen, S. L. Braunstein, C. A. Fuchs, H. J. Kimble, E. S. Polzik, "Unconditional quantum teleportation", Science **282**, 706 (1998).

[259] X. Li, Q. Pan, J. Jing, J. Zhang, C. Xie, and K. Peng, "Quantum dense coding exploiting a bright Einstein-Podolsky-Rosen beam", Phys. Rev. Lett. **88**, 047904 (2002).

[260] J. Eisert, S. Scheel, and M. B. Plenio, "Distilling Gaussian states with Gaussian operations is impossible", Phys. Rev. Lett. **89**, 137903 (2002).

[261] J. Fiurášek, "Gaussian transformations and distillation of entangled Gaussian states", Phys. Rev. Lett. **89**, 137904 (2002).

[262] G. Giedke and J. I. Cirac, "Characterization of Gaussian operations and distillation of Gaussian states", Phys. Rev. A **66**, 032316 (2002).

[263] B. Hage, A. Samblowski, J. Diguglielmo, A. Franzen, J. Fiurášek, and R. Schnabel, "Preparation of distilled and purified continuous-variable entangled states", Nature Phys. **4**, 915 (2008).

[264] H. Takahashi, J. S. Neergaard-Nielsen, M. Takeuchi, M. Takeoka, K. Hayasaka, A. Furusawa, and M. Sasaki, "Entanglement distillation from Gaussian input states", Nature Photon. **4**, 178 (2010).

[265] N. Jain, S. R. Huisman, Erwan Bimbard, and A. I. Lvovsky, "A bridge between the single-photon and squeezed-vacuum states", Optics Express **18**, 18254 (2010).

[266] Y. Kurochkin, A. S. Prasad, A. I. Lvovsky, "Distillation of the two-mode squeezed state", arXiv:1307.3397 [quant-ph] (2013).

[267] M. Vidrighin, T. J. Bartley, G. Donati, X.-M. Jin, M. Barbieri, W. S. Kolthammer, A. Datta, I. A. Walmsley, "Requirements for two-source entanglement concentration", Quantum Measurements and Quantum Metrology **1**, 5 (2013).

[268] T. J. Bartley, P. J. D. Crowley, A. Datta, J. Nunn, L. Zhang, and I. Walmsley, "Strategies for enhancing quantum entanglement by local photon subtraction", Phys. Rev. A **87**, 022313 (2013).

[269] C. Simon *et al.*, "Quantum memories: a review based on the European integrated project "Qubit Applications (QAP)" " Eur. Phys. J. D **58**, 1 (2010).

[270] E. T. Campbell, M. G. Genoni, and J. Eisert, "Continuous-variable entanglement distillation and noncommutative central limit theorems", Phys. Rev. A **87**, 042330 (2013).

[271] S. Scheel, D.-G. Welsch, "Entanglement generation and degradation by passive optical devices", Phys. Rev. A **64**, 063811 (2001).

[272] J. Nunn, I. A. Walmsley, M. G. Raymer, K. Surmacz, F. C. Waldermann, Z. Wang, D. Jaksch, "Mapping broadband single-photon wavepackets into an atomic memory", Phys. Rev. A **75**, 011401(R) (2007).

[273] W. Pernice, C. Schuck, O. Minaeva, M. Li, G. N. Goltsman, A. V. Sergienko, H. X. Tang, "High speed and high efficiency travelling wave single-photon detectors embedded in nanophotonic circuits", Nature Comm. **3**, 1325 (2012).

[274] F. Marsili, V. B. Verma, J. A. Stern, S. Harrington, A. E. Lita, T. Gerrits, I. Vayshenker, B. Baek, M. D. Shaw, R. P. Mirin, and S. W. Nam, "Detecting single infrared photons with 93% system efficiency", Nature Photon. **7**, 210 (2013).

[275] M. Hosseini, B. M. Sparkes, G. Campbell, P. K. Lam, and B. C. Buchler, "High efficiency coherent optical memory with warm rubidium vapour", Nature Comm. **2**, 174 (2011).

[276] M. Sabooni, S. T. Kometa, A. Thuresson, S. Kröll, and L. Rippe, "Cavity-enhanced storagepreparing for high-efficiency quantum memories", New J. Phys. **15**, 035025 (2013).

[277] Y.-H. Chen, M.-J. Lee, I.-C. Wang, S. Du, Y.-F. Chen, Y.-C. Chen, and I. A. Yu, "Coherent optical memory with high dtorage efficiency and large fractional delay", Phys. Rev. Lett. **110**, 083601 (2013).

[278] Y. O. Dudin, L. Li, A. Kuzmich, "Light storage on the time scale of a minute", Phys. Rev. A. **87**, 031801 (2013).

[279] G. Heinze, C. Hubrich, T. Halfmann, "Stopped light and image storage by electromagnetically induced transparency up to the regime of one minute", Phys. Rev. Lett. **111**, 033601 (2013).

[280] G. Campbell, M. Hosseini, B. M. Sparkes, P. K. Lam and B. C. Buchler, "Time- and frequency-domain polariton interference ", New J. Phys. **14**, 033022 (2012).

[281] K. F. Reim, J. Nunn, X.-M. Jin, P. S. Michelberger, T. F. M. Champion, D. G. England, K. C. Lee, W. S. Kolthammer, N. K. Langford, and I. A. Walmsley, "Multipulse addressing of a Raman quantum memory: configurable beam splitting and efficient readout", Phys. Rev. Lett. **108**, 263602 (2012).

[282] K. F. Reim, J. Nunn, V. O. Lorenz, B. J. Sussman, K. C. Lee, N. K. Langford, D. Jaksch, and I. A. Walmsley, "Towards high-speed optical quantum memories", Nature Photon. **4**, 218 (2010).

[283] X.-H. Bao, A. Reingruber, P. Dietrich, J. Rui, A. Dück, T. Strassel, L. Li, N.-L. Liu, B. Zhao, and J.-W. Pan, "Efficient and long-lived quantum memory with cold atoms inside a ring cavity", Nature Phys. **8**, 517 (2012).

Conference theses and abstracts

[284] L. Chakhmakhchyan, D. Shepelyansky, "PageRank Model of Opinion Formation on Ulam Networks", 39*th* Conference of the Middle European Cooperation in Statistical Physics - MECO39 (Coventry, UK, 2014), book of abstracts, p. 56.

[285] L. Chakhmakhchyan, S. Guérin, C. Leroy, "Solvable Model for Ultrastrong QED Regime", IOTA Workshop on Cold Molecular Ions (Arosa, Switzerland, 2013), book of abstracts, p. 19.

[286] L. Chakhmakhchyan, "Entanglement Properties of a Spin-1/2 Diamond Chain", Control of Quantum Dynamics of Atoms, Molecules and Ensembles by Light Workshop - CAMEL9 (Nessebar, Bulgaria, 2013), book of abstracts, p. 2.

[287] L. Chakhmakhchyan, "Entanglement Properties of a Spin-1/2 Ising-Heisenberg Diamond Chain", Les 14èmes Journées de l'Ecole Doctorale Carnot Pasteur (Dijon, France, 2013), book of abstracts, p. 21.

[288] L. Chakhmakhchyan, N. Ananikian, S. Guérin, C. Leroy, "Superstable Cycles of Antiferromagnetic Potts and Ising Models on Recursive Lattices", 38*th* Conference of the

Middle European Cooperation in Statistical Physics - MECO38 (ICTP, Trieste, Italy 2013), list of poster presentations, p. 1.

[289] L. Chakhmakhchyan, A. Datta, G. Grigoryan, J. Nunn, "A Realistic Quantum Entanglement Distillery", Laser Physics 2013 (Ashtarak, Armenia), book of abstracts, p.2.

[290] L. Chakhmakhchyan, S. Guérin, C. Leroy, N. Ananikian, "Entanglement and Thermodynamic Properties of Three Coupled Atoms", Laser Physics 2012 (Ashtarak, Armenia), book of abstracts, p. 12.

[291] L. Chakhmakhchyan, G. Grigoryan, C. Leroy, Y. Pashayan-Leroy, S. Guérin, and H. R. Jauslin, "Influence of Unequal Oscillator Strengths on Stimulated Raman Adiabatic Passage through Bright State", Laser Physics 2011 (Ashtarak, Armenia), book of abstracts, p. 63.

[292] L. Chakhmakhchyan, "Thermal Entanglement of the Spin-1/2 Diamond Chain", The $7th$ International Conference Quantum Theory and Symmetries (Prague, Czech Republic, 2011), book of abstracts, p. 9.

[293] N. S. Ananikyan, L. N. Ananikian, L. A. Chakhmakhchyan and A. N. Kocharyan, "Thermal Entanglement and Critical Behavior of Magnetic Properties on a Triangulated Kagome Lattice", The $19th$ International Colloquium on Integrable Systems and Quantum symmetries, (Prague, Czech Republic, 2010), book of abstracts, p. 3.

[294] L. A. Chakhmakhchyan, N. S. Ananikian, L. N. Ananikyan and A. N. Kocharyan, "Common Features of Magnetic Properties and Thermal Entanglement on a Triangulated Kagome Lattice", Workshop on Principles and Design of Strongly Correlated Electronic Systems (ICTP, Miramare-Trieste, Italy, 2010), book of abstracts, p. 71.

[295] L. A. Chakhmakhchyan, N. S. Ananikian, L. N. Ananikyan, "Chaotic Behavior of the Q-state Potts Model on Recursive Lattice: $Q < 2$", Pseudochaos and Stable-Chaos in Statistical Mechanics and Quantum Physics (ICTP, Miramare-Trieste, Italy, 2009), book of abstracts, p. 29.

Title: Entangled states and coherent interaction in resonant media.

Abstract: The entanglement features of some solid state materials, as well as of particular systems of interacting atoms and fields are analyzed. A detailed investigation of the rich phase structure of low dimensional spin models, describing the natural mineral azurite ($Cu_3(CO_3)_2(OH)_2$) and copper based coordination compounds [Cu_9X_2 $(cpa)_6\cdot$ nH_2O ($X = F$, Cl, Br)], has revealed regimes with the most robust entanglement behavior. Using the dynamical system approach, the phase structure of some classical models on hierarchical (recursive) lattices has been also studied and, for the first time, the transition between chaotic and periodic regimes by means of tangent bifurcation has been detected.

A detailed description of entanglement properties of three atoms trapped in a cavity within the dispersive limit is presented. A relatively simple tunability of the atomic interaction strength of the above system and its close relation to the problems of frustrated magnetism is shown. Furthermore, the propagation effects of two intense laser pulses in a medium of Λ atoms with unequal oscillator strengths are investigated. Obtained results are crucial in some problems of quantum information theory, as, e.g., in the analysis of population transfer mechanism in media possessing the above properties. Finally, the dissipation effects in a recently proposed compact continuous-variable entanglement distillation protocol have been analyzed. Despite additional constraints on the parameters of the protocol, the discussed entanglement distillation scheme in quantum memories is still possible to implement within emerging technologies.

Key words: Quantum entanglement; spin-lattice models; bifurcation; chaos; dispersive regime; adiabatic population transfer; entanglement distillation.

Titre : Etats intriqués et interaction cohérente dans les milieux résonants.

Résumé : Nous analysons les caractéristiques d'intrication de quelques matériaux à l'état solide ainsi que des systèmes particuliers d'atomes et de champs interagissants. Une étude détaillée de la riche structure de phase des modèles de spins de basse dimension, décrivant le minéral naturel d'azurite ($Cu_3(CO_3)_2(OH)_2$) et les composés de coordination à base de cuivre [Cu_9X_2 $(cpa)_6\cdot$ nH_2O ($X = F$, Cl, Br)], a révélé des régimes à comportement d'intrication des plus robustes. En utilisant l'approche des systèmes dynamiques, la structure de phase de certains modèles classiques en réseaux hiérarchiques (récursifs) a aussi été étudiée et, pour la première fois, la transition entre régime chaotique et régime périodique au moyen de la bifurcation tangente a été détectée.

Nous présentons une description détaillée des propriétés d'intrication de trois atomes piégés dans la limite dispersive. Une relativement simple accordabilité de la force atomique d'interaction de ce système et son étroite relation aux problèmes de frustration magnétique est démontrée. En outre, les effets de propagation de pulses laser intenses dans un système atomique de type Λ avec des forces d'oscillateurs différentes sont analysés. Les résultats obtenus sont d'extrême importance dans des problèmes d'information quantique, comme par exemple, dans l'analyse du mécanisme de transfert de population dans des milieux ayant les propriétés définies ci-avant. Enfin, nous avons analysé les effets dissipatifs dans un protocole de distillation de l'intrication à variable continue récemment proposé. En dépit de contraintes additionnelles sur les paramètres du protocole, il est encore possible d'implémenter ce schéma de distillation de l'intrication évoqué ci-avant dans les technologies émergentes.

Mots clefs : Intrication quantique ; modèles de réseaux de spins ; bifurcation ; chaos ; régime dispersif ; transfert adiabatique de population ; distillation de l'intrication.